Development of Novel Biosensing Platforms using Metal, Metal-Insulator-Metal (MIM) and Quantum Materials

by

Dipanjan Nandi

A thesis submitted in partial fulfillment of the requirements for the degree of

Doctor of Philosophy

in

Photonics and Plasmas

Department of Electrical and Computer Engineering
University of Alberta

Abstract

Rapid and accurate testing of easily transmissible diseases is essential to prevent extensive breakouts, identify infected individuals for timely treatment, and curb transmission by taking suitable measures. With the advancement of nanotechnology, biosensors are becoming an indispensable tool in drug development, biomedicine, disease monitoring, and food safety. Nanophotonic biosensors rely on the interaction of the evanescent field with target bioanalytes to produce a measurable optical signal output. This thesis is a groundbreaking achievement in the field of nanoresonator-based biosensor platforms. Through the use of finite-difference time-domain (FDTD) simulations, we have developed three distinct designs that incorporate metal-insulator-metal (MIM), gold (Au), and 2D material nanoresonators. These designs have the potential to revolutionize the biosensor industry and pave the way for new and innovative applications.

The design of two different MIM nanoresonator configurations, (i) metal-insulator-metal nanopillar array and (ii) metal nanoresonator array on insulator-metal thin film stack, were nurtured. The influence of the geometric parameters such as diameter, pitch, insulator layer's materials and thickness, the shape of individual nanoresonators, and the array arrangements were cultivated efficiently to balance the leakiness of MIM nanoresonators for achieving high surface sensitivity. With the best design parameters, MIM nanoresonators were fabricated and experimentally validated with varying concentrations of polystyrene beads. The MIM nanopillar array device demonstrated the best experimental detection sensitivity of 6.54 $\pm$ 0.7 nm/decade for polystyrene beads of 100 nm diameter. Polystyrene beads were used to test the

device's performance as their optical properties, such as refractive index and extinction coefficient, match well with most bioanalytes.

Despite the high degree of tunability of localized surface plasmon resonance field, the fabrication complexity associated with different MIM nanoresonators imposes limitations for mass production and cost-effectiveness. In this context, plasmonic Au nanoresonators were proposed, and the best design was established using FDTD simulation to enhance the localized surface plasmon resonance (LSPR) field. The devices were fabricated with the best design parameters and were biofunctionalized, demonstrating SARS-CoV-2 detection with one of the lowest limits of detection 1 virus-like particle (VLP) μL^{-1} and detection sensitivity of 1.32 $\pm$ 0.08 nm/decade. We also proposed a design of a portable point-of-care biosensing platform using our Au nanoresonators.

Furthermore, we delved into different metasurface designs of MoS_2 nanoresonators to mitigate the field dissipation issues that plague the plasmonic metal nanostructures. We introduced three groundbreaking MoS_2 nanoresonator designs for biosensor platforms, established novel fabrication methods and experimentally evaluated their performances. MoS_2 was selected as the material for the nanoresonator due to its high refractive index and low absorption coefficient in the visible wavelength range. Moreover, MoS_2 has minimal cytotoxicity and biocompatibility, making it suitable for various biosensing applications. The best design obtained from FDTD simulations were utilized to fabricate nanoresonators with the large area (1 inch $\times$ 1 inch) MoS_2 thin film grown by pulsed laser deposition system. The experimental measurements provided a detection sensitivity of 13.71 $\pm$ 1.7 nm/decade and a limit of detection (LOD) of 4 polystyrene beads.

By innovating three distinct nanophotonic platforms, we have showcased the adept detection of 100 nm-sized polystyrene beads and SARS-CoV-2 virus-like particles. This thesis research not only underscores the accomplishment of nanophotonics but also symbolizes its profound capacity to make a monumental impact in biosens-

ing. Our ingenious approach has demonstrated capability and illuminated a path where nanophotonics emerges as a transformative force, fundamentally reshaping the biosensing landscape with unparalleled precision and efficacy.

Preface

The research work both the simulation and experimental works are carried out at the department of Electrical and computer Engineering, University of Alberta during the time frame of January 2017 and November 2023. Dr. Manisha Gupta conceptualized the research project. All the simulation, fabrication, characterization, experimental measurements, analysis of data, review and editing the manuscript by Dipanjan Nandi.

The work in Chapter 3 was published as Dipanjan Nandi, Md. Zahurul Islam, and Manisha Gupta, "Optimization of a leaky plasmonic metal-insulator-metal nanopillar array for low concentration biosensing applications", Journal of Optical Society of America B, vol: 39, issue: 10, pp. 2705-2713, 2022, doi: https://doi.org/10.1364/JOSAB.468244. All the simulations and analysis were conducted by Dipanjan Nandi. Manuscript was written by Dipanjan Nandi, and reviewed by Md. Zahurul Islam and Dr. Manisha Gupta.

The works presented in Chapter 4, simulations, fabrication of MIM nanopillar devices, characterization and experimental measurements with polystyrene beads conducted by Dipanjan Nandi. The manuscript was written by Dipanjan Nandi and reviewd by Dr. Manisha Gupta.

In Chapter 5, the simulation, nanofabrication of devices and experimental setup, experimental measurements are conducted by Dipanjan Nandi. Jiaxin Fan and Seongdae Kang established the protocol for functionalizing Au nanodots array. They also prepared the concentrations of SARS-CoV-2 virus like particles for experimental measurements. Reflection spectroscopic measurements with SARS-CoV-2 were conducted

and data analysis were performed by Dipanjan Nandi. The results and analysis are reviewed by Dr. Manisha Gupta.

All the FDTD simulations in Chapter 6 were performed by Dipanjan Nandi. Data analysis and manuscript was prepared by Dipanjan Nandi and reviewed by Dr. Manisha Gupta.

In Chapter 7, the simulations, fabrication of MoS_2 nanoresonators array devices and measurements are conducted by Dipanjan Nandi. The MoS_2 thin film samples were grown, optimization of the PLD growth parameters by Andres Alejandro Forero Pico and Dhanvini Gudi. Andres Alejandro Forero Pico also conducted the AFM measurements and analyzed the data. He also helped in optimizing the RIE etching recipe of MoS_2. The TEM images were taken by Dr. Payel Sen and analyzed by her. The data analysis was performed and manuscript was written by Dipanjan Nandi. The manuscript was reviewed by Dr. Manisha Gupta.

Acknowledgements

I wish to express my utmost appreciation to my mentor and supervisor, Dr. Manisha Gupta, for affording me the opportunity to embark on this research expedition. Her unbridled zeal for research has been an unwavering source of inspiration to me throughout my Ph.D. studies. I am indebted to her for her unfailing patience, support, and guidance, without which I would not have been able to complete this thesis. In particular, I am grateful for the freedom and learning opportunities she has accorded me, which have enabled me to grow and excel in my field of study.

I would like to extend my sincerest gratitude to my current and former colleagues in the laboratory, including Jiaxin Fan, Payel Sen, Seongdae Kang, Andres Alejandro Forero Pico, Junsen Gao, Dhanvini Gudi, Paul Lavryshyn, Michelle Livojevic, Jyoti Yadav, Darren Majak, and Michael Facchini-Rakovich. Their unwavering support and assistance have been invaluable to me throughout my Ph.D. journey. I am particularly grateful for the positive and welcoming work environment that they have created, which has made my experience more fulfilling and enjoyable. The memories of our coffee breaks, lunch hours, and ice cream outings will always hold a special place in my heart. Once again, thank you for your contributions to my academic and personal growth.

I would like to express my heartfelt gratitude to my parents who have always supported me unconditionally. They have never imposed any sort of pressure on me and have given me the freedom to pursue my interests. I feel extremely fortunate to have such loving and open-minded parents. Finally, I want to express my gratitude to my wife, Barnali De. She has always been my biggest support, even during difficult

times, and has lifted me up when I was feeling low. I owe you a debt of gratitude for being my constant pillar of strength. Thank you for always standing by me.

I would like to extend my deepest appreciation for the financial assistance I have received from the University of Alberta Doctoral Recruitment Scholarship, J. Gordin Kaplan Graduate Student Academic Travel Award, Natural Sciences and Engineering Research Council of Canada, Alberta Innovates, and the MNT financial assistance for conducting fabrication and characterization costs provided by CMC Microsystems. Their generous support has been invaluable in facilitating my research.

Table of Contents

List of Tables

List of Figures

Abbreviations

AFM Atomic force microscopy.

ALD Atomic layer deposition.

DMEM Dulbecco's Modified Eagle Medium.

EBL Electron beam lithography.

FDTD Finite difference time domain.

FOM Figures of merit.

FTIR Fourier transform infra-red.

FWHM Full-width at half maximum.

GSPR Gap-surface plasmon resonance.

ICP-RIE Inductively-coupled plasma reactive ion etching.

LOD Limit of detection.

LSPR Localized surface plasmon resonance.

MIM Metal-insulator-metal.

PhC Photonic crystal.

PLD Pulsed laser deposition.

PVD Physical vapour deposition.

RIU Refractive index unit.

SARS-CoV-2 Severe acute respiratory syndrome coronavirus 2.

SEM Scanning electron microscopy.

SPR Surface plasmon resonance.

TFSF Total-field scattered field.

VLPs Virus like particles.

XPS X-ray photoelectron spectroscopy.

XRD X-ray diffraction.

Chapter 1

Introduction

1.1 Motivation of thesis

Medical facilities often use various analytical methods to collect diagnostic information from patients. By gathering the information from various medical tests, doctors and healthcare professionals can make crucial decisions about critical care for the patients to achieve fast health recovery. The widely used diagnostic techniques include labeled immunoassays, cell culture, optical confocal microscopy, and polymerase chain reaction (PCR). Significant limitations of the existing medical diagnostic systems are the following:

- Time-consuming (takes a few hours to days) multi-step process.
- Higher maintenance cost for the instrument and other accessories for running the medical diagnostic tests.
- Complex operation procedures of the diagnostic instruments.
- Thoroughly preparing and purifying an ample sample volume is of utmost importance in ensuring precise test outcomes.
- Requirement of well-trained technical personnel.
- Not compatible for rapid, point-of-care testing and analysis.

Biosensors are analytical devices that have the ability to convert biological responses into a measurable output like electrical or, optical signals. The ability to provide

real-time, reliable, and non-invasive analysis makes them highly valuable in a number of critical fields such as healthcare [1–4], food safety [5], environmental monitoring [6], pharmaceutics and drug discovery [7–9], security and forensics [10, 11], etc. L. C. Clark Jr. *et. al.*, [12, 13] first developed an instrument to monitor the blood O_2, CO_2 and *p*H using electrodes for open heart surgery patients. The term "biosensor" was later coined by Cammann [14], and the definition was introduced by IUPAC [15]. The field of biosensors has seen remarkable advancements both in technology and applications, with innovative approaches ranging from electrochemistry to nanotechnology and bioelectronics. The essential components of any biosensor are the (i) bioreceptors or, bio-recognition elements, (ii) transducers, and (iii) signal processing system. Schematic Fig 1.1 depicts different components of a biosensing platform. Target analytes are attached to the bioreceptor part of the biosensor. An important characteristic of biosensors is their ability to exhibit a high degree of specificity, allowing them to accurately detect target analytes without providing false-positive readings. The bioreceptors play a significant role in identifying specific substances or target molecules by the interaction with the target analytes. The transducer then converts the analyte-bioreceptor interaction into a quantitative signal that can be measured and analyzed (by the signal processing system) to determine the presence and quantify the target analytes.

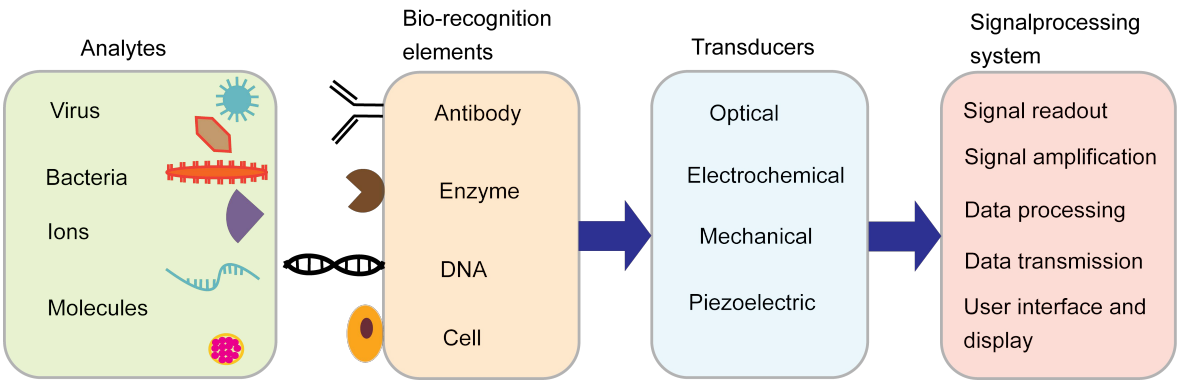

Figure 1.1: Schematic view demonstrates the key elements of a typical biosensor.

Among different types of transducers, optical/photonic biosensors are devices that utilize biomolecular receptors for specific analyte interaction in terms of optical signal transduction, coupled with an optical readout system that provides information on this interaction. The optical spectroscopic techniques (such as, Raman spectroscopy [16, 17], photoluminescence [18], near-infrared (NIR) fluorescence [19], Fourier-transform infrared (FTIR) spectroscopy [20, 21], UV-Vis spectroscopy [22]) dynamic light scattering (DLS) [23] and nanoparticle tracking analysis (NTA) [24] have been utilized broadly for various biomolecules sensing, drug discovery and monitoring the kinetics of biochemical reactions in bio-pharmaceutical industry applications. However, the above mentioned optical biosensing methods require lab infrastructure, trained personnel for handling, making them cumbersome and unsuitable for on-site practice and lab-on-chip applications.

In recent times, the field of nanotechnology has witnessed significant advancements, leading to the emergence of nanomaterials with unique optoelectronic properties. Nanophotonic sensors utilize the light-matter interaction to produce measurable optical signal output, allowing rapid, accurate measurements. Evanescent-field-based photonic biosensors are highly effective for analyzing biomolecules using light. The surface sensitivity of these photonic sensors is due to the exponentially decaying evanescent field perpendicular to the sensor surface, with a decay length of hundreds of nanometres. This unique feature enhances the light-matter interaction of the evanescent field with the target analytes immobilized on the sensor surface, provides precise spatial control over measurements. The four main categories of nanophotonic biosensors are: (i) plasmonic biosensors, (ii) optical waveguide (including optical fibers) and interferometer-based biosensors, (iii) optical resonator-based biosensing platforms, and (iv) metasurface biosensors. Nanophotonic structures exhibit a tight confinement of light in the close proximity to their surface, even a distance down to 10 nm known as “hot-spots”. The localized field intensity is amplified by the orders of 3-4 times of magnitude of incident light intensity. This particular feature of nanopho-

tonic biosensors makes them more sensitive near to the surface and thus makes the sensor less susceptible to the background interference. However, the performance of nanophotonic biosensors depends on the alignment of the target bioanalytes captured on the regions that exhibit the highest evanescent field intensity. The nanophotonic sensors' performance can be engineered by changing the nanoresonators geometry, constituent materials, etc. In situations where the active sensing area (strongly localized evanescent field) is very small, the transportation of analytes to the specific target locations needs a complex arrangement and detection of single analytes with a small diameter ($\leq$ 100 nm) can be challenging. The misalignment of analytes with the confined resonant optical field may have an impact on the sensor's performance (such as sensitivity, figure of merit (FOM), and limit of detection (LOD)).

In this work, we have focused on two types of nanophotonic biosensor configurations: (i) plasmonic nanoresonators and (ii) dielectric/semiconductor metasurface based biosensing platforms with the goal of detection of small size analytes of ultra-low concentration. The plasmonic nanoresonators was chosen due to their capacity to amplify resonance optical field. Our research focused on understanding the influences of both plasmonic metal and metal-insulator-metal (MIM) nanoresonator's geometry on the resonance properties. Additionally, the correlation between the nanophotonic device design parameters with the target particle size was also studied. Nanophotonic resonators' design was optimized to gain precise control over the leaky behaviour of individual plasmonic nanoresonator and improve coupling of neighbouring nanoresonators to achieve high sensing performance. We aim to develop nanophotonic sensing platform that features a large active sensing region for detecting bioanalytes (of $\leq$ 100 nm) without requiring a specific bioanalytes delivery mechanism. On the other hand, high-index dielectric/semiconductor nanostructures are a useful alternative to plasmonic systems. These nanoresonators offer high Q-factor resonances and significant amplification of electric and magnetic near-field with low optical absorption losses. A higher Q-factor is helpful to measure small resonance shifts. However, the

confined field inside the resonator reduces field overlap with the surface-adsorbed target analytes and diminishes the sensitivity for biosensing application. Our study focuses on employing the strategies to balance Q-factor and resonance field leakage of dielectric/semiconductor to achieve high overlap with the target bioanalytes for enhancing the sensor's performance. The design can also be tuned according to the target particle's size and shape to achieve higher sensitivity.

1.2 Organization of the thesis

This thesis is organized in 8 chapters starting with the primary motivation of the thesis in chapter 1.

The rest of the thesis is organized as follows:

Chapter 2 is the background chapter. The theory and working principle of different types of plasmonic and dielectric/semiconductor nanoresonators are discussed. Existing works in the literature related to nanophotonic biosensors are briefly presented. This chapter also presents the fabrication and characterization techniques along with the critical sensing performance parameters and loss mechanism of nanophotonic biosensors.

Chapter 3: In this chapter, we present a comprehensive study of the MIM nanopillar-based biosensor, using finite difference time domain (FDTD) simulation. We have discovered the significance of controlled leaky characteristics in plasmonic MIM nanoresonators, and our research prescribes that using an array of controlled leaky resonators instead of high Q resonators could be a promising approach for improving the performance of nanophotonic biosensors while dealing with small size bioanalytes. An array of novel leaky MIM nanopillar geometry ensures uniform sensitivity throughout the device surface. Our study considers the influence of individual MIM nanopillar's geometry (shape, diameter, pitch, insulator layer's thickness), insulator layer's materials, and arrangements of array to achieve high sensitivity for 100 nm and 50 nm sized polystyrene particles. The proposed plasmonic sensing platform has demonstrated

outstanding potential in detecting small size analytes, including SARS-CoV-2, H1N1 virus, and Hepatitis B virus, at ultra-low concentrations.

In the Chapter 4, we present the fabrication process and experimental tests conducted to validate the efficacy of the MIM nanoresonator as a biosensing platform. Two types of MIM nanoresonators were fabricated using the FDTD optimized design and subjected to experimental measurements using varying concentrations of 100 nm sized polystyrene beads. Our study has also uncovered the intricate obstacles involved in fabricating different MIM nanoresonator configurations.

In Chapter 5, this research study focuses on developing a biosensing platform using Au nanoresonators to avoid fabrication issues present in MIM nanoresonators. We have introduced a leaky Au nanoresonator based biosensor design and fabricated the devices for experimental validation. We then biofunctionalized the Au nanoresonators with the anti-SARS-CoV-2 antibody to enable the specific detection of SARS-CoV-2 virus like particles (VLPs). Notably, our biosensor has demonstrated an incredibly low limit of detection (LOD) of 1 VLP μL^{-1}, making it one of the most sensitive plasmonic biosensors available for detecting SARS-CoV-2. The Polymerase Chain Reaction (PCR) technique is indisputably the gold standard for detecting SARS-CoV-2, the virus responsible for the COVID-19 pandemic. The PCR process requires a large sample volume (500 - 1000 μL of the initial sample for viral RNA extraction) and several days to deliver final results, which can be inconvenient. Furthermore, an expert technical person is required to run and analyze the samples. In this context, our established plasmonic biosensing platform is a game-changer in the field of disease diagnosis and has the potential to revolutionize the way we detect SARS-CoV-2, providing unparalleled precision and reliability with very low sample volumes (1 μL of test sample).

In Chapter 6, we present innovative designs of all-dielectric/semiconductor metasurfaces constructed using leaky MoS_2, a biocompatible quantum material for biosensing applications. The field of Mie-resonant metaphotonics has recently emerged, provid-

ing a breakthrough in the confinement and manipulation of resonant optical fields at subwavelength scales. The combination of Mie-resonances with nanostructures made of transition metal dichalcogenides (TMDC) results in a strong coupling between optical modes and excitons within the same nanophotonic system. Our research has pioneered leaky nanoresonator designs using MoS_2 and explored the unique configurations and properties of these resonators. Furthermore, we have conducted a comprehensive analysis of the key factors that significantly impact the detection of small-sized bioanalytes.

Chapter 7 of this thesis presents a novel approach to fabricating a large-area MoS_2 metasurface using leaky MoS_2 split-nanorings array. This groundbreaking study substantiates the novel fabrication process and experimentally demonstrates that MoS_2 Mie-resonator based metaphotonic devices are capable of detecting small analytes (as small as 100 nm), with an impressively low limit of detection. Our findings conclusively establish that the MoS_2 metasurface has immense potential for next-generation quantum sensing applications, opening up a new and exciting avenue for groundbreaking research. Our research findings as a keystone will undoubtedly contribute to 2D material metaphotonics and beyond. With our contributions, we aim to revolutionize the field and inspire future breakthroughs.

Chapter 8 provides a comprehensive summary of the thesis and outlines the potential avenues for future exploration.

Chapter 2

Background

2.1 Biosensors

A biosensor is an analytical device that transduces biological or chemical reactions to measurable electrical or optical signals. During the post-covid pandemic, biosensors are now unavoidable for biomedical diagnosis and widely used in other areas such as, point-of-care monitoring of disease progression [25],[26],[27], environment monitoring [6], drug discovery [28], food process control [29], forensics [30] etc. Biosensors can be classified into different groups such as, optical, electrochemical, thermoelectric, and piezoelectric. Optical biosensors offer many advantages due to their compact dimensions (few nanometers to few microns), high-speed operation, sensitivity, and robustness [31], [32]. Optical biosensing performs by exploring the interaction of the optical field with the biological molecules, analytes and converts the concentrations, or biological events to measurable optical signals in terms of fluorescence, luminescence, surface plasmon resonance, absorption spectroscopy and scattering of light [31]. Different types of optical biosensors are used for detecting enzymes [33], [1], antibodies [34], antigens [35], nucleic acids [36],[37], cells and tissues [38] as biorecognition elements. There is a wide range of optical biosensors as described below.

1. Light scattering-based biosensing: This is an analytical technique commonly used in the pharmaceutical industry to determine the sizes of biomolecules for drug formulation. The scattered light intensity of most of the biomolecules is

weak. Therefore, a high volume of bioanalytes is required to characterize them. This technique was successfully used for quantitative detection and analysis of various chemical [39] and biological molecules [40].

2. Fluorescence-based biosensor: Fluorescence lifetimes are very sensitive to the change in the local environment of fluorophores and measure the efficiency of FRET (Förster Resonance Energy Transfer). Fluorescence lifetimes are important to study the complex structures in intra-cellular processes [41].

3. Optical waveguide interferometer biosensor: In this configuration, the sensing region is located in one waveguide arm and the light signal propagating through the other waveguide arm works as a reference signal. The evanescent field generated along the waveguide detects the local change in refractive index occurring at the active sensing region, producing a phase difference in the optical signal. In [42], a multimodal waveguide interferometric sensor design was proposed and the theoretical limit of detection 1.9×10^{-7} refractive index unit (RIU) was achieved. A. Psarouli et al., [43] reported a broad-band Mach-Zehnder interferometer (BB-MZIs) biosensor to detect C-reactive protein (CRP), a vital cardiovascular disease marker in human serum samples, and the detection limit of the proposed immunosensor was 2.1 ng/mL.

4. Fabry-Perot resonator biosensor: In a typical Fabry-Perot cavity resonator the light is reflected back and forth inside the resonator itself and emits from one end, which interacts with the target biomolecules bind on the surface [44].

5. Microresonator-based biosensor: Microresonator could be of different structures such as a microdisk, microring, microsphere, microtoroid resonator, illustrate the whispering gallery mode (WGM) resonator mode, where the mode field is circulating around the concave surface of the structures and the internal reflections from the curved surface of resonator make the light wave traveling

around the structure. Anderson et al., [45] reported a WGM resonator-based biosensor for Helicobacter hepaticus bacteria detection.

6. Photonic crystal (PhC) resonator biosensor: Photonic crystals are of three types: One dimensional (1D), two-dimensional (2D), and three-dimensional (3D) systems. In a 1D photonic crystal, a stack of high and low refractive index materials is fabricated where the light can propagate through the periodic change of refractive indices of the materials. 2D photonic crystals are typically developed either through etching holes in the substrate made of high refractive index materials (e.g., silica or glass substrates with etched holes) or, by fabricating 2D periodic arrays of nano/micropillars. In a 3D photonic crystal, the refractive index of constituent materials vary periodically in three directions. T. Endo et al., [46] fabricated a 2D nanohole array using nanoimprint lithography (NIL) technique on cyclo-olefin polymer thin film (100 μm) for the detection of CRP in human serum with the detection limit of 12.24 pg/mL. Leest and Caro [47] have reported the optical trapping of single bacteria (B. subtilis and E. coli) in the 2D PhC cavity-enhanced evanescent field.

7. Surface plasmon resonance biosensor: When the incident excitation matches with the natural frequency of the conduction electrons present on the surface of the noble metal nanostructures, surface electrons start to oscillate. Oscillating electrons produce wavelets and propagate along the metal surface as a surface or evanescent wave. It utilizes the evanescent field in close proximity to the biosensor surface to detect the biorecognition element with the analytes. A brief description of the working principle is provided in the following section.

2.2 Nanophotonic devices for biosensing

The major goal of point-of-care (POC) diagnostic systems is to achieve fast response time, independent of laboratory infrastructures, and diagnosing different diseases

without any pre-labels and with a smaller amount of test sample to obtain good sensitivity. Nanophotonics involves the light-matter interactions with the plasmonic metal, dielectric, semiconductor nanostructures enabling strong confinement and near-field enhancement of optical field in the sub-wavelength (nanometer dimension) regime, which dramatically boost the bioanalytes detection sensitivity. Resonant nanophotonic devices act as the fundamental building blocks for real-time, label-free, non-invasive rapid detection of bioanalytes making this approach unique to other techniques such as enzyme-linked immunosorbent assay (ELISA) [48], fluorescence lifetime imaging (FLIM) [49].

Most of the nanophotonic biosensors are based on the evanescent-field principle to probe the target bioanalytes. This evanescent field generated surrounding the nanophotonic structures decays exponentially along the axis perpendicular to the sensing surface with a decay length of a few nanometers to a few hundred nanometers. This important feature of strong surface localization is essential and the optical field is sensitive to the modifications of the dielectric environment on the sensor surface, which enhances the light–matter interaction. The evanescent field generated on the active sensing surface interacts with the bioanalytes, real-time chemical and biomolecular interactions occurring at the active sensor surface directly transduce in terms of change in resonance wavelength, intensity, and/or, phase of the light. Thus, the device can record the real-time dynamics of any biomolecular interaction (for example, an antibody–antigen interaction) [50].

The nanophotonic biosensors could be broadly categorized into two: (i) nanoplasmonics systems and (ii) dielectric/semiconductor nanophotonic systems. Brief descriptions of each category are in the following subsections.

2.2.1 Working of metal and metal-insulator-metal Plasmonic biosensors

Long time before scientists discovered the optical properties of metal nanostructures, in 4^{th} century AD artistry of famous Lycurgus cups was decorated by gold nanoparticles of different sizes and shapes to create the colors. The scientific investigation by Gustav Mie [51] and Rufus Ritchie [52] of metal nanoparticles and flat metal surface breakthrough the research area of plasmonics. Localized surface plasmons (LSPs) are the collective oscillations of free electrons on the surface of subwavelength dimension metal nanostructures. When the incident excitation frequency matches with the conduction electrons' oscillation frequency, a strong electric field is produced due to the induced positive charges and electron clouds in the vicinity of the plasmonic metal nanostructures (see Fig.2.1). Localized surface plasmon resonance (LSPR) of a spherical nanoparticle under the incident light's electric field (E(t)) has been depicted in Fig.2.1. The excitation wavelength of LSPRs depends on the metal nanostructure's size, shape, elemental composition (mostly noble metals e.g., Au, Ag, Pt), and surrounding local dielectric environment [53], generally in the range of visible to near-infrared (NIR) region of the spectrum. Surface plasmon resonance (SPR) has been used for biosensing applications for the last two decades. SPR biosensors provide real-time analysis [54], an important tool for studying biomolecular interactions in life sciences and pharmaceutical research [55].

Surface plasmons are evanescent in nature because the oscillations of the free electrons are out-of-phase with the incident light wavelength and tend to cancel the incident excitation wave. If the dielectric constants of the two materials (such as, plasmonic metal and surrounding dielectric medium) are of opposite sign (i.e., $\epsilon_1 = -\epsilon_2$), surface plasmons can only exist at the interface between a metal ($\epsilon < 0$) and a dielectric medium ($\epsilon > 0$) as shown in Fig.2.1. Thus, the plasmonic system is composed of electromagnetic waves in the dielectric medium and oscillating plasma. Free electrons and positive ions in the metal are considered as the plasma whose density oscillates

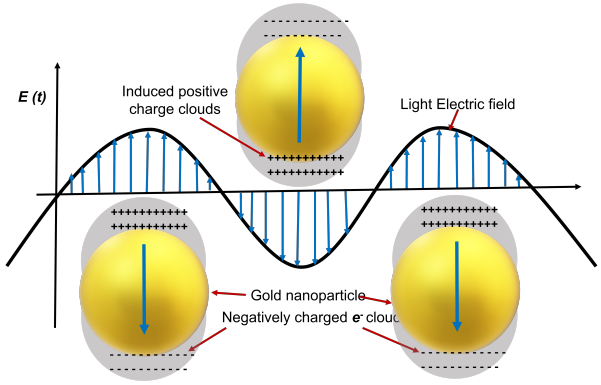

Figure 2.1: Spherical gold nanoparticle under the electric field of incident light shows the polarizations of electron clouds, which produces localized surface plasmon resonance field surrounding the nanoparticle.

with the fundamental frequency (ω_p). The plasma frequency (ω_p) of a bulk metal is defined as follows [56]:

$$\omega_p = \left(\frac{Nq_e^2}{\epsilon_0 m_e}\right)^{\frac{1}{2}} \tag{2.1}$$

where N is the number of atoms per unit volume, q_e is the electron's charge, m_e is the electron's mass and ϵ_0 is the permittivity of air. The working of different types of surfaces plasmon resonator systems is discussed below.

Propagating surface plasmons (PSPs)

Surface plasmon polaritons (SPPs) are the electromagnetic excitations propagating along the interface between a metal nanowire and a dielectric material (air in this case) as shown in Fig.2.2. This was first observed by R. W. Wood while conducting reflection measurements on metallic gratings in 1902 [57]. When the incident wave is p-polarized, the oscillating electric field will excite surface charges at the interface between the metal and the dielectric, and the surface charges undergo a collective oscillation. Although the wave is totally reflected at the interface there are oscillating

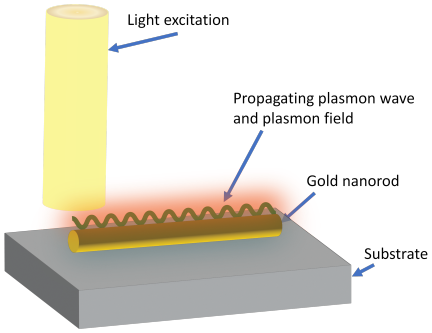

Figure 2.2: Illustration of propagating surface plasmons on the surface of a gold nanorod upon incident excitation.

charges which have associated radiation fields penetrating the metal. The plasmonic field is the spatially decaying evanescent field in the direction normal to the interface. At the critical angle of incident light, the decay length is infinite, but when the angle of incidence is higher than the critical angle, the decay length falls off rapidly to the order of the wavelength of light. Propagating surface plasmons are the electromagnetic waves propagating on the surface of metal nanorods (see the schematic in Fig.2.2), along the boundary of metal and dielectric medium. When the incident light excites the surface plasmon polariton (SPP) mode on a flat metal thin film or, nanorod, SPP modes propagate on the metal-air boundary. They comprise an electromagnetic wave that is coherently bound with the collective motion of mobile charges on the surface of the metal; this coherent interaction leads to the PSP having greater momentum than that of a free photon of the same frequency. However, due to the high absorption loss of metals, propagation loss becomes critical and imposes limitations on propagation distance. Extensive research being conducted to overcome the challenges of long-range propagation of SPP modes [58], [59]. M. Khodami et al., [60] reported long-range surface plasmon waveguide modes for bulk refractive index sensing and Bovine serum albumin (BSA) protein detection.

Localized surface plasmons resonance (LSPR)

When surface plasmon resonance is confined near the surface of the metal nanostructures (e.g., Au nanodisks, Au nanotriangles, etc.), known as localized surface plasmon resonance (LSPR). In the schematic Fig.2.3, the LSPR field is localized near the surface of Au nanodisks, upon resonance excitation. LSPR mode is different than PSP, which propagates along the metal–dielectric interface upon resonance excitation. Localization and enhancement of LSPR's plasmonic field in the subwavelength dimension are advantageous for small biomolecule detection applications.

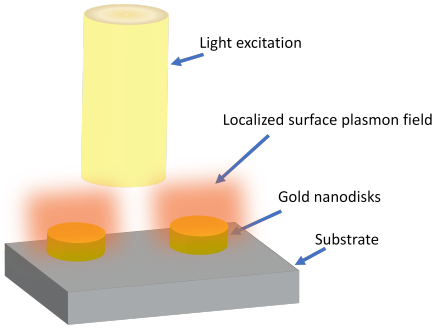

Figure 2.3: Localized surface plasmon resonance field in the vicinity of gold nanodisks upon resonance excitation.

The Mie solution to Maxwell's equations describes the extinction cross-section of the metal nanoparticles.

$$\sigma_{ext} = \sigma_{scat} + \sigma_{abs} \tag{2.2}$$

σ_{ext} is proportional to the $\frac{\epsilon_2(\omega)}{[\epsilon_1(\omega)+2\epsilon_m]^2} + \epsilon_2(\omega)^2$ [61]. Here, $\epsilon_1(\omega)$ and $\epsilon_2(\omega)$ are the real and imaginary parts of the dielectric function of metal nanoparticles, and ϵ_m is the dielectric medium surrounding the metal nanostructure. The surface plasmon absorption band appears when $\epsilon_1(\omega) = -2\epsilon_m$ and the extinction cross-section (σ_{ext}) becomes maximized, and then the metal nanoparticle is at its resonance. Bandwidth and peak absorption of surface plasmons are dependent on $\epsilon_2(\omega)$. However, the size and shape of metal nanoparticles are significant factors for achieving strong LSPR signals. For a spherical metal nanoparticle with a size (diameter) of particle $d << \lambda$ (wavelength

of incident light), the optical properties follow the Mie theory [51]. External electric field drives surface electrons with the same frequency and phase and produces an oscillation dominated by the electric dipole mode. Depending on the size and shape of metal nanostructures, dipolar modes vary, modifying the LSPR signal too. For example, metal nanorods support two types of surface plasmon modes: transverse mode along the short axis (width of nanorod) and longitudinal mode along the long axis (nanorod length). Two important parameters for tuning LSPR characteristics are the effective radius

$$r_{eff} = \frac{3V}{4\pi})^{\frac{1}{3}} \tag{2.3}$$

where V is the volume of a nanostructure, and the aspect ratio (AR) of nanostructures is as follows

$$AR = \frac{long - axis}{short - axis} \tag{2.4}$$

For example, an Au nanorod has a larger cross-section than a spherical shape Au nanoparticle. Interestingly, with increasing the r_{eff} or AR, the restoring force weakens due to electric charge separation and thereby localized plasmonic field becomes stronger. The plasmonic field enhancement is stronger at the edges of metal nanostructures with sharp edges (for example, nanotriangles, nanocrescents, etc.), whereas Au nanoparticles (of isotropic shape) with equivalent effective radius, plasmon oscillation is equally distributed over the surface. Besides the size, and shape of metal nanostructures, surface plasmon resonance also depends on dielectric properties in its surrounding local environment for example, the buffer solution, surface adsorbed biomolecules, etc. The surface plasmon resonance peak shifts to a longer wavelength (red-shift) with the increase in the refractive index of the surrounding medium due to the retardation in plasmon oscillation.

Characteristics of LSPR such as resonance wavelength (λ_r), resonance linewidth (full width at half maximum (FWHM) at resonance wavelength), and resonance peak intensity (I_r) depend on structural parameters such as size, shape, and constituent

materials (i.e., Au, Ag, Pt etc.). Generally, biosensing using LSPR-based devices is performed by observing the shift in resonance wavelength with the binding of analytes on the device surface. The reason is wavelength shift is directly proportional to the molecular adsorption on the surface of plasmonic nanostructures. However, depending on the shape and size plasmonic field concentrates specific regions of the metal nanostructures. There are various LSPR systems reported for virus [62], bacteria [63], protein [64], DNA hybridization [65] and cell [66] detection.

Gap surface plasmon resonance (GSPR)

Gap surface plasmon (GSP) systems are a type of truncated metal-insulator-metal (MIM) nanoresonators. A typical GSP resonator consists of two metal strips of width (w) and thickness (t), separated by a dielectric spacer of height (d). Among other multilayer stack structures, the metal-insulator-metal (MIM) configuration-based GSP resonator is preferable compared to insulator-metal-insulator (IMI) resonators because of its high Q-factor and strong confinement of resonance field. The insulator layer's material and thickness play a crucial role in tuning the resonance characteristics of MIM GSP resonators. Here, we discuss GSP-based MIM nanoresonator systems obtained by truncating the metal and insulator layers. Because of the terminations of the MIM structure, multiple reflections of light can be achieved, resulting in lateral standing-wave GSP modes. The GSP mode is created because the two out-of-phase currents in the two gold strips produce a E-field minimum illustrating magnetic dipole (MD) mode (maximum of the H-field) in the dielectric spacer layer between the two metal strips. MIM GSP nanoresonators are of three different types: configuration I: truncated all three metal and insulator layers (Fig.2.4a), configuration II: truncated top metal and middle insulator spacer layers fabricated on a metal film act as a mirror (see Fig.2.4b), and configuration III: Fig.2.4c truncated top metal layer on stacked films of insulator and metal layers.

When the insulator layer thickness (i.e., the gap between two metal layers) is $\leq$

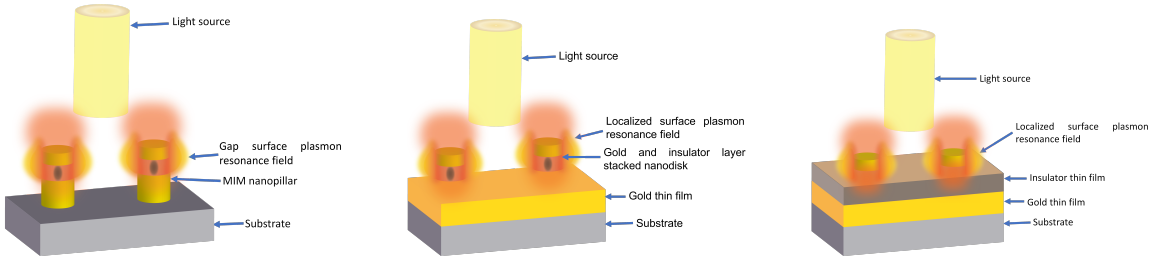

(a) configuration I (b) configuration II (c) configuration III

Figure 2.4: Schematic illustration of different metal-insulator-metal (MIM) nanoresonator configurations.

50 nm (much smaller than the incident wavelength), then Fabry-Perot type resonances create GSPs in individual MIM nanoresonator [67]. Interestingly, when the insulator layer thickness increases, GSP resonance field confinement weakens, and scattering losses become dominant. Also, the increased dimension of the top metal nanostructure enhances scattering and radiation losses [68]. L. P. Hackett et al., [69] reported a plasmonic MIM nanocup array for sensing cancer biomarker carcinoembryonic antigen (CEA) with a limit of detection of 10 ng/mL. The plasmonic MIM cavity-enhanced field interacts with the biomolecules bind on the top gold layer surface and the extraordinary optical transmission (EOT) intensity increases at the resonance wavelength, which quantifies the biomolecules.

2.2.2 Working of dielectric and semiconductor nanophotonic biosensors

Optical resonances in nanostructures made with low absorption, high refractive index dielectric materials (e.g., TiO_2) [70], and semiconductors (e.g., Si [71], Ge [72], etc.) can also facilitate light manipulation at nanoscale. Therefore, sensing devices based on such sub-wavelength dimension nanostructures offer the opportunity to manipulate light confinement. Recent progress in silicon photonics and high-refractive index material-based meta-optic systems have drawn large attention to various applications such as prostate-specific antigen (PSA) detection [73], breast cancer biomarker [74] detection.

Nanostructures made of high refractive index low loss dielectric or semiconductor materials provide Mie-like resonances in the visible wavelength range [75]. The interplay between electrical and magnetic resonances can be tuned by modifying the geometry of resonant nanostructures [76]. The electric dipolar (ED) resonance is created by the collective polarization of the resonator material with the incident excitation light's electric field component. The magnetic dipolar (MD) resonance mode is generated due to the coupling of incoming light with the circular displacement current loop of the electric field inside the dielectric/semiconductor material [77]. This happens if the nanoresonator's dimension is comparable to the wavelength inside the nanoresonator itself, which means $2R \approx \lambda/n$, where n is the refractive index of the nanoresonator's constituent material, and R is the nanoresonator's radius, and λ is the incident light wavelength. This clearly indicates that to achieve such geometric resonance in the subwavelength dimension, the nanoresonator's material should possess a high refractive index. Efficient coupling with the displacement current inside the dielectric/semiconductor nanoresonator needs significant retardation of the electric field. This happens due to the multiple reflections inside the nanoresonator and a prominent phase shift of the electric field. The geometry of the nanoresonator plays a significant role to achieve this magnetic dipolar mode, as the phase retardation will not occur if the nanoresonator's dimension is shallow. When the height and diameter of the nanoresonator increase, a large fraction of the current loop fits well inside the high-index nanoresonator material itself. The controlled leaky characteristics of the resonance field can be introduced with an effective design of the nanoresonator.

The strong near-field enhancement in the hotspots generated in the vicinity of individual dielectric/semiconductor nanoresonators originates strong interaction with the bioanalytes bound to the surface. Binding the analytes on the nanoresonators surface modify the local refractive index, which induces a shift in resonance wavelength or change in intensity. A highly sensitive and responsive device could be developed

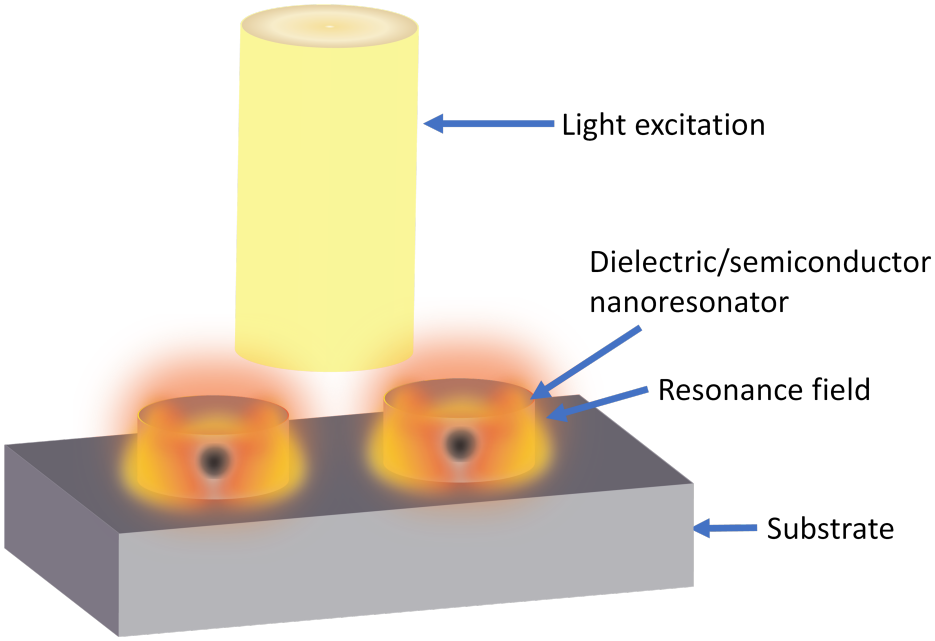

Figure 2.5: Mie resonance in a dielectric/semiconductor nanodisks upon resonance excitation.

by carefully designing the metasurface for the detection of a particular analyte. In dielectric/semiconductor nanostructures, experimental realization of high-Q modes such as, Fano resonances [78], [79] is achieved by breaking the in-plane geometrical symmetry of the unit-cell and these modes are efficient for biosensing applications [80].

2.3 Key Parameters for Biosensing

Here we discuss the key parameters that govern the integrated photonic/plasmonic biosensors. When a sample of bioanalytes is delivered to the designated active sensing region and attached to the functionalized surface of the biosensors, molecular binding occurs between the functionalized surface and the target analytes. Consequently, the effective local refractive index on the device surface changes with the concentration of bioanalytes. The evanescent waves generated from the confined photonic/plasmonic modes interact with the attached bioanalytes and influence the resonance properties (i.e., resonance wavelength, resonance linewidth (FWHM), resonance peak intensity,

etc.). This leads to a shift in the excitation wavelength or relative intensity changes at the wavelength peak.

1. Sensitivity: One of the crucial parameters of a biosensor is the sensitivity to detect any bioanalyte, which maps the physical change upon the attachment of bioanalytes onto the active sensing surface of the sensor. The sensitivity of the photonic/plasmonic biosensor is often defined as the ratio of the shift in resonance wavelength denoted as $\Delta\lambda_r$ to the device surface refractive index unit (RIU) change (Δn)

$$S_\lambda = \frac{\Delta\lambda_r}{\Delta n} \tag{2.5}$$

The relative change in intensity at the resonance wavelength (defined as ΔI_r) also be used as a sensitivity parameter

$$S_I = \frac{\Delta I_r}{\Delta n} \tag{2.6}$$

where Δn (in RIU) is the change in local refractive index on device surface. The sensitivity of the nanophotonic biosensors can be categorized into two:

- Bulk sensitivity: Bulk sensitivity is the change in photonic/plasmonic mode effective index to the change in the refractive index of the surrounding medium of the resonator. For example, when the sensor chip is dipped into a solution bath, the surrounding refractive index changes, and thereby it induces a change in resonant mode also.
- Surface sensitivity: When the surface of the resonator, where the mode is typically confined or the evanescent field of resonator mode is available, is coated with the thin layer of bioanalyte to be detected, the mode effective index changes with the thickness of the adsorbed layer of bioanalytes.

2. Figure of Merit: The figure of merit (FOM) is an essential metric of biosensors, which signifies the sensing performance defined as

$$FOM = \frac{Sensitivity}{FWHM} \tag{2.7}$$

The limit of detection (LOD) of the biosensor is defined as the minimum amount of detectable variation in the resonance parameter, which can be resolved by the measurement equipment. Smaller size and low concentration (e.g., a few pM) of bioanalytes could reflect a slight shift in λ_r. However, in experimental measurements more significant shift in wavelength ($\Delta\lambda_r$) per small change in concentration of bioanalytes on the device surface is expected to achieve higher S_λ and FOM of the biosensor. Following we discuss the major parameters which signify the resonance conditions of photonic and plasmonic resonator-based sensing platforms.

3. Quality factor: The Q factor is an important parameter to measure the performance of both the photonic and plasmonic resonators. It reflects the length of life of the photon in the resonance cavity and the sharpness of the resonance relative to its central frequency. The Q factor is formally defined as the ratio of the stored energy circulating inside the resonator to the energy lost per optical cycle:

$$Q = \omega_0 \frac{E_{stored}}{E_{lost}} \tag{2.8}$$

Here, ω_0 (rad/sec) is the resonance frequency of the resonator. E_{stored} represent the stored energy (Joule) and E_{lost} is the energy lost per each cycle of the resonator. The high Q factor indicates that microcavity has strong photon storage ability and a long photon lifetime. The Q factor can be expressed as:

$$Q = \frac{\lambda}{\delta\lambda} \tag{2.9}$$

where λ (in nm) represents the center wavelength of the resonant mode, and $\delta\lambda$ (in nm) represents the full width at half maximum (FWHM) of the resonant mode.

4. Limit of detection (LOD): Limit of detection is defined as the minimum number or concentration of bioabalytes can be detected. In the experimental measure-

ments, the LOD is extracted by the 3-sigma rule defined as follows.

$$LOD = 3.3 \times \frac{S_{intercept}}{S_{slope}} \tag{2.10}$$

Here, $S_{intercept}$ is defined as the standard deviation of Y-intercepts of regression lines, and S_{slope} represents the standard deviation of the slopes of the linear response curves.

2.3.1 Different Loss Mechanism

As discussed in the above section, the Q factor of the resonator is one of the crucial parameters of nanophotonic devices. Among all the factors, the optical losses in nanoresonators need to be highly considered. The major loss mechanisms directly impacting the device's performance are discussed below.

- Material absorption loss: The material-induced loss from the resonators is mainly due to the material property and processing during fabrication. Such absorption loss plays an essential role in plasmonic and dielectric/semiconductor-based nanoresonators, as noble metals have intrinsic absorption losses due to their high extinction coefficient values [81]. Also, the metal absorbed power generates heat, which can destroy the biomolecules, and proteins bound on the surface. In the case of semiconductor/dielectric nanoresonators, the cavity-enhanced field is expected to enhance the field surface-state absorption per unit distance, given an input optical power. The absorption generates free carriers at the semiconductor/dielectric nanoresonator sidewalls and thus is likely to result in free-carrier absorption.

- Scattering loss: Scattering loss is caused by the surface roughness and contaminants attached to the surface of the nanoresonators. This is primarily due to the defects introduced during fabrication, such as sidewall roughness during the reactive plasma etching (RIE) process. The scattering loss comes from inner and

outer sidewalls in dielectric/ semiconductor nanorings structures. Scattering loss is also significant in plasmonic nanostructures, as the metal deposition and lift-off process also creates roughness in the metal sidewalls. Improvement of the fabrication process can help mitigate the sidewall surface roughness, which usually employs forming and removing an oxidation layer.

- Optical leakage: Optical leakage comes from the resonator's inherent radiation loss, and part of the energy leaks out from the nanoresonator's surface in the form of evanescent waves. With a customized design and material used in nanoresonators, the optical field leak can be controlled and manipulated to utilize it for small bioanalytes detection.

2.4 Fabrication Techniques

There are different techniques to fabricate plasmonic and dielectric/semiconductor nanoresonators. Depending on the feature dimensions, either microfabrication (e.g., photolithography) or nanofabrication techniques (for example, electron-beam lithography (EBL), focused ion beam (FIB), and nanoimprint lithography (NIL)) can be used. Metal layers are deposited by electron-beam evaporation technique, and for dielectric/semiconductor layers, atomic layer deposition (ALD) and pulsed laser deposition (PLD) techniques are used. The brief details of each technique are below.

1. Patterning techniques

    - Photolithography: Photolithography is a high-throughput fabrication method at the microscale. It is the most commonly used fabrication method in the semiconductor industry due to its advantages, such as high reproducibility, high yield, low cost, and mass production availability. Photolithography uses a photomask to cover the photoresist which is a light-sensitive material. There are two types of photoresists: positive and negative tone resist. The photomask is used to transfer the pattern on the photoresist

after exposure to light. Then the patterned substrate could be used to deposit materials (such as metals) in the desired pattern or, used as a mask for etching patterns onto a substrate placed under the photoresist. After the pattern is transferred to the wafer, the photoresist is removed and most of the photoresists are soluble in acetone. The resolution of a photolithography system depends on the wavelength of the light source and the reduction lens system.

- Electron-beam lithography (EBL): Electron beam lithography, commonly known as e-beam lithography is a form of fabrication that produces patterns with high resolution down to sub-10 nm. It does not require a physical mask rather a pattern created in the software is used to guide the electron beam scan to write the pattern directly onto the resist. The electron beam changes the solubility of the e-beam resist, and the resist is then selectively removed using a solvent. The main advantage of the EBL technique is it allows multiple designs to be written together on a substrate and minimum feature size can be achieved down to 5 nm by optimizing the beam voltage, aperture size, and dose of the electron beam. However, the major disadvantage of EBL is a slow and expensive low throughput technique, which is not practical for large-scale productions. Along with that, other disadvantages are Substrate charging and proximity error effects which pose limitations to achieving a high-resolution feature size. In my thesis research, the EBL technique was extensively used to fabricate the metal and MoS_2 nanostructures.

2. Material deposition techniques

- Electron-beam (e-beam) evaporation: This is a physical vapor deposition (PVD) process that can produce a few nm to few μm thin films at low substrate temperature. The e-beam evaporation technique offers a controlled

film structure and morphology with low contamination, and high productivity. The thin film is deposited in a high vacuum chamber (pressure could be 10^{-5} Torr or lower). The material to be evaporated is kept as ingots in a crucible. The current is passed through a tungsten filament leading to the Joule heating and a beam of electrons is emitted a high voltage source is applied to accelerate the electron beam with high kinetic energy and focused on the crucible containing the material to be deposited. The electron beam could be generated by any one of the processes: thermionic emission, field electron emission, or, the anodic arc method. The kinetic energy of the electrons is converted into thermal energy which enhances the temperature on the target material's surface. Evaporated materials are deposited onto the substrate placed at a certain height inside the chamber. The deposition rate can be precisely controlled by tuning the e-beam current and the in-situ measurement is carried out by a quartz crystal monitor. The major advantages of the e-beam evaporation technique are: it allows to reach a very high temperature of the target crucible, which allows for obtaining a high deposition rate, a highly directional deposition technique, and is good for the metal lift-off process, during the film deposition process the purity of the source material is maintained with the water cooling system of the crucible. In our thesis research work, we have used e-beam evaporation technique for depositing Au and Ti (adhesive layer) layers for fabricating the Au and MIM nanoresonators.

- Atomic layer deposition (ALD): Atomic layer deposition (ALD) is a well-known technique for the deposition of high-quality thin film thickness ranging from a single atomic layer to a few hundred of nanometers. In this method, chemical gas reactants (precursors) are supplied into the reaction chamber and the chemical reactions occur that form the thin film layer on the substrate. The precursor gases are pulsed alternately, and each

precursor gas cycle is separated by an inert gas (N_2 or, Argon) purging to avoid any contamination. The thickness of film growth can be controlled by setting up the number of gas purging cycles. In my research work, plasma enhanced atomic layer deposition (PEALD) for Al_2O_3 layer deposition where, the O_2 plasma with Trimethylaluminum (TMA, $Al(CH_3)_3$) precursor sources were used. The unique feature of the ALD technique is self-terminating growth mechanism yields thickness uniformity and good surface morphology deposited on the substrate. One of the important characteristics of the ALD technique is that the film grown by this process is conformal to the substrate surface which means the thin film morphology follows the surface contours resulting in uniform thickness over a full wafer surface. In our research, we have used the PEALD technique for growing the Al_2O_3 thin film layer for fabricating the MIM nanoresonators.

- Pulsed laser deposition (PLD): Pulsed laser deposition works based on the laser-matter interaction. A high-energy pulsed laser beam focused on a target in an ultra-high vacuum chamber (champer pressure $< 10^{-7}$ Torr) or with the presence of some background gas depending on the material to be grown. The target is prepared by compressing the powder to make a solid form with the application of high pressure. Organic polymers and biomaterials are generally in liquid form, which can also be frozen to make a solid target in a matrix-assisted pulsed laser evaporation (MAPLE) system. The plume in the PLD system contains electrons, atoms, molecules ions, clusters, and globules, that reach to the heated substrate. A repeated number of laser pulses leads to the growth of a thin film on the substrate surface. The nucleation process mainly depends on the interface energy between the substrate and the plume material. Different types of high-energy excimer gas laser systems where the laser pulse duration can vary from femtosecond to nanosecond are used to excite the PLD target

and these laser sources can deliver very-high-energy (a few hundred MW) focused beams.

3. Reactive ion etching (RIE): In the dry-etch processes, the lithographically patterned wafer is bombarded with the gas ions, where the resist material works as the masking layer. These processes can etch extremely deep features with vertical side walls. In dry etching processes, plasma is produced inside a high vacuum chamber by a parallel plate configuration and special reactive gas plasma is used for etching a particular material maintaining the selectivity. The inductively coupled plasma reactive ion etching (ICP-RIE) is a special type of RIE method used to fabricate complex micro and nanostructures (for example, trenches, tilted sidewalls, etc.). In a typical ICP-RIE system, a coil is placed in the reactor to produce a magnetic field that narrows down the area of the plasma produced by the RF source and prevents unwanted scattering on the chamber sidewalls contributing to the directionality of the plasma ions. On the other hand, the RF source power was used to accelerate the plasma ions (contributing to the kinetic energy of the plasma ions), and generate the polarization voltage of the etched material. It has been experimentally proven that the RF power is directly related to the etch rate irrespective of the material to be etched [82], [83], [84]. A few special features of ICP RIE are: (a) it is a low-pressure process, (b) anisotropy etching process that means, the etching direction is orthogonal to the substrate surface plane, (c) high selectivity between the masking material and the material to etched, with a controlled high-degree of directionality achieved, (d) separate sources for RF and ICP generators provide specific control over ion energy and ion density, enabling high process flexibility depending on the need of directionality (ICP) as-well-as RF energy. In our research work, we have used SF_6 plasma in Oxford Instruments Cobra ICP RIE system to etch MoS_2 for fabricating the MoS_2 nanoresonators.

4. Metal lift-off technique: Typically lift-off technique is used for patterning different metals (such as Au, Ag, Ti, Cr, Al, etc.) layers using a sacrificial layer such as, photoresist or EBL resist materials to write the patterns on the substrate. The sacrificial layer is coated and pattern writing is then performed using optical or electron beam lithography technique and a metal layer is deposited on top. In the final step, a sacrificial layer (resist material) is dissolved in organic solvents such as acetone, and remover PG, thereby lifting away metal deposited onto it and the rest of the patterns keep on the substrate. In the lift-off technique, important facts are, (a) the sacrificial layer should be thicker than the metal layer thickness so that, there are no wings at the edges left at the side walls, (c) the metal deposition technique should be directional such as, e-beam evaporation technique generally used for metal deposition, that could be lift-off., (d) using two different types of resist on top of another helps to avoid the side walls edge wings creation after lift-off. In our research, we have performed Au layers lift-off to fabricate the Au nanodot structures.

2.5 Characterization Techniques

In our research, we have used several characterization techniques at different steps of the sensor fabrication process. These are described briefly below.

1. Atomic Force Microscopy (AFM): Atomic force microscope works based on the principle of surface sensing by using a cantilever tip. The micro-machined tip raster scans (line-by-line) through the top surface of the sample under investigation. This instrument can work in different operating modes: (a) static or, contact mode, (b) dynamic mode which is sub-divided into tapping mode or, intermittent contact mode, and non-contact mode depending on the surface of the materials. AFM is a non-destructive measurement technique to obtain topography information with a high spatial resolution of the nanostructures and

thin film samples. This technique also can also be used to identify the properties of superconductors and magnetic nanomaterials with a special AFM tip (magnetic material coated) used to record the local magnetic field map.

2. Scanning Electron Microscopy (SEM): In SEM, the electron beam is focused on the sample under study inside a vacuum chamber. The electron beam is generated from either of the three types of guns: (a) tungsten filament: inverted V-shaped wire of tungsten heated to produce electrons, (b) thermionic emission gun based on the solid-state crystal (Lanthanum hexaboride or, Cerium hexaboride): a high-brightness source provides longer lifetime than tungsten source. (c) field emission gun: a very sharp tip made of 100 nm width tungsten provides a high-energy tightly focused electron beam. SEM has a large depth of field, which allows more of a specimen to be in focus at one time. The electron beam is focused through a set of electromagnetic lenses. In our research, we have used SEM to image the nanostructures at different stages of the nanofabrication process (e.g., after EBL pattern writing, after metal lift-off, after etching steps, etc.).

3. X-Ray Diffraction (XRD): X-ray diffraction is an important technique in materials science to identify the crystalline properties of nanomaterials. The basic working principle of XRD is based on Bragg's law [85], The collimated beam of X-ray incident on a specimen sample and atoms present on the crystal planes of the material and the beam gets scattered, diffracted by the atoms along the beam path. The reflected beam from the sample reaches the detector placed at a certain angle with the sample surface, which detects the interference of the scattered/diffracted beam of X-rays. Thus the crystalline structure properties of a particular material are determined. Here, the diffraction peak intensity is plotted against the diffraction angle (2θ is an angle between the incidence X-ray beam and the detector). The narrower and high-intensity peak defines

the crystalline nature of the sample. In most of the thin film analyses, a grazing angle of incidence XRD, where a small incident angle of the X-ray beam is used, to make the diffraction as surface sensitive, because the penetration depth of the beam is limited to the distances of a few nanometers only. In our research, we have used glancing angle XRD for determining the crystalline properties of MoS_2 thin film grown by the PLD technique.

4. Optical Reflection/Transmission Spectroscopy: Optical spectroscopy techniques, such as reflection and transmission, help diagnose optoelectronic materials. Reflection spectroscopy, for instance, measures the intensity of reflected light based on wavelength or frequency. This technique works by detecting photons that have been reflected from the surface of a material, providing essential insights into its composition, structure, and electronic properties. The major components of a typical optical reflection spectroscopy are a light source, detector, and data analysis system. The reflection spectrum of a photonic device can provide valuable information about how the device interacts with incident light. Resonant features appear as peaks or dips in the intensity of reflected light as a function of wavelength or frequency. Multiple spectral peaks/dips occur in the transmission or reflection spectrum as multiple resonance modes can be excited with the incident light source. In the case of optical transmission spectroscopy, the incident light passes through the nanophotonic device fabricated on a quartz/glass substrate, and the detector collects the transmission spectrum. In our lab, we have custom-built a free-space optical reflection spectroscopy to characterize the nanophotonic devices. A broadband unpolarized light source (λ = 360 nm to 2600 nm) was used, and a tabletop spectrometer (Ocean optics USB4000 with resolution of 1.3 nm and wavelength range of λ = 170 nm to 890 nm). The reflection spectrum collected from the nanophotonic device is recorded by Oceanview software.

5. Raman Spectroscopy: When the light is incident on a specimen (for example, a gas, liquid, or, any solid), the photons are scattered by the atoms or molecules and the scattered photons conserve the same energy as the incident photons energy (elastic scattering). However, there are a small number of photons (1 photon in 10 million scatters with different energy compared to the incident photons) and this process is known as inelastic scattering, which is the Raman effect. In the Raman scattering process, the incident photon (of frequency ω_i rad/sec), interacts with the electrons in the sample's crystal lattice, and an electron-hole pair is created. The law of energy and momentum conservation provides $\omega_i = \omega_s \pm \omega$, where ω_i is the incident photon frequency (rad/sec), ω_s rad/sec is the scattered photon frequency and ω (rad/sec) is the frequency of the phonon created (or annihilated) during the photon electron interaction. The scattering is known as Stokes scattering when the frequency changes to a higher frequency and anti-stokes scattering when the photon frequency reduces. The Raman shift is defined by the frequency difference $\omega_i - \omega$. In my thesis research Raman shift was used to find the number of monolayers present in MoS_2 thin film sample while optimizing the thickness of PLD grown MoS_2.

6. Optical Microscopy: A magnified image of an object (size in the order of microns) by the standard optical microscope. The objective lens of a certain magnification (generally used objective lenses: 2.5X, 5X, 10X, 20X, 50X, 100X, etc.) is used to focus and collect the light from the specimen and an eyepiece is used for the user to observe it. In my research, an optical microscope has been used at several stages during fabrication, before and after measurements of the fabricated devices.

2.6 Surface Functionalization

The surface functionalization process is an indispensable step in the development of biosensors. By integrating biorecognition elements onto the biosensor, it is possible to effectively detect the specific analyte of interest. The process of biofunctionalization entails chemical modification of sensor's surface that facilitates the immobilization of bioreceptors while simultaneously preventing non-specific adsorption of matrix components present in biological samples. In label-free nanophotonic biosensing platforms, analyzing non-treated clinical samples such as blood, serum, plasma, urine, and saliva poses a major challenge as they contain a variety of compounds that differ significantly among patients. The adsorption of non-relevant molecules to the active sensor surface can produce high background noise or even false positive signals. To prevent this unwanted signal interference, it is essential to minimize the undesired adsorption by employing proper functionalization steps during biosensor development. The specific affinity between the biorecognition element and the target analyte defines the selectivity of a biosensor. Few examples of bioreceptors are enzymes, antibodies, nucleic acids (DNA), aptamers, etc.

Chapter 3

Optimization of a Leaky Plasmonic Metal-Insulator-Metal Nanopillar Array for Low Concentration Biosensing Applications[1]

Dipanjan Nandi[1], Md. Zahurul Islam[1,2], and Manisha Gupta[1*]

[1]Department of Electrical and Computer Engineering, University of Alberta, Edmonton, Alberta, Canada.

[2]Department of Electrical and Electronic Engineering, Bangladesh University of Engineering and Technology, Dhaka, Bangladesh.

3.1 Abstract

The research focuses on optimization of leaky metal-insulator-metal (MIM) nanopillars array design for the detection of sub-100 nm virus. Here, we have explored different MIM nanopillar and array geometries along with the insulator layer material to tune the plasmonic field leakage. For the optimized design we observe a sensitivity of surface refractive index change - 101.68 nm RIU^{-1}. Using 100 nm diameter polystyrene particles, a sensitivity of 17.66 nm/decade was achieved with detection

[1]This manuscript is published as D. Nandi, Md. Z. Islam, and M. Gupta, "Optimization of a leaky plasmonic metal-insulator-metal nanopillar array for low concentration biosensing applications", Journal of Optical Society of America B, vol: 39, issue: 10, pp. 2705-2713, 2022, doi: https://doi.org/10.1364/JOSAB.468244

limit of 1 particle. The optimized structures thus demonstrate a homogeneous surface sensitivity over large active sensing area for sub-100 nm virus detection.

3.2 Introduction

Emergence of nanotechnology finds diverse applications in medical diagnostics, cancer therapy, drug delivery to individual biological cells, and biomolecule sensing. There are plenty of variations in size and shape of biological molecules, sub-cellular organelles, different viruses, and bacteria [86]. Bioanalytes possess low refractive index (RI $\sim$ 1.3-1.5) and do not create enough refractive index contrast with the surrounding environmental medium (e.g., air or water medium) [87, 88] which makes single small size analyte detection challenging. In current COVID-19 time, the point-of-care diagnostic instruments have become significantly important for secure and quick detection of bioanalytes with ultra-low number density (a few pM or single molecule resolution). Traditional nanophotonic devices such as, microring resonators [89, 90], whispering gallery mode (WGM) resonators [91, 92], slotted nanobeam cavity [93, 94], and photonic crystal (PhC) based devices [95–97] have drawn significant attention as non-invasive biosensing platform for the last few decades. There are numerous plasmonic metal and metal-insulator-metal (MIM) nanostructure-based platforms to achieve strong light confinement and enhancement for biosensing applications, e.g., gold bowtie nanoantenna array with MIM configuration [98], Au crescent nanodisk array [99], one-dimensional Au nanogroove array [100] and plasmonic nanocavity [101]. The primary objective of these resonant nanophotonic devices is to achieve strong confinement of light in a small modal volume (V_m), thereby attaining high Q-factor (approximately 100) in a small V_m ($\sim$ 40 nm^3) and employ them for bioanalyte detection. There are several metrices that are used to measure performances of a photonic or, plasmonic resonator-based sensor, e.g., sensitivity, Q-factor, resonant linewidth (full-width at half maximum (FWHM) at the resonance wavelength position, along with device sensing performance metrices: figures of merit (FOM) and limits of detec-

tion (LOD). For a refractometric sensor, the device sensitivity is often defined as the change in resonance wavelength ($\Delta\lambda_{res}$), or resonance intensity (ΔI_{res}), per refractive index unit (RIU) change. Device sensitivity is greatly dependent on the confined resonant field overlap with the bioanalytes, which induces a shift in λ_{res} and/or, I_{res}, or create resonance frequency line width broadening or, splitting [91].

However, the above mentioned biosensing platforms require immobilizing the target analyte on the specific active sensing region of the nanophotonic devices precisely, as misalignment with the confined optical field could affect the single particle detection sensitivity [95]. During the global health emergency major challenge arises with the targeted delivery of sample to the designate active sensing region of device, when utilized outside of the controlled laboratory conditions. Also, the plasmonic field on the surface of metal nanostructures evanescently decays into air, thus resonance linewidth becomes broader (larger FWHM) and it weakens the sensing performance of the plasmonic devices. Therefore, it is crucial to develop a larger active sensing area (approximately few μm^2 to few hundreds μm^2) platform with homogeneous sensitivity over the whole active sensing surface to reduce the challenges related to targeted delivery of bioanalytes. To detect the bioanalytes attached on the surface, it is necessary to have tightly confined plasmonic modes near the surface (top and/or, sidewall surfaces) to achieve higher surface sensitivity. In this context, leaky metal-insulator-metal (MIM) nanoresonators are introduced where the resonating field leaks out to the surface and evanescently decaying to the surrounding medium. Larger active area photonic sensors such as, gold mushroom array [102], MIM nanocup array [103, 104], MIM capped polymer nanopillar array [105], MIM nanocube array [106] for biosensing applications have been demonstrated. Here we aim to develop a large active sensing area nanophotonic sensor with leaky MIM nanopillar design-based approach.

In this article, we propose a novel design of leaky MIM nanopillars array device for detecting hepatitis B virus (diameter of $\sim$ 50 nm), H1N1 influenza virus (diameter of $\sim$ 100 nm) [95, 107] separately. Here we present a tuneable nanophotonic design

where manipulation of optical field leak in individual MIM nanopillar can be controlled by exploring different geometry (shape, size, thickness) and materials of the individual MIM nanopillars. We aim to explore the prospect of how efficiently the leaky nature of a MIM nanopillar and plasmonic field coupling with the neighbouring nanopillars can be promoted to establish a large active sensing-area based nanophotonic sensor platform for sub-100 nm sized bioanalytes detection. Finite-Difference Time-Domain (FDTD) (Ansys-Lumerical Inc. (c) [108]) method has been used to numerically solve the full-field vector Maxwell's equations for the proposed device and simulate its performance. Major application of the proposed nanophotonic device would be a portable sensor for the detection of small size bioanalytes with ultra-low concentrations.

3.3 Sensor Design

Optical response of a single MIM nanopillar was explored as a function of lateral geometric shapes (cylindrical, elliptical, hexagonal, square, and triangular), diameter (ranging from 100 nm to 1 μm), insulator layer materials (Al_2O_3 and TiO_2) and thickness of the insulator layer (from 10 nm – 100 nm). These parameters directly impact the plasmonic field, balance between optical field leak and plasmonic near-field localization around the top and sidewall surfaces of each nanopillar [109]. Here we have used gold (Au) metal layers in nanopillar structure as Au is a widely used plasmonic metal and chemically stable metal (less chance of oxidation compared to other plasmonic metals e.g., Ag, Cu & Pt etc.) [110]. A monochromatic ($\lambda = 532$ nm with wavelength span $\Delta\lambda = 1$ nm) unpolarized total-field scattered-field (TFSF) source was incident into the MIM structure on glass substrate to excite localized surface plasmon resonance (LSPR) in the Au-insulator interfaces of the MIM nanopillar. A schematic view of the square-shaped nanophotonic sensing platform consisting of two-dimensional (2D) array of MIM nanopillars on a glass substrate is shown in Fig. 3.1 along with the axis directions used for the simulations. The localized plasmonic field

surrounding the MIM nanopillars interacts with the polystyrene particles distributed on the surface and the field intensity recorded on the top of particles with a 2D monitor. For these simulations, we have used TFSF source, a plane wave source with perfectly matched layer (PML) boundary conditions in all three coordinate directions (X, Y and Z) to prevent any reflection from the boundary. As we are studying the relative change of $\boldsymbol{E}$ field intensity in the presence of the polystyrene particle; TFSF and the PML boundary condition ensures that there is no reflection from the boundary which can modify the relative intensity change due to the polystyrene particle. Here, 532 nm excitation wavelength has been used because Au surface plasmon peaks appear in the range 520 nm to 560 nm [111] and there is existing work where 532 nm excitation was used to excite surface plasmon resonance of Au nanostructures [112], [113], [114]. We also conducted tests using different excitation wavelengths such as, 405 nm, 532 nm, and 808 nm, but found that 532 nm excitation source provides stronger surface plasmon enhanced field confinement surrounding the Au nanostructures. We have considered an optically thick 90 nm Au as the bottom mirror layer ($<$ 10 % transmission for 50 nm thin Au film at $\lambda = 532$ nm [115]) and partially transparent 20 nm Au ($\sim$ 40% transmission at $\lambda = 532$ nm [115]) as the top metal layer, as shown in the inset of Fig. 3.2(a).

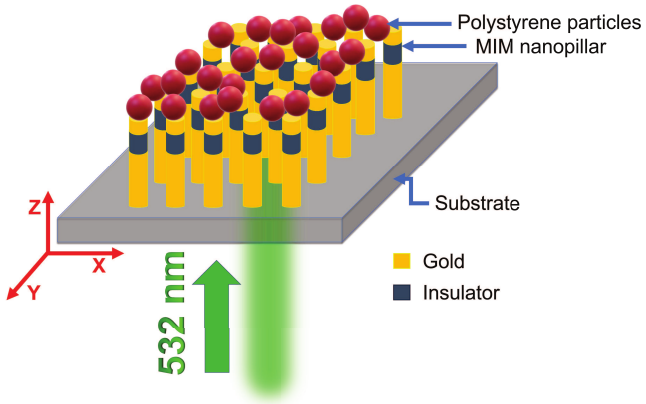

Figure 3.1: A schematic view of the planar two-dimensional (2D) square shape array of MIM nanopillars with particles to be detected shown. Light source incident from the $+Z$ axis direction. $\boldsymbol{E}$ field intensity is recorded by a two-dimensional monitor placed on the top of particles.

In this MIM nanopillar design, we have chosen thicker Au (90 nm) metal layer at the bottom, so that, plasmonic field at metal-insulator interface is reflected and a thinner Au layer (20 nm) on top in order to leak out the field. This structure allows us to vertically outcouple the resonant field at the top surface of individual MIM nanopillar. Considering cylindrical shape with 100 nm diameter of single MIM nanopillar, we have separately used two different insulator materials, Al_2O_3 (refractive index $n = 1.77$, extinction coefficient $k = 0$ at wavelength, $\lambda = 525$ nm [116]) and TiO_2 ($n = 2.67$, $k = 0$ at $\lambda = 529$ nm [117]), of varying heights ranging from 10 nm to 100 nm and recorded the average $\boldsymbol{E}$ field intensity (at $\lambda = 532$ nm and normal incident excitation by an unpolarized TFSF source along the $+Z$ axis direction) on top of single MIM nanopillar, which is plotted in Fig. 3.2(a). We have also recorded the field intensity on top of an Au nanopillar of 100 nm diameter and 150 nm height which is presented by the blue triangle in Fig. 3.2(a) for comparison with the MIM nanopillar.

Insulator layer's refractive index and thickness are crucial to control the leaky characteristics of the MIM nanopillar. To better understand leaky characteristics, we have plotted field distribution (see top-view Fig. 3.2(b-d) and side cross-sectional view Fig. 3.2(e-g) of a MIM nanopillar choosing Al_2O_3 as the insulator layer material. Selecting the correct insulator layer (Al_2O_3) thickness is important and determines the amount of plasmonic field generated at the metal-dielectric (here two Au-Al_2O_3 interfaces) interfaces which can outcouple to the outer surface. Thus, $\boldsymbol{E}$ field intensity distribution on the top and sidewall surfaces of single MIM nanopillar is modifiable by varying the thickness of insulator layer (here Al_2O_3) as shown in Fig. 3.2(e-g), where we see that leakiness (or, spreading of $\boldsymbol{E}$ field intensity) increases when Al_2O_3 thickness reduces from 100 nm to 10 nm. Plasmonic field generated at the two Au-Al_2O_3 interfaces coupled when the Al_2O_3 layer thickness reduces as illustrated in cross-sectional view Fig. 3.2(e-g). Thus, the leaky behaviour of an MIM nanopillar can be manipulated in a controlled fashion by tuning the Al_2O_3 layer thickness. We

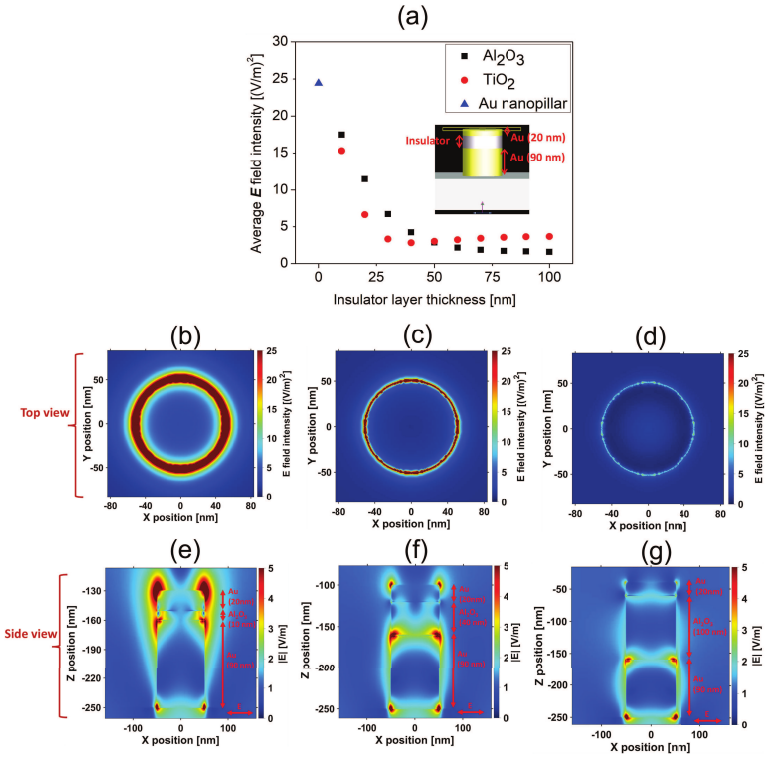

Figure 3.2: (a) Average $\boldsymbol{E}$ field intensity recorded on single Au-insulator-Au nanopillar with varying insulator layer's (Al_2O_3 and TiO_2) thickness has been shown. Average $\boldsymbol{E}$ field intensity on single Au nanopillar (150 nm height and 100 nm diameter) also recorded to compare with the MIM nanopillar. Unpolarized TFSF source with $\lambda = 532$ nm incident from the bottom of nanopillar placed on substrate and $\boldsymbol{E}$ field intensity recorded by a 2D monitor at the top as shown in the inset. Top view (b-d): Electric field (unpolarized TFSF source $\lambda = 532$ nm) intensity $|\boldsymbol{E}|^2$ is recorded by a 2D monitor on top of a nanopillar keeping the Au metal layer's thicknesses constant (20 nm top Au layer and 90 nm bottom Au layer) and varying the insulator layer's thickness (b) 10 nm Al_2O_3, (c) 40 nm Al_2O_3 and (d) 100 nm Al_2O_3. Side-view: figures (e), (f) and (g) depict the $\boldsymbol{E}$ field ($|\boldsymbol{E}|$) distribution with Al_2O_3 layer thickness varying 10 nm, 40 nm and 100 nm, respectively. Incident light's $\boldsymbol{E}$ field polarization is shown in figures.

choose 40 nm thick Al_2O_3 layer and the $\boldsymbol{E}$ field intensity on the top surface are closely identical with the 10 nm Al_2O_3 layer, but the leaked out field spreading is more in MIM nanopillar with 10 nm Al_2O_3 layer (see Fig. 3.2(b) and (c) for comparison). After deciding on the constituent materials with desired thicknesses for the MIM nanostructure, we have then explored five different geometry shapes of single MIM nanopillar to understand the connection between the geometry and optical field leak (see Fig. 3.3(a-e)).

It is visible that, the $\boldsymbol{E}$ field intensity distribution is uniform along the circumference of the circular geometry of the nanopillar (see Fig. 3.3(a)), whereas it is localized only at certain locations for other geometrical shapes (e.g., at corner locations in square, triangle and, hexagon) (see Fig. 3.3(b-e)). Interestingly, plasmonic near-field intensity is uniformly distributed when the rate of change of radius of curvature of a geometrical shape is uniform along its periphery boundary; otherwise, it is localized only at certain regions of the periphery boundary where, radius of curvature changes abruptly. Hence, we decide to choose cylinder-shaped MIM nanopillar structure as the fundamental building block of the proposed nanophotonic sensing device. Single MIM nanopillar's shape optimization was carried out by considering the following dimensions: circular nanopillar of 100 nm diameter, elliptical nanopillar of 100 nm major axis and 50 nm minor axis, hexagonal nanopillar of 100 nm diameter of circumscribed circle of hexagon, square nanopillar of 100 nm side length, and triangular nanopillar of 100 nm each side of equilateral triangle. The effect of the size of nanopillar on the plasmonic field localization for the cylindrical shape was then studied by choosing three different diameters and comparing average $\boldsymbol{E}$ field on the top surface (see Fig. 3.3(f-h)). We observe that the enhancement of average $\boldsymbol{E}$ field intensity around the circumference of the shape is much stronger for 100 nm-sized nanopillar (average $\boldsymbol{E}$ field intensity onto nanopillars with diameter 100 nm - 4.5314 $(V/m)^2$, 500 nm - 0.5681 $(V/m)^2$ and 1 μm - 0.4872 $(V/m)^2$) compared to the larger diameter nanopillars. Hence, we propose to design nanophotonic sensor consisting of

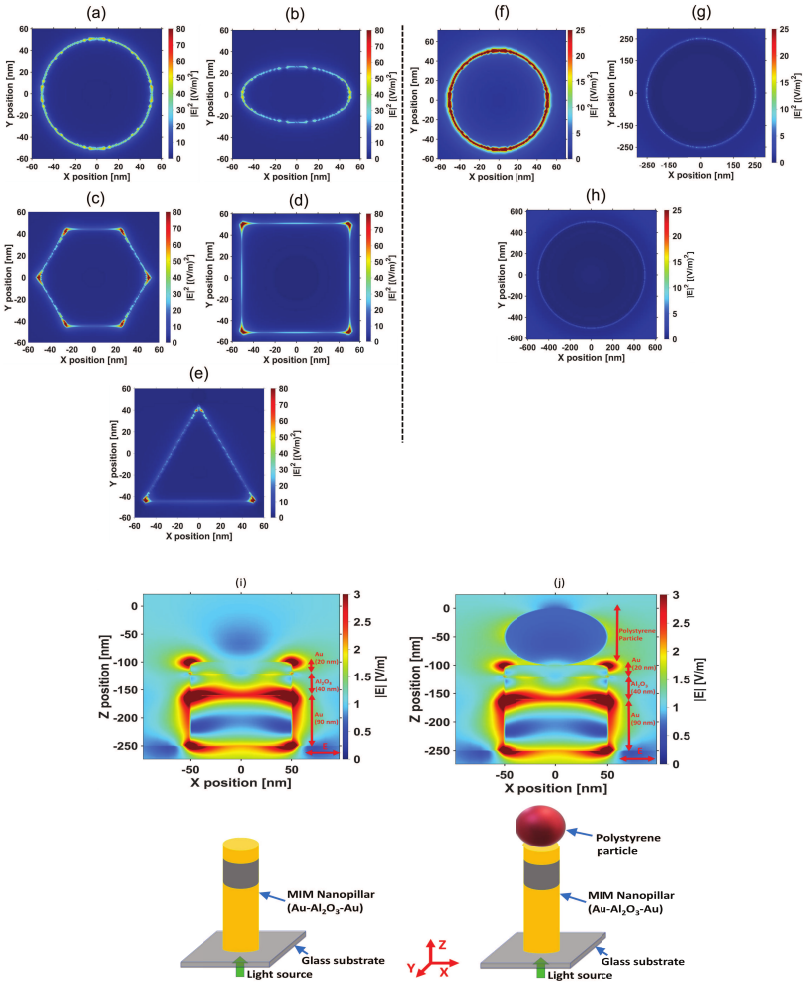

Figure 3.3: $\boldsymbol{E}$ field intensity $|\boldsymbol{E}|^2$ of individual MIM nanopillar as a function of five different shapes- (a) cylindrical (100 nm diameter), (b) elliptical (100 nm major axis and 50 nm minor axis), (c) hexagonal (100 nm diameter of circumscribed circle of hexagon), (d) square (each side length of 100 nm) and (e) triangular (100 nm each side of equilateral triangle). Here, we have considered MIM configuration: 20 nm Au (top layer) – 40 nm Al_2O_3 (middle insulator layer) – 90 nm Au (bottom layer) for all the shapes. Figures (f), (g) and (h) illustrate the intensity distribution for a cylinder-shaped single MIM nanopillar of 100 nm (average intensity- 4.5314 $(V/m)^2$), 500 nm (average intensity- 0.5681 $(V/m)^2$) and 1 μm (average intensity- 0.4872 $(V/m)^2$) diameters, respectively. For these studies, an unpolarized TFSF source at $\lambda = 532$ nm was incident at the bottom of the glass substrate with individual nanopillar on it. Working of nanophotonic sensor: Electric field $\boldsymbol{E}$ distribution of single MIM nanopillar (20 nm Au - 40 nm Al_2O_3 - 90 nm Au) cross-sectional side-view without the presence of a particle shown in (i) and disturbance of $|\boldsymbol{E}|$ field due to the scattering by the 100 nm particle (material: polystyrene) shown in (j). In this case, incident TFSF source along $+Z$ axis direction is TM polarized as shown in schematic figures (i) and (j). The schematic pictures (at the bottom of each electric field distribution figure) display the configurations corresponding to the electric field distributions collected by the cross-section XZ monitors.

a two-dimension (2D) array of 100 nm-diameter cylinder-shaped MIM nanopillars. To understand the working principle of the proposed nanophotonic sensor, the interaction of the plasmonic field of a single MIM nanopillar with a spherical polystyrene particle (R.I $\sim$ 1.59 at λ = 535 nm [118]), 100 nm bead is placed on the top surface of single MIM nanopillar as illustrated in Fig. 3.3(i) and (j) (schematic view also displayed without and with the polystyrene particle on MIM nanopillar configuration). Here, we have introduced a particle of polystyrene [118] as its refractive index matches well with most of the bioanalytes. Also, polystyrene beads were widely used as the representative of bioanalytes for testing several biosensing platforms in the previous reports [92, 95, 119]. When the particle is present on the nanopillar's top surface, the plasmonic near-field of the nanopillar gets scattered by it. This event can be observed from the cross-sectional views (XZ view) of $\boldsymbol{E}$ field distribution of the nanopillar without the particle and with the particle on its top surface Fig. 3.3(i) and (j), respectively (incident light is TM polarized for both cases). Detection of a foreign particle can be confirmed by calculating the relative change in average near-field (electric field) intensity due to the presence of the single particle on the nanopillar's top surface as follows:

$$I_r = \frac{mean(< |E_w|^2 >)}{mean(< |E_{wo}|^2 >)} \tag{3.1}$$

Here, $< |E_w|^2 >$ and $< |E_{wo}|^2 >$ are the averaged $\boldsymbol{E}$ field intensity values with and without the presence of the particle, respectively.

3.4 Simulation method

The design optimization study (studying near-field intensity) was carried out by λ = 532 nm excitation from a TFSF source applied at the bottom of structure placed on glass substrate. Here, we have used perfectly matched layer (PML) boundary condition on all the X, Y and Z directions. The resonance study with the MIM

nanopillar array was carried out with the periodic boundary condition in X and Y directions and PML on Z axis direction with broadband plane wave source excitation. For the randomly oriented particles resonance shift simulation study, we have considered PML boundary condition along all the three coordinate (X, Y and Z) directions. Resonance study with randomly oriented particles were conducted with 5 nm (auto-nonuniform) FDTD mesh size and the second resonance peak position (λ_{r2}) found at 681.77 nm, whereas the same device structure was simulated with 1 nm mesh size and resonance peak found at $\lambda_{r2} = 692.83$ nm. This is the consequence of commonly known FDTD numerical dispersion [120, 121] problem.

3.5 Sensing results and discussion

For biosensing applications, a large active area sensor is preferred, hence, we have designed a 2D array of the cylindrical MIM nanopillars. Two different lattice arrangements- square and hexagonal with active sensing area of 2.56 μm^2 and 1.87 μm^2, respectively were explored in this study considering 150 nm periodicity (center to center distance between two neighbouring nanopillars). Three concentric distinct zones are identified for each design of the device (red dotted line marked zones in Fig. 3.4(a) and (b)) to study whether they have uniform sensing capability throughout the device surface. Numerical simulations were performed by placing single spherical polystyrene particle of diameters- 50 nm, 100 nm and 1 μm on three distinct locations (considering at the top of nanopillar, edge of nanopillar and gap between two adjacent nanopillars) in each zone separately and the values of the relative intensity change (I_r) were calculated for each case. Figures 3.4(c) and (d) show that relative intensity change of a particular particle size is uniform across the surface of a zone. This result confirms that the particle detection sensitivity is homogeneous throughout the MIM nanopillar array device surface, which definitely allows delivery of target analyte anywhere on the device surface and the sensitivity is not dependent on the placements of particles. We examined the effect on relative intensity change when multiple particles of same

size are randomly distributed (here Gaussian distribution considered) over the device surface. The results indicate that, I_r gradually enhances with increase in the number of particles on the device's active sensing area as depicted in figures 3.4(e) and (f) for square and hexagonal array devices, respectively.

It is visible that the ratio of I_r for 100 nm to 50 nm sized particles increases with increase in the number of particles. This simulation result signifies the importance of relative intensity change (I_r) parameter in sub-100 nm sized bioanalytes detection and establishes our optimized MIM nanopillars array design for biosensing applications.

The resonance characteristics were further investigated the surface sensing capability of the proposed sqaure MIM nanopillar array (MIM nanopillar configuration: 20 nm Au – 40 nm Al_2O_3 – 90 nm Au and each nanopillar's diameter of 100 nm and 150 nm periodicity). Resonance wavelength of the MIM nanopillar array device is defined by the dip (transmission intensity minima) locations in its transmission spectrum, when the device is illuminated by a TM polarized broadband planewave source (λ = 400 nm to 2000 nm) (the black curve in Fig. 3.5(a)). Here we found two distinct resonance dip positions at $\lambda_{r1} = 551.5$ nm and $\lambda_{r2} = 692.8$ nm. Fig. 3.5(a) shows the transmission spectra recorded with varying dielectric slab medium refractive index. A linear red-shift is observed at $\lambda_{r2} = 692.8$ nm, when a dielectric slab is placed on the top surface of MIM nanopillar array and with varying the refractive index of slab ranging $n = 1$ to 1.8 (see figures 3.5(a) and (b)). The first resonance position at λ_{r1} = 551.5 nm is due to the gold surface plasmon resonance behaviour (as depicted in Fig. 3.5(c) and (d)) and the second resonance position at $\lambda_{r2} = 692.8$ nm reflects the gap surface plasmon (GSP) mode signature [122] (depicted in Fig. 3.5(e) and (f)). The origin of λ_{r2} is the near-field coupling and interference effects of out-of-phase $\boldsymbol{E}$ fields generated at the two Au-Al_2O_3 interfaces of an MIM nanopillar as illustrated in the cross-sectional side view in Fig. 3.5(f). This GSP mode profile matches well with the previously reported MIM structures [122]. Figures 3.5(g) and (h) are the enlarged view of the two resonance dip locations observed in Fig. 3.5(a) curves. From Fig.

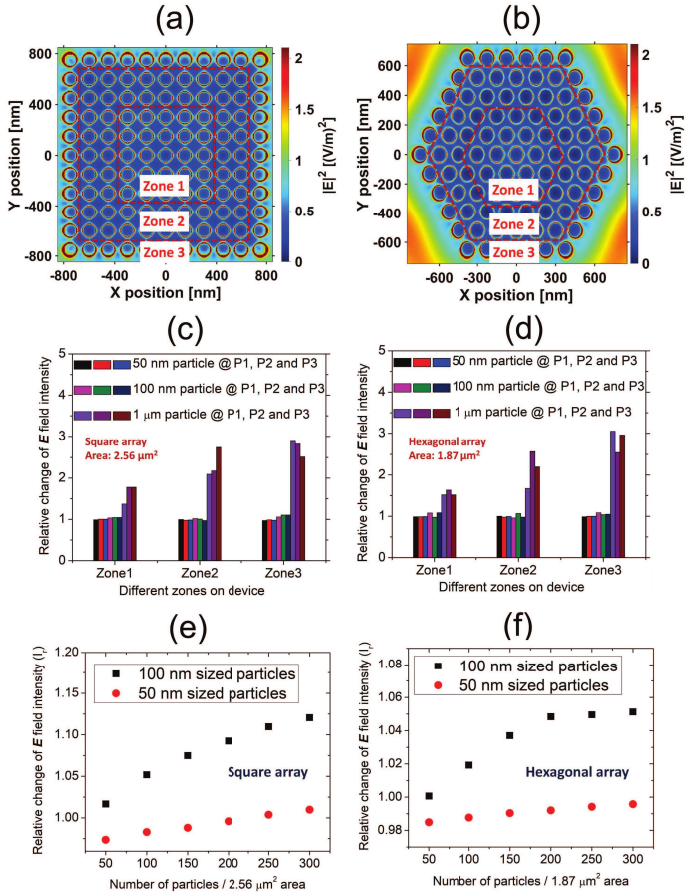

Figure 3.4: Distribution of $\boldsymbol{E}$ field intensity $|\boldsymbol{E}|^2$ recorded by a 2D monitor on the top surface of MIM nanopillar arrays arranged in (a) square and (b) hexagonal form. Here we have considered each cylindrical MIM nanopillar of diameter 100 nm with 20 nm Au (top layer) – 40 nm Al_2O_3 (insulator layer) – 90 nm Au (bottom layer) with periodicity of 150 nm, to show the plasmonic $\boldsymbol{E}$ field coupling on the device surface. Comparison of different dimension particles (50 nm, 100 nm & 1 μm) detection on three different concentric zones of device surface are shown in (c) for square array and (d) hexagonal array devices. Relative change of $\boldsymbol{E}$ field intensity (I_r) calculated and plotted in figures (c) and (d). Here, P1, P2 and P3 represent three different positions of polystyrene particle in each zone, including top of a nanopillar, edge of a nanopillar and gap between two adjacent nanopillars. I_r as a function of number and size of particles on device's active sensing area for, (e) square-shaped array (with active sensing area 2.56 μm^2) device and (f) hexagonal-shaped array (with active sensing area 1.87 μm^2) device. Here, a TFSF source at $\lambda = 532$ nm was incident at the bottom of MIM nanopillars array on glass substrate (light source is unpolarized).

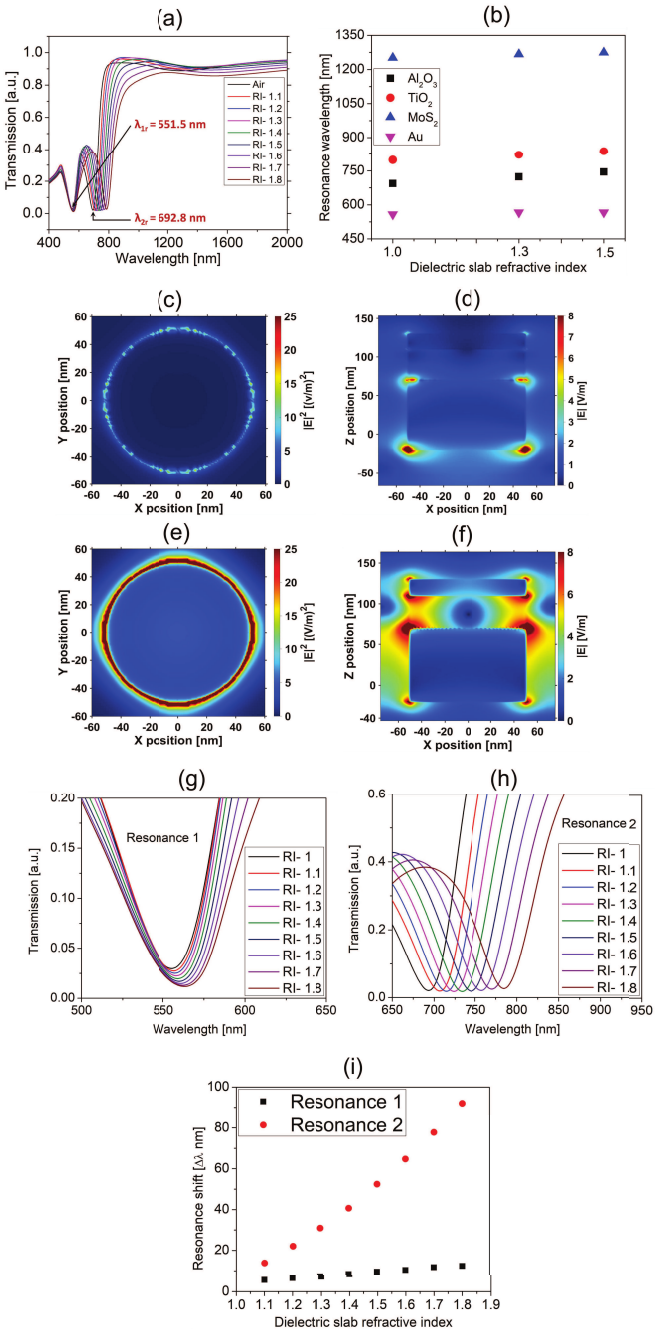

Figure 3.5: (a) Transmission spectra for the MIM nanopillar array (square array) device with 100 nm thick dielectric slab is placed on device surface and refractive index varied from $n = 1$ to 1.8. Figure (b) shows the resonance wavelength (λ_{r2}) shifts with refractive index of dielectric slab. MIM nanopillar's insulator material varies (Al_2O_3, TiO_2 and MoS_2) keeping the thickness fixed (40 nm). Top and cross-sectional side view of single MIM nanopillar (20 nm Au – 40 nm Al_2O_3 – 90 nm Au): (c) and (d) display the top view ($|\boldsymbol{E}|^2$ distribution) and side view ($|\boldsymbol{E}|$ distribution) at $\lambda_{r1} = 551.5$ nm. (e) and (f) show top view ($|\boldsymbol{E}|^2$ distribution) and side view ($|\boldsymbol{E}|$ distribution) at $\lambda_{r2} = 692.8$ nm. For $|\boldsymbol{E}|$ TM polarized and $|\boldsymbol{E}|^2$ figures unpolarized plane wave source was used. (g) and (h) are the enlarged view of λ_{r1} and λ_{r2} locations, respectively. (i) shows the resonance shift of both the resonance positions with slab refractive index increases.

3.5(g), it is clearly observed that, there is resonance shift at the resonance 1 location (λ_{r1} = 551.5 nm) along with the intensity change. However, the resonance 2 (λ_{r2} = 692.8 nm) location shows (see Fig. 3.5(h)) stronger shifts because, the surface plasmon field generated at the top and bottom Au layers coupled inside the Al_2O_3 layer, and the cavity enhanced field is leaked out and localized over the top and the sidewall surfaces. With a small change of nanopillar's surface refractive index, resonance field at λ_{r2} interacts with the dielectric slab medium present on the device surface, and thereby induces a stronger resonance shift. The resonance shift with respect to the slab refractive index changes for both the resonance positions are shown in Fig. 3.5(i), highlights the significance of the leaky plasmonic MIM nanopillar array for biosensing applications. We have investigated the effect of insulator layer's refractive index on the device sensitivity S_λ, keeping the insulator layer's thickness fixed at 40 nm and varying materials used: Al_2O_3 (n = 1.77), TiO_2 (n = 2.67) and MoS_2 ($n > 4$) [123] as they have distinct refractive indices (n) with low absorption at visible wavelength range. The sensitivity of the device is defined as the ratio of the shift in resonance wavelength position to the device surface refractive index change $S_\lambda = \Delta\lambda_r/\Delta n$ nm RIU^{-1} (RIU denotes refractive index unit). A notable finding is that, surface sensitivity of the device reduces with increase in the refractive index of the insulator layer as can be seen from the plot in Fig. 3.5(b). The MIM nanopillar array with Al_2O_3 as the insulator layer material has demonstrated the best surface sensitivity (S_λ = 101.68 nm RIU^{-1}) among the three materials (as illustrated in Table 3.1). The reason for this may be that the leakiness of each MIM nanopillar reduces with the increase of the refractive index of the insulator layer. This is due to the higher confinement inside the insulator layer itself. Thus, available resonant plasmonic field is weak on the top and sidewall surface, thereby reducing the surface sensitivity. We have also compared the surface sensitivity of MIM nanopillar array with Au nanopillar array (see Table 3.1), keeping individual Au nanopillar's height at 150 nm, diameter at 100 nm and periodicity at 150 nm, same as the individual MIM nanopillar's dimensions.

Noticeably, S_λ and Figure-of-Merit (FOM=S_λ/full width at half maximum (FWHM) RIU^{-1}) are significantly higher (see Table 3.1) for the MIM nanopillar array device compared to the Au nanopillar array device. The best FOM obtained 3.72 RIU^{-1} with the Au-Al_2O_3-Au nanopillar array device, which signifies that Al_2O_3 as the insulator layer provides best surface sensitivity by controlling the leaky behaviour of individual MIM nanopillar. Also, the resonance linewidth FWHM = 27.3 nm (at λ_{r2} = 692.8 nm) obtained with Au-Al_2O_3-Au nanopillar array configuration is better than the reported values from literature (see Table 3.1 for comparison of different configurations).

Table 3.1: Comparison of sensor performance metrices for Au nanopillar array and MIM nanopillar array-based devices with different insulator layer materials

Device		Different types of devices			Existing
Parameters	Au	Au-Al_2O_3-Au	Au-TiO_2-Au	Au-MoS_2-Au	Literature
Resonance wavelength (nm)	537.22	692.83	798.34	1251.25	728 (Au nanorods ensemble)[124]
					1020 (Au nanodisks array)[125]
					730 (MIM nano resonators)[126]
					635 (Au mushroom array)[102]
FWHM (nm)	345.97	**27.30**	30.81	88.84	107 (Au nanorods ensemble)[124]
					70 (Au nanodisks array)[125]
					40 (MIM nano resonators)[126]
					10 (Au mushroom array)[102]
Q-factor	1.55	25.37	25.91	14.08	Not reported
Sensitivity (S_λ)	17.97	**101.68**	80	46.79	224 (Au nanorods ensemble)[124]
(nm RIU^{-1})					55 (MIM nano resonators)[126]
					1010 (Au mushroom array)[102]
Figure of Merit (S_λ/FWHM)	0.05	**3.72**	2.59	0.52	2.1 (Au nanorods ensemble)[124]
(RIU^{-1})					3.5 (Au nanodisks array)[125]
					108 (Au mushroom array)[102]

The proposed design of the MIM nanopillars array has few advantages: (i) although we have simulated MIM nanopillar array considering only active sensing area of 2.56 μm^2 (square array) and 1.87 μm^2 (hexagonal array), but the design is scalable to larger area during fabrication, (ii) each nanopillar has larger surface area compared to the nanohole structures. Thus, the exposure of resonant plasmonic field is greater with the bioanalytes attached on the top and sidewall surfaces of MIM

nanopillars, (iii) MIM nanopillar array design demonstrates the tunability of leaky plasmonic field distribution surrounding the nanopillar surface with the change of insulator layer material and thickness, while keeping two Au layers fixed, (iv) narrower resonance linewidth (FWHM = 27.3 nm with 40 nm Al_2O_3 as the insulator layer of each MIM nanopillar in the array) compared to the reported resonance linewidth of Au nanodisk array (FWHM = 70 nm) based biosensing platform [120]. Comparison of sensing performance parameters of our proposed device configurations with the existing literature is shown in Table 3.1. We can observe that the proposed MIM (Au-Al_2O_3-Au) nanopillar array device has narrower FWHM = 27.3 nm and higher FOM = 3.2 RIU^{-1} as compared to the existing devices. The narrower FWHM allows us to observe smaller shift in the resonance wavelength corresponding small size and low concentration of target bioanalytes.

Simulations were conducted to examine the device resonance condition and sensitivity by varying the number of polystyrene particles (size of 100 nm and 50 nm diameter separately) distributed over the MIM (Au-Al_2O_3-Au) nanopillar array (square shape with periodicity 150 nm and diameter of each pillar 100 nm). Figures 3.6(a) and (b) show the resonance peak positions against number of particles on the device surface for 100 nm and 50 nm sized particles, respectively. Each of the semi-log plots are fitted with exponential curves as shown in figures 3.6(a) and (b). The slope of the curve defines the sensitivity as defined by the following formula:

$$S = \frac{\Delta\lambda}{\Delta P} \tag{3.2}$$

where, $\Delta\lambda$ represents the resonance wavelength shifts and ΔP represents the increment of the number of polystyrene particles present on the device surface. This is presented as the semi-log plot in Fig. 3.6 and the sensitivity (S) is in nm/decade unit.

The slopes of each curve were calculated by two linear fits choosing the X-range (number of particles) as shown. For 100 nm sized particles (Fig. 3.6(a)), the slopes

are 2.17 nm/decade and 17.66 nm/decade corresponding to the number of particles ranging from 1-100 and 200-1000 (X-axis range), respectively. Similarly, for 50 nm sized particles slopes are 0.096 nm/decade and 6.41 nm/decade corresponding to the particles 1-10 and 100-1000 (X-axis range), respectively (see Fig. 3.6(b)). This portrays the highest detection sensitivity was achieved 17.66 nm/decade for 100 nm sized polystyrene particles. It is also evident from the resonance shift plots in Fig. 3.6(c) and (d) that, 100 nm diameter polystyrene particles induced larger resonance shift compared to the 50 nm sized particles, indicating stronger interaction of localized plasmonic field with the 100 nm sized polystyrene particles. Another noteworthy fact that, resonance shifts of 1.45 nm and 0.27 nm were obtained due to the presence of single polystyrene particle of 100 nm and 50 nm diameters, respectively. These resonance shift values can be measured experimentally by using a high resolution spectrometer (Horiba 1250M research spectrometer with resolution = 0.006 nm). This affirms that our proposed MIM nanopillar array-based platform can be used for 100 nm and smaller size virus particles detection with remarkably lowest detection limit (LOD = 1 particle). Additionally, we have performed simulations by mixing equal number of 50 nm and 100 nm sized polystyrene particles distributed over the MIM nanopillar array surface. The calculated sensitivity is shown in Fig. 3.6(e)) and resonance shift is presented in Fig. 3.6(f)). Here, we found that, sensitivity is lesser compared to only one type of particles present on the device surface. The reason could be the overlap among different dimension particles reduces the plasmonic field interaction with the particles on the MIM nanopillar array surface. With more detailed study of the mixture of different sized particles, one may be able to obtain the correlation between the particle size concentration with the wavelength shift.

There is another recently published work [127] where a hybrid metasurface was proposed for biosensing application. They have used Si hollow square nanostructure array on Au thin film, where the field is majorly confined within the Si nanostructure. However, in our proposed leaky MIM nanopillar array based sensing platform,

the resonant plasmonic field is accessible to the top and sidewall surface of individual nanopillar. Also, the 50 nm gap between two adjacent nanopillars allows to couple the resonant field and strong enhancement at the top surface and at the gap between two adjacent nanopillars. Target analytes located anywhere on the proposed MIM nanopillars array device can be detected with detection limit of 1 polystyrene particle.

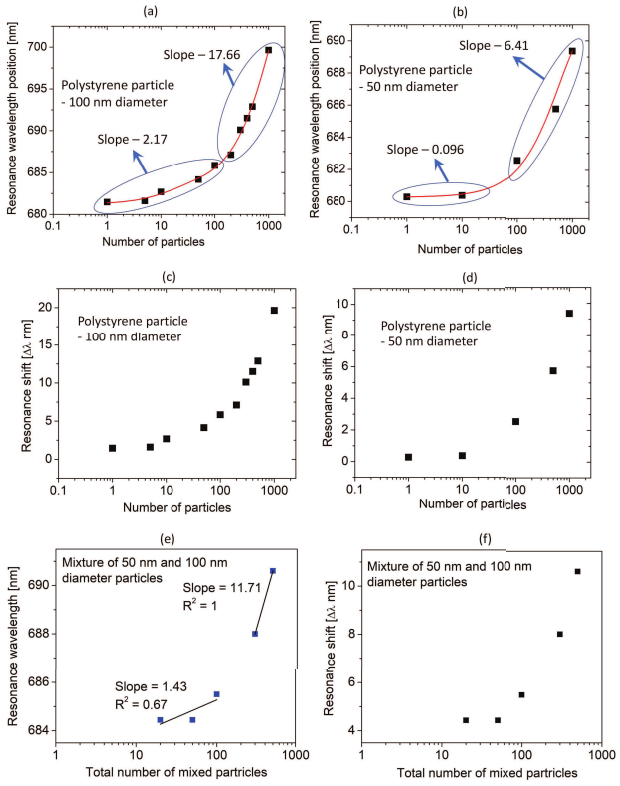

Figure 3.6: Resonance position with respect to the number of polystyrene particles on the device sensing surface for both (a) 100 nm and (b) 50 nm sized particles. Resonance shifts with the presence of polystyrene particles are shown for (c) 100 nm and (d) 50 nm sized particles, respectively. Figures (e) and (f) show the resonance wavelength shifts with the total number of particles (equal number of mixed 50 nm and 100 nm sized particles are present) on the MIM nanopillar array surface. Here, MIM (Au-Al_2O_3-Au) nanopillars square array device was used, where each pillar diameter is 100 nm with a periodicity of 150 nm. An array of 11 x 11 MIM nanopillars, where PML boundary condition along the Z boundary (light incident from the $+Z$ axis direction) and periodic boundary condition along the X and Y boundaries were used. A plane wave source (TM polarized) was used to excite the device.

3.5.1 Proposed Nanofabrication Process

The designed MIM nanopillar array can be fabricated on glass/quartz substrate using the following process:

- Electron beam lithography (EBL) to fabricate the circular nanostructure patterns on the glass substrate using ZEP 520A EBL resist.
- Standard material deposition techniques such as, e-beam evaporation and sputtering can be used for Au and Al_2O_3 layer deposition [104], respectively.
- The lift-off of Au and Al_2O_3 layers can be performed by soaking into the Remover PG solution.
- Another method that can be used is that after EBL patterning and metallization, insulator layer deposition, oxygen plasma etching technique can be performed to etch the metal and oxide layers and obtain the MIM nanopillar array structures as discussed in [128].

For experimental measurements, near-field intensity measurement can be conducted using near-field scanning optical microscope (NSOM) [129]. Standard optical transmission measurement can be performed to obtain the shift in the second resonance peak (λ_{r2}) after surface functionalization and attachment of bioanalytes on the surface of the MIM nanopillar array device. Extensive experiments need to be carried out to establish its prospect as a size-selective sub-100 nm bioanalytes detection platform. A high resolution (0.006 nm) [130] commercially available spectrometer like Horiba 1250M research spectrometer can be utilized for the experimental set up to detect the small shift in resonance wavelength predicted in simulation. To achieve the detection of a specific bioanalyte, device surface needs to be bio-functionalized accordingly.

3.6 Conclusion

In summary, we have optimized structural parameters of MIM nanopillar array for single sub-100 nm particle detection. Simulation results demonstrate that the MIM nanopillar array with 100 nm diameter and 150 nm periodicity is a promising platform for 100 nm and smaller size polystyrene particles detection. In our simulation, polystyrene particles were used to represent different virus of the same respective size and shape (for example, 100 nm sized virus: SARS-CoV-2, influenza H1N1 and 50 nm sized virus: hepatitis B), as most of the bioanalytes have refractive indices similar to the polystyrene. Our proposed platform demonstrated a homogeneous sensing capability over the device surface area of 2.56 μm^2 (square array) and 1.87 μm^2 area (hexagonal array) which was chosen due to simulation constraints, but this design is scalable to achieve larger active sensing area with the standard fabrication techniques. Our study shows that square array of MIM nanopillars illustrated two distinct resonance peaks and specifically, the second resonance peak (at $\lambda_{r2} = 692.8$ nm) is very sensitive with the device surface's local refractive index change and therefore, induces a shift in resonance wavelength. Simulation study with different insulator materials (of distinct refractive indices) shows the importance of insulator layer in tuning the optical field leak in MIM nanopillar to attain detection sensitivity and FOM. We found the best surface sensitivity $S_\lambda = 101.68$ nm RIU^{-1} and FOM = 3.72 using the dielectric slab on device surface and gained the detection sensitivity of 17.66 nm/decade and 6.41 nm/decade for 100 nm and 50 nm sized polystyrene particles, respectively. The lowest possible theoretical LOD = 1 particle was achieved for both the 100 nm and 50 nm sized polystyrene particles for corresponding resonance shifts of 1.45 nm and 0.27 nm in presence of 1 polystyrene particle, respectively. Noticeably, the resonance peak line width (FWHM at λ_{r2}) is 27.3 nm of Au-Al_2O_3-Au nanopillar square array device, which is better than many existing plasmonic biosensing platforms. In future, our proposed MIM nanopillars array platform can be fabricated and

integrated to a portable set up consisting of a visible wavelength range light emitting diode (LED) and a portable high resolution spectrometer. For specific bioanalytes detection, Au surface of MIM nanopillars could be biofunctionalized accordingly.

Chapter 4

Experimental Validation of Plasmonic Metal-Insulator-Metal (MIM) Nanoresonator Configurations

In Chapter 3, we discussed how the geometry of MIM nanoresonators impacts detecting small size polystyrene particles. We have performed optical transmission simulation using Ansys-Lumerical FDTD [108] to optimize the design parameters of MIM nanopillar resonators. To achieve higher biosensing performance, plasmonic devices need to have a larger spectral shift per refractive index unit (RIU) change. In this context, a metal-insulator (MI) nanostructure elevates the plasmonic metal layer by a dielectric layer on the substrate [131, 132] or, a metal-insulator-metal (MIM) structure [69, 133] introduce a great degree of tunability to manipulate the resonance optical field. Plasmonic metal-insulator-metal (MIM) nanoresonator cavities have attracted special attention for their ability to confine light to nanoscale dimensions by resonance excitation. The plasmonic field at the metal-insulator interface tends to concentrate in the insulator layer instead decaying into the surrounding air medium [134–137]. Thus, choosing an insulator material and the resonator dimensions is crucial to balance the field leak and confinement.

Several works of different types of MIM nanostructures are reported, such as split ring resonator-bar structures [134], lifted cross-bar structures [135], closely packed

nano disk clusters [136] and silver nanocubes supported on dielectric substrates [137]. Few studies demonstrated the detection of disease biomarker proteins with plasmonic MIM device platforms by measuring the relative intensity change when the local refractive index changes on the device surface [104]. MIM nano cup array fabricated on a transparent polymer substrate for the detection of carcinoembryonic antigen (CEA) with a limit of detection of 10 ng/mL. Plasmonic MIM-capped polymer nanopillar array also exhibits detection of protein-protein interactions and the cancer biomarker cancer antigen 125 (CA-125) [105]. Plasmonic Au mushroom (MIM structure) array device [138] was proposed for the detection of two different proteins- cytochrome c (Cyt c) and alpha-fetoprotein (AFP), with LOD as low as, 200 pM and 15 ng/ml, respectively.

In this chapter, we investigate the fabrication of MIM nanoresonators and validate the previous simulation work through experimental measurements. We explore two MIM nanoresonator configurations and optimize the design by performing reflection simulations using FDTD. The reflection mode measurement method was selected due to its suitability for a portable optical setup, as well as for its ability to facilitate device fabrication on SiO_2/Si substrate in contrast to quartz/glass substrate. Structural parameters with FDTD simulations (reflection spectroscopy) were optimized to obtain the best sensitivity for 100 nm polystyrene beads detection.

4.1 Design and Working of MIM Nanoresonator Configurations

In this work, we have proposed two different systems based on MIM nanoresonators: (i) MIM_configuration_1: Au nanoresonators array on stacked Au and insulator thin film layers (see schematic in Fig. 4.1 (a)), and (ii) MIM_configuration_2: metal-insulator-metal nanopillar array (see schematic in Fig. 4.1 (b)), both on the SiO_2/Si substrate. The FDTD simulation package from Ansys-Lumerical Inc. [108] was used to optimize the design parameters of MIM nanoresonators. Here, we have used Au

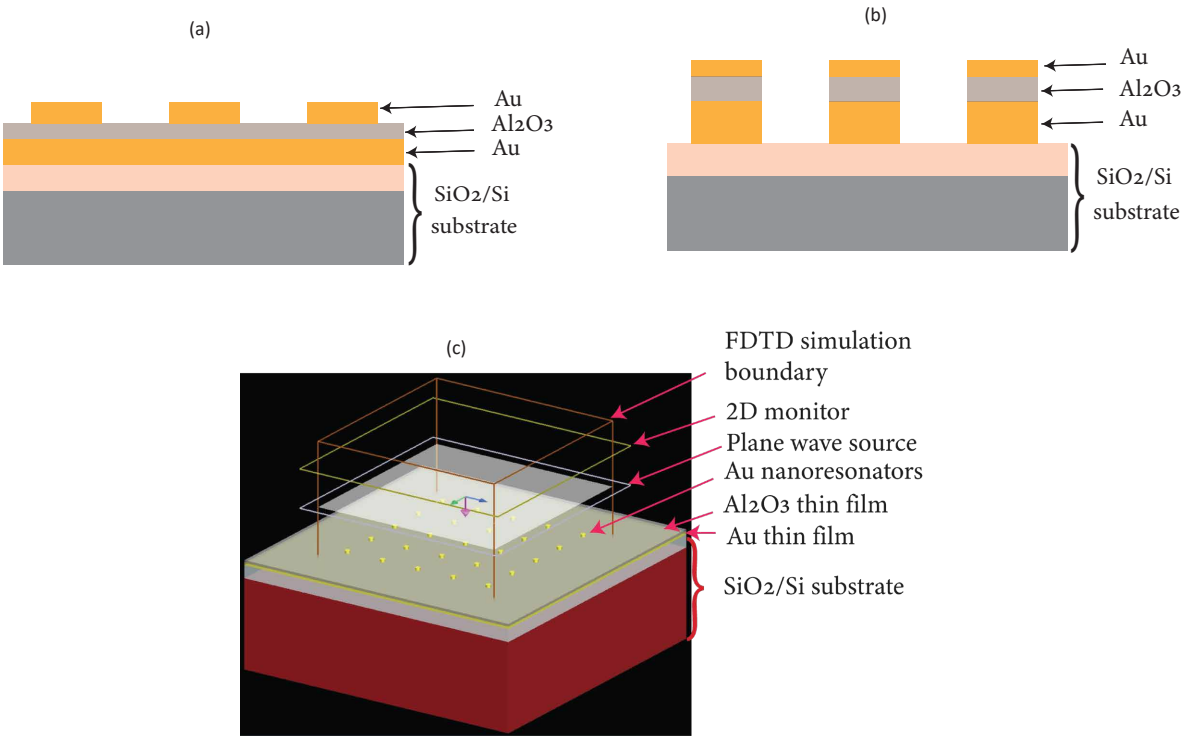

Figure 4.1: Schematic illustration of (a) MIM_configuration_1: Au nanoresonators array on metal-insulator thin film stack. Au as the plasmonic metal and Al_2O_3 as the insulator layer was used on thick Au mirror layer. (b) MIM_configuration_2: Au-Al_2O_3-Au nanopillar resonator array, and (c) Schematic illustration of FDTD simulation setup with the MIM_configuration_1.

as the plasmonic material because of its chemical stability and bio-compatibility. A thicker Au layer (90 nm - 100 nm) is used as the bottom layer for both the MIM nanoresonator configurations, as it acts as a mirror layer so that, the incident light can reflect back to the top surface. A thinner (partially transparent) top Au layer is chosen to leak out the resonance field on the top surface. In the previous Chapter 3, we have demonstrated that Al_2O_3 as the insulator material is good for maintaining the balance between the resonance field leakage and confinement of individual MIM nanopillar resonator. Therefore, throughout this study, we have utilized Al_2O_3 as the insulator layer material for both the nanoresonator configurations and optimized the following parameters: diameter (D) and pitch (P) of Au nanoresonators on insulator-metal thin film, Al_2O_3 layer thickness, varying D and P of MIM nanopillars. We performed simulations with varying numbers of polystyrene particles of 100 nm diameter distributed over the device surface and calculated the sensing performance parameters such as sensitivity, and figures of merit (FOM). Polystyrene particles were chosen to be 100 nm in size because it matches the dimensions of SARS-CoV-2, allowing the utilization of MIM nanoresonator array platform for virus sensing applications. The schematic in Fig. 4.1 (c) illustrates the FDTD simulation setup with MIM nanoresonators, where a broadband plane wave source (λ = 400 - 2000 nm) was used for excitation and the 2D field monitor was placed above the source plane to capture the reflection spectrum. In the simulation study, we have used periodic boundary conditions along the $X - Y$ direction. The perfectly matched layer (PML) boundary condition was used in the Z direction so that no scattered field can interfere with the reflected signal from the device, which is the primary interest for calculating the sensor's performance.

Different types of plasmonic modes are generated depending on the resonator configuration. For MIM_configuration_1, two plasmonic modes are generated, localized surface plasmon resonance (LSPR) modes generated by the excitation of the top Au nanoresonator array and the field is localized surrounding the Au nanoresonators.

Another waveguide mode is created due to the propagation of surface plasmons in the Al_2O_3 layer [139]. The Al_2O_3 thin film acts as the dielectric waveguide layer, and the coupling between the LSPR and waveguide modes generates the plasmon resonance wave, which is more confined inside the Al_2O_3 layer. In case of MIM nanopillar array (MIM_configuration_2), localized surface plasmons are generated on the top and bottom gold layers. Plasmonic modes are generated depending on the thickness and refractive index of the insulator layer. Strong coupling of plasmon fields generated at the two Au-Al_2O_3 interfaces enhances the resonance field at the insulator layer and this plasmonic mode is known as gap surface plasmon (GSP) resonance which is discussed in the background Chapter 2 of thesis. By introducing a leaky MIM nanoresonator configuration, the resonance field spread over the top and sidewall surface of individual MIM nanopillar (MIM_configuration_2). The target bioanalytes attached on the device surface disturb the resonance field, which induces a resonance red-shift.

4.2 Experimental Methods

We have used the FDTD simulation optimized structural parameters to fabricate both the MIM nanoresonator configurations. The detailed fabrication process is illustrated in Fig. 4.2 (a) and (b) for MIM_configuration_1 and MIM_configuration_2, respectively. For both the fabrication processes, 10 mm $\times$ 10 mm SiO_2/Si chips were first piranha cleaned and dried with N_2 gun. The patterns were designed by the Raith design software tool and were exposed by Raith150 Two electron beam lithography (EBL) system. For fabricating the MIM_configuration_1 (see process flow in schematic Fig. 4.2 (a)), piranha-cleaned chips were first used for Au deposition using e-beam evaporation. We have deposited 5 nm Ti/90 nm Au/5 nm Ti with the e-beam evaporation technique. 100 nm Al_2O_3 film was deposited by using the atomic layer deposition (ALD) technique with Kurt J. Lesker 150LX ALD system. We have used trimethylaluminum (TMA) and water used as the precursors and the substrate holder

temperature was 300°C and total 1111 number of cycles were used to deposit 100 nm thick Al_2O_3 film on the Au coated SiO_2/Si substrates. After Al_2O_3 deposition, EBL resist ZEP 520A was coated on it. The spin-coating recipe used for ZEP 520A positive tone EBL resist with spin speed: 5000 rpm, ramping: 2000 rpm/sec, time: 40 sec, and then the chips were post-baked at 180°C for 1 minute. We have optimized the EBL patterning parameters such as, electron-beam aperture: 20 μm, beam voltage (EHT) = 10 kV, and the write field area was 100 μm × μm with 1000× objective to write the patterns. After EBL exposure of the patterns the resist was developed using ZED N50 developer for 15 sec, then immediately in MIBK/IPA (1:3) for 10 sec, then dry with a N_2 gun. After EBL exposure and development of patterns, 20 nm Au with 5 nm Ti adhesive layer was deposited by e-beam evaporation technique. The top Au layer was lift-off using the hot (75° C) remover PG solution for 1.5 hours and the remover PG solution was changed after each 30 minutes interval.

For fabricating the MIM_configuration_2 (see process flow in schematic Fig. 4.2 (b)), the cleaned chips were baked at 180°C for 5 minutes to evaporate any water or, moisture present on the substrate surface. Then the baked chips were used for spin-coating of positive tone EBL resist ZEP 520A using the aforementioned spin coating recipe. The EBL patterning and development recipe was same as used for MIM_configuration_1. Both Au and Al_2O_3 layers were deposited by electron-beam evaporation technique. The materials were deposited in the following order on EBL patterned chips: 5 nm Ti/90 nm Au/5 nm Ti/20 nm Al_2O_3/5 nm Ti/20 nm Au, where Ti was used as the adhesive layer. After depositing all the layers, chips were sunk into hot (75°C) remover PG for lift-off. The lift-off process took 90 minutes and every 30 minutes the old solution was replaced by a new remover PG solution to avoid any re-deposition of lift-off metal flakes. After lift-off, chips were cleaned by IPA solution and dried with N_2. To perform the experimental measurements with the fabricated devices, 9 devices were fabricated on a single chip for both configurations. The gap between two neighboring devices was 1.5 mm to prevent any signal

interference during optical measurements.

The optical quality of the ALD deposited Al_2O_3 layer is confirmed by the ellipsometry technique as shown in Fig. 4.3 (a). We have deposited a 20 nm Al_2O_3 thin film using electron-beam evaporation on a bare silicon chip just after HF/BOE clean and performed ellipsometry to verify the optical quality. The Fig. 4.3 (b) shows the optical constants of Al_2O_3 layer deposited by e-beam evaporation technique.

4.2.1 Polystyrene Beads Sample Preparation

Polystyrene beads of diameter 100 nm and 3 μm were purchased from Sigma-Aldrich and Polysciences Inc., respectively. Concentrated 100 nm sized polystyrene beads solution (original stock solution concentration – 2×10^{14} beads/mL) was diluted in deionized (DI) water to prepare different bead concentration solutions - 100 beads/μL, 300 beads/μL, 400 beads/μL, 500 beads/μL, and 700 beads/μL. Only 0.3 μL of each concentration solution was drop cast on a 100×100 μm^2 device area using a micropipette, and the chip was placed on a hotplate (at 60°C) to evaporate the water and the optical measurement was then performed. After each measurement, the chip was cleaned with chloroform and DI water to remove the polystyrene beads before the next measurement was conducted.

4.3 Results and Discussions

4.3.1 Simulation Results

Here, we present both the simulation and experimental results of the two MIM configurations. We have conducted simulations of the MIM_configuration_1 by varying the diameter, pitch of Au nanoresonators, the thickness of Al_2O_3 layer while keeping the height of Au nanoresoantors 20 nm and bottom Au mirror layer thickness 90 nm. In the simulation spectra of MIM_configuration_1, there are three major resonance positions observed as shown in Fig. 4.4 (a). The enlarged view portrays that all three

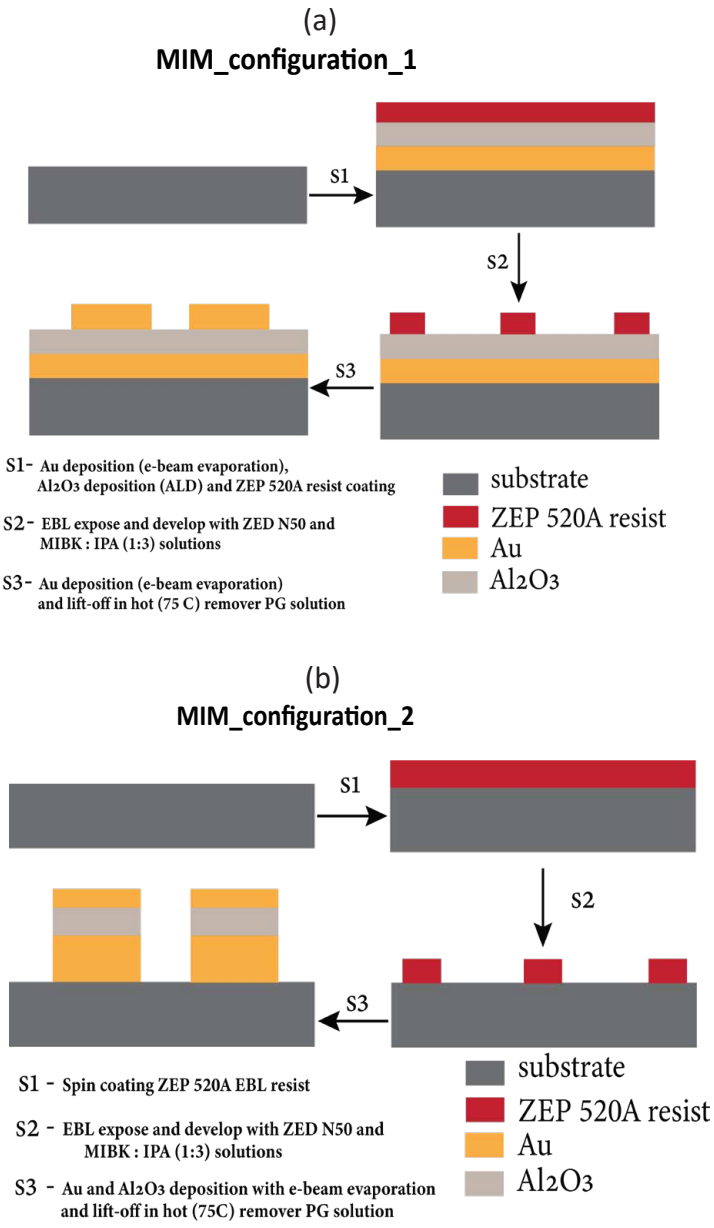

Figure 4.2: The schematic illustration in (a) shows the fabrication process steps for the Au nanoresonators array on Al_2O_3/Au thin film stack (MIM_configuration_1), and in (b) fabrication process flow MIM nanopillars (Au-Al_2O_3-Au) array (MIM_configuration_2) is demonstrated.

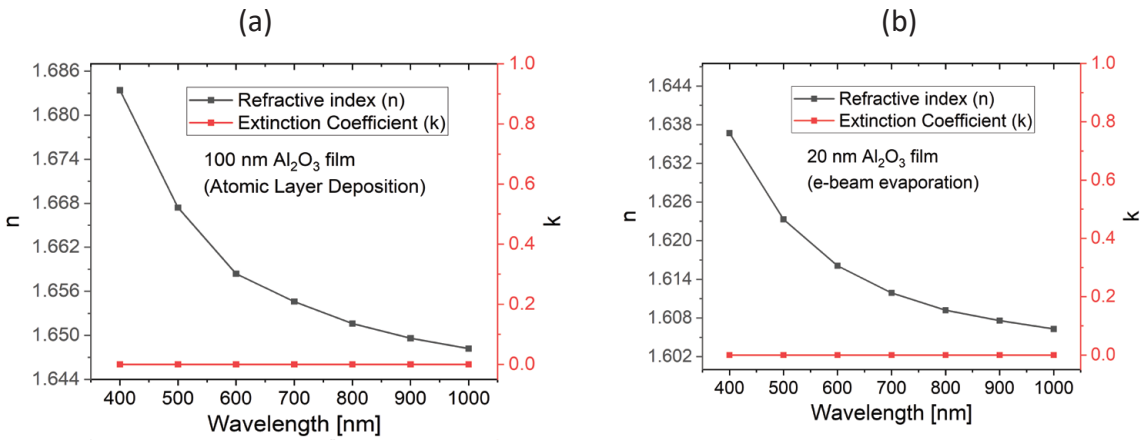

Figure 4.3: Ellipsometry measurement shows optical constants refractive index n and extinction coefficient k for (a) 100 nm Al_2O_3 thin film using atomic layer deposition technique. (b) 20 nm Al_2O_3 thin film deposited using electron beam evaporation technique.

resonance wavelength shifts with the increase in the number of polystyrene particles. Fig. 4.4 (b), (c), and (d) represent the linear response of resonance shift with the number of polystyrene particles at $\lambda = 850.05$ nm, 923.7 nm, and 1087.2 nm, respectively. The slope of the piece-wise linear response curve represents the detection sensitivity. The best detection sensitivity achieved at $\lambda = 850.05$ nm, $\lambda = 923.7$ nm, and $\lambda = 1087.2$ nm are $S = 2.83 \pm 0.12$ nm/decade, $S = 3.23 \pm 0.24$ nm/decade, and $S = 9.58 \pm 1.38$ nm/decade, respectively for the range of 300 to 1000 polystyrene particles. The FWHM at $\lambda = 850.05$ nm, 923.7 nm, and 1087.2 nm are $\delta\lambda = 7.59$ nm, 13.9 nm, and 6.57 nm, respectively. Hence, we obtain the FOM ($S/FWHM$, unit: per number of polystyrene particles in log-scale) are 0.37, 0.23, and 1.45 at the resonance wavelength $\lambda = 850.05$ nm, 923.7 nm, and 1087.2 nm, respectively. Also, the LOD (in simulation) achieved with this MIM device configuration is 10 particles. Out of the three resonance positions available, we have decided to focus on $\lambda = 850.05$ nm for further study. This particular wavelength falls within the Near Infrared (NIR) range and is within the range of our lab spectrometer, the Oceanoptics USB 4000 spectrometer model, which can measure wavelengths up to 900 nm. Our ultimate goal is to develop an affordable and easy-to-use portable biosensor platform that op-

erates in the visible wavelength range.

The E field distribution is depicted in Fig. 4.5 to understand the resonance characteristics and sensing performances. The top view in Fig. 4.5 (a), (b), and (c) display the E field distribution of the MIM nanoresonators array (MIM_configuration_1) recorded by a 2D field monitor placed at the top surface for the resonance wavelength $\lambda = 850.05$ nm, 923.7 nm, and 1087.2 nm, respectively. It is clearly visible that, there are different coupling of the resonance field on the top surface of MIM nanoresonator MIM_configuration_1. The resonance field is localized surrounding the Au nanoresonators for the resonance $\lambda = 850.05$ nm, 923.7 nm (see Fig. 4.5 (a) and (b)), whereas, a plasmonic surface wave present at the resonance $\lambda = 1087.2$ nm. Therefore, the field interaction with the polystyrene particles is stronger and produces a higher detection sensitivity and FOM at $\lambda = 1087.2$ nm as observed in Fig. 4.4 (d). In Table 4.1, we have presented a summary of structural parameters and corresponding detection sensitivity of MIM_configuration_1. It is clearly visible that, 100 nm diameter (D), 800 nm pitch (P) configuration has highest sensitivity of $S = 9.58 \pm 1.38$ nm/decade.

Table 4.1: Summary of sensitivity obtained from different design parameters of MIM nanoresonator array (MIM_configuration_1).

Diameter (D in nm)	Pitch (P in nm)	Al_2O_3 layer thickness (in nm)	Sensitivity (nm/decade)
100	300	100	1.93
100	500	60	7.45
100	500	100	7.06
100	500	200	2.69
100	600	100	6.42
100	800	100	9.58

For MIM_configuration_2, We have performed FDTD simulations by varying the diameter and pitch to make the gap between two adjacent nanopillars is 100 nm. This creates a stronger coupling between two neighboring MIM nanopillar's leaky plasmonic field and thereby achieve a strong interaction with the polystyrene beads

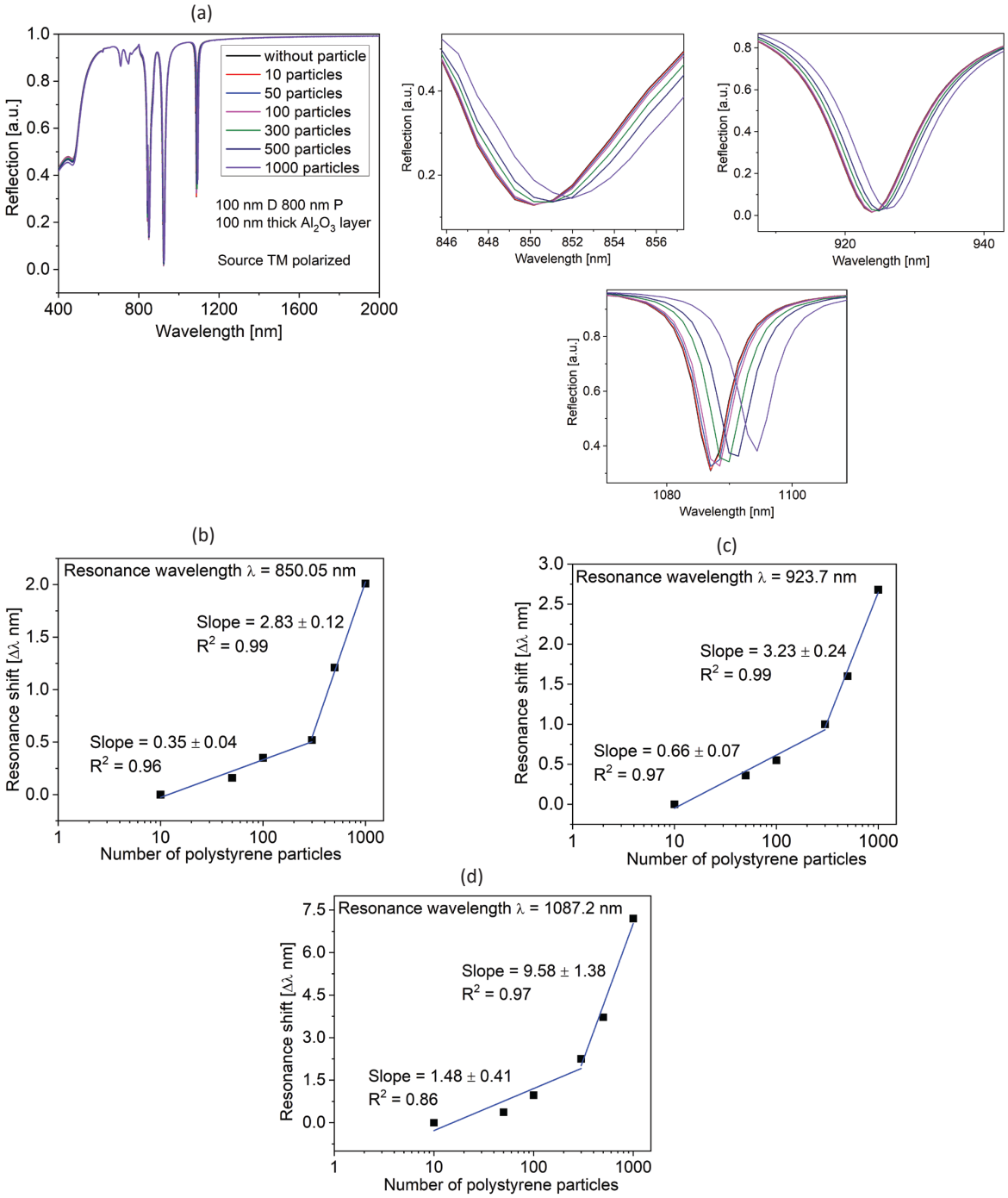

Figure 4.4: (a) Simulated reflection spectra of MIM_configuration_1 (MIM configuration: where 20 nm thick Au nanoresonators (D = 100 nm and P = 800 nm) are on the top of Al_2O_3 (100 nm)/Au (90 nm) thin film stack) show the resonance positions. The zoomed-in view shows three major resonance wavelength positions with the number of polystyrene particles varying from 10 to 1000. In figures (b), (c), and (d) resonance shift response is illustrated with the increase in the number of polystyrene particles at the resonance wavelength λ = 850.05 nm, 923.7 nm, and 1087.2 nm, respectively. In this simulation, TM (p) polarized broadband light source (400-2000 nm) was used.

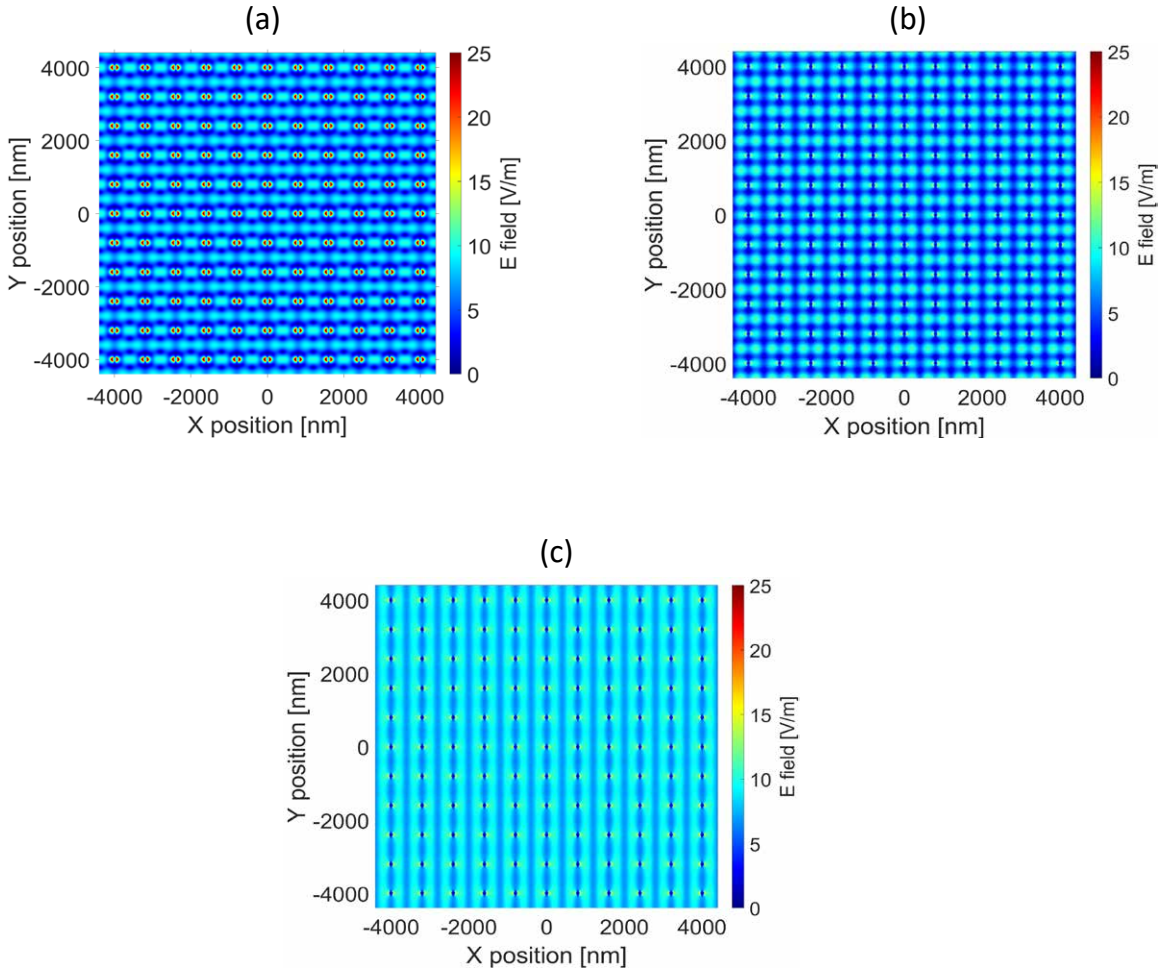

Figure 4.5: The E field distribution recorded on the top surface of MIM nanoresonators array (MIM_configuration_1), where 20 nm thick Au nanoresonators (D = 100 nm and P = 800 nm) are on the top of Al_2O_3 (100 nm)/Au (90 nm) thin film stack at the resonance wavelengths of (a) λ = 850.05 nm, (b) λ = 923.7 nm, and (c) λ = 1087.2 nm, respectively.

of 100 nm diameter placed on the top surface of a nanoresonator or at the gap between two adjacent nanoresonators. The Fig. 4.6 (a) shows the simulated reflection spectra obtained from the MIM nanopillar array where each MIM nanopillar configuration: D = 100 nm, P = 200 nm, thickness of Al_2O_3 layer = 20 nm, top Au layer = 20 nm and bottom Au layer = 90 nm. There are several resonance dip locations and a significant resonance shift was observed in the two resonance positions λ = 726.78 nm and λ = 1175.12 nm (as seen in the enlarged view of resonance positions in Fig. 4.6 (a)). The piece-wise linear response of resonance shift curves can be observed in Fig. 4.6 (b) and (c) for both resonance positions. The detection sensitivity obtained $S = 5.08 \pm 1.01$ nm/decade for the number of particles ranging from 10 to 300 and $S = 33.13 \pm 5.54$ nm/decade for 300 to 1000 particles at the resonance wavelength $\lambda_{resonance}$ = 726.78 nm (see Fig. 4.6 (b)). The resonance line width (FWHM at $\lambda_{resonance}$ = 726.78 nm) $\delta\lambda$ = 94.95 nm obtained from the spectrum without any particles present (black curve in Fig. 4.6 (a)) by Gaussian fit. Hence, we obtain the sensing performance parameter figure of merit (FOM) = 0.05 (per number of polystyrene particles in log-scale) and 0.34 (per number of polystyrene particles in log-scale) for the particles ranges from 10 to 300 and 300 to 1000 particles, respectively. Similarly, at the $\lambda_{resonance}$ = 1175.12 nm, the detection sensitivity of $S = 28.69 \pm 7.59$ nm/decade was achieved for the 10 to 300 particles, and $S = 256.2 \pm 2.01$ nm/decade for 300 to 1000 particles (see Fig. 4.7 (b)). The FWHM (at $\lambda_{resonance}$ = 1175.12 nm) is 333.47 nm, and we obtain FOM 0.08 and 0.76 for the number of particles ranging from 10 to 300 and 300 to 1000, respectively. The MIM nanopillar array (MIM_configuration_2) provides a limit of detection (LOD) of 10 particles in the simulation.

To understand the sensing performance of the MIM nanopillar array (MIM_configuration_2), the E field distribution recorded at the top of the MIM nanopillar array presented in Fig. 4.7 (a) and (b) for $\lambda_{resonance}$ = 726.78 nm and $\lambda_{resonance}$ = 1175.12 nm, respectively. This clearly illustrates that E field localization on the surface of individual MIM nanopillar and near-field coupling makes the whole surface sensitive

for 100 nm size particle detection. From the simulation results, it is observed that resonance field disturbance is smaller by the lower number density of polystyrene particles present on the device surface generating a weaker sensing response. However, the larger number of polystyrene particles (300 to 1000) on the device surface makes a stronger overlap with the localized resonance field on the device surface creating a larger resonance shift and thereby enhance the sensing response.

We also have performed simulations by varying the diameter and pitch of MIM nanopillars keeping all layers' thickness fixed. The detection sensitivity is summarized in Table 4.2 and the best detection sensitivity was obtained for D = 100 nm and P = 200 nm of the MIM nanopillar array (MIM_configuration_2) for both the wavelength ranges as shown in Table 4.2.

Table 4.2: Summary of sensitivity obtained from different design parameters of MIM nanopillar array (MIM_configuration_2).

Diameter (D in nm)	Pitch (P in nm)	Sensitivity (nm/decade) in 400 - 900 nm range	Sensitivity (nm/decade) in 900 - 2000 nm range
100	200	33.13	256.2
100	300	0.25	23.82
100	500	0.87	NA
150	250	5.26	44.03
150	350	2.21	6.87

4.3.2 Experimental Results and Discussions

After obtaining the optimized design parameters from the FDTD simulation study for both configurations of MIM nanoresonators, devices are fabricated and the detailed process flow is shown in Fig. 4.2 (a) and (b) for MIM_configuration_1 and MIM_configuration_2, respectively. The Fig. 4.8 (a) shows the schematic of MIM_configuration_1 and the SEM images of fabricated device with the simulation optimized condition (5 nm Ti/90 nm Au thin film/5 nm Ti/100 nm Al_2O_3 thin film/Au nanores-

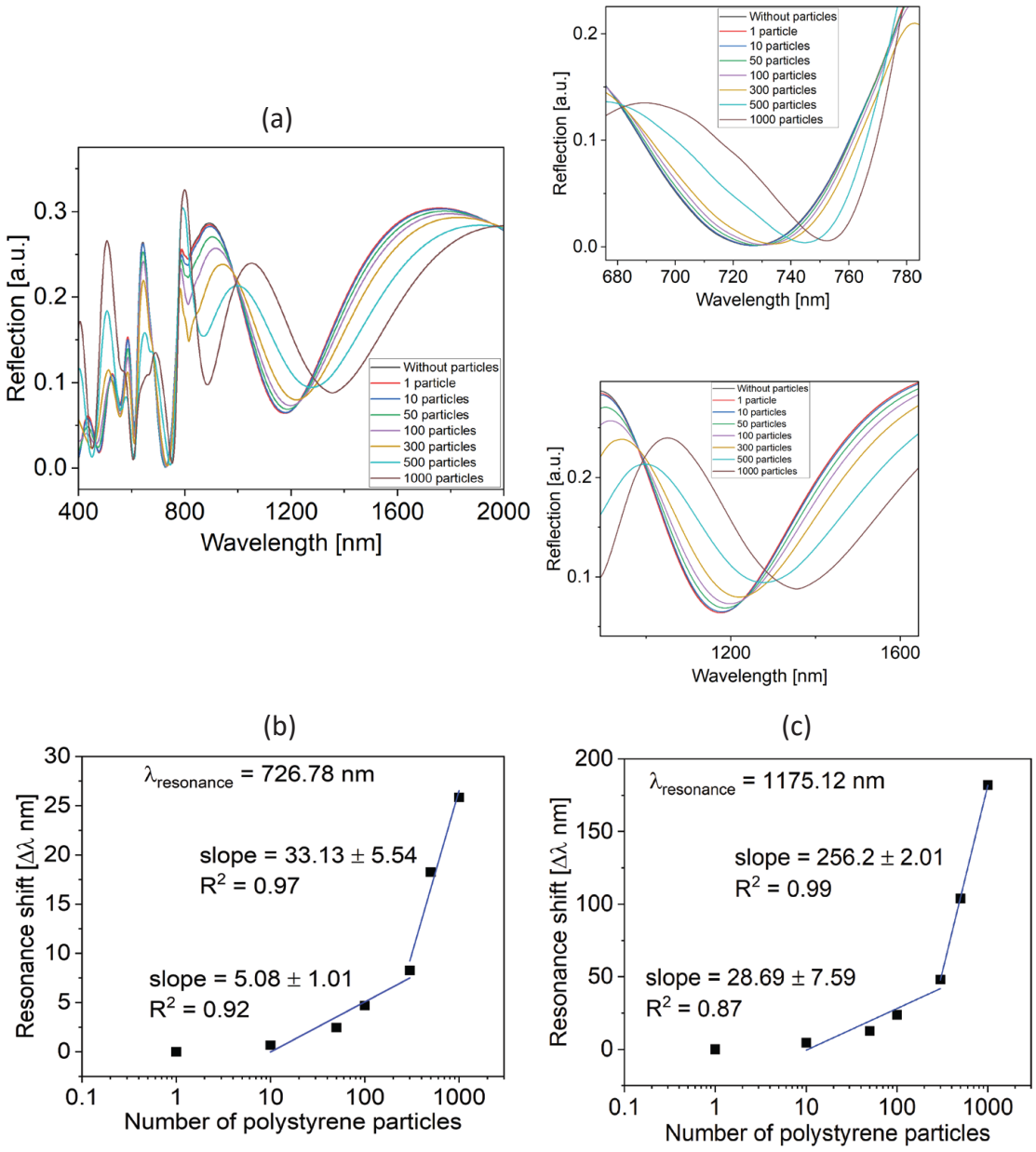

Figure 4.6: (a) Simulated reflection spectra of MIM_configuration_2 (configuration: D = 100 nm, P = 200 nm, thickness of Al_2O_3 layer = 20 nm, top Au layer = 20 nm and bottom Au layer = 90 nm.) with varying numbers of polystyrene particles present on the device surface. The enlarged view shows the resonance wavelength position shifts with the number of polystyrene particles. In (b) and (c) resonance shift response with the increase in the number of polystyrene particles and the slope of the curves (obtained from the linear fit response) defines the detection sensitivity. Here polystyrene particles diameter - 100 nm, and the broadband light source (400-2000 nm)is TM (p) polarized.

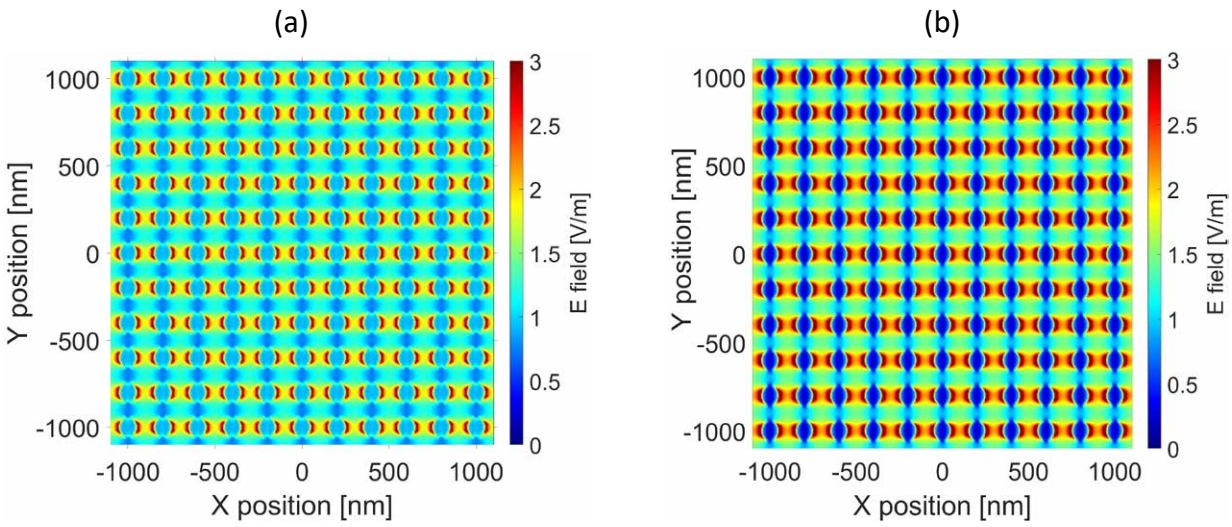

Figure 4.7: The E field distribution on the top surface of MIM nanopillars array (MIM_configuration_2) device at the resonance wavelength (a) λ = 726.78 nm, and (b) 1175.12 nm.

onators array: 100 nm diameter with 800 nm pitch, 20 nm height with 5 nm Ti adhesive) are shown in Fig. 4.8 (b) and (c).

We have performed the optical reflection measurements with our lab-made custom optical reflection spectroscopy setup and the details of the setup are given in the experimental methods section 5.2.5 of Chapter 5. We have used an unpolarized broadband light source (λ = 360 nm - 2600 nm) normal incident to the device and the reflection spectrum was collected to the Ocean Optics USB4000 spectrometer (wavelength range: 177 nm – 810 nm and resolution is 1.34 nm). Reflection measurements were performed with the presence of varying concentrations of polystyrene beads of 100 nm diameter on the device surface. The 100 nm-sized polystyrene beads were diluted in deionized (DI) water and concentrations ranged from 100 beads/μL to 700 beads/μL. Before measurement, each solution was vortex mixed, and from each concentration, 0.3 μL solution was drop-casted using a micropipette covering the 100 μm $\times$ 100 μm device surface area, and the DI water then evaporated by heating the chip at 60° C. Each concentration was measured on 3 devices on a single chip to obtain the statistics of resonance shift. The reflection spectra with the varying number of

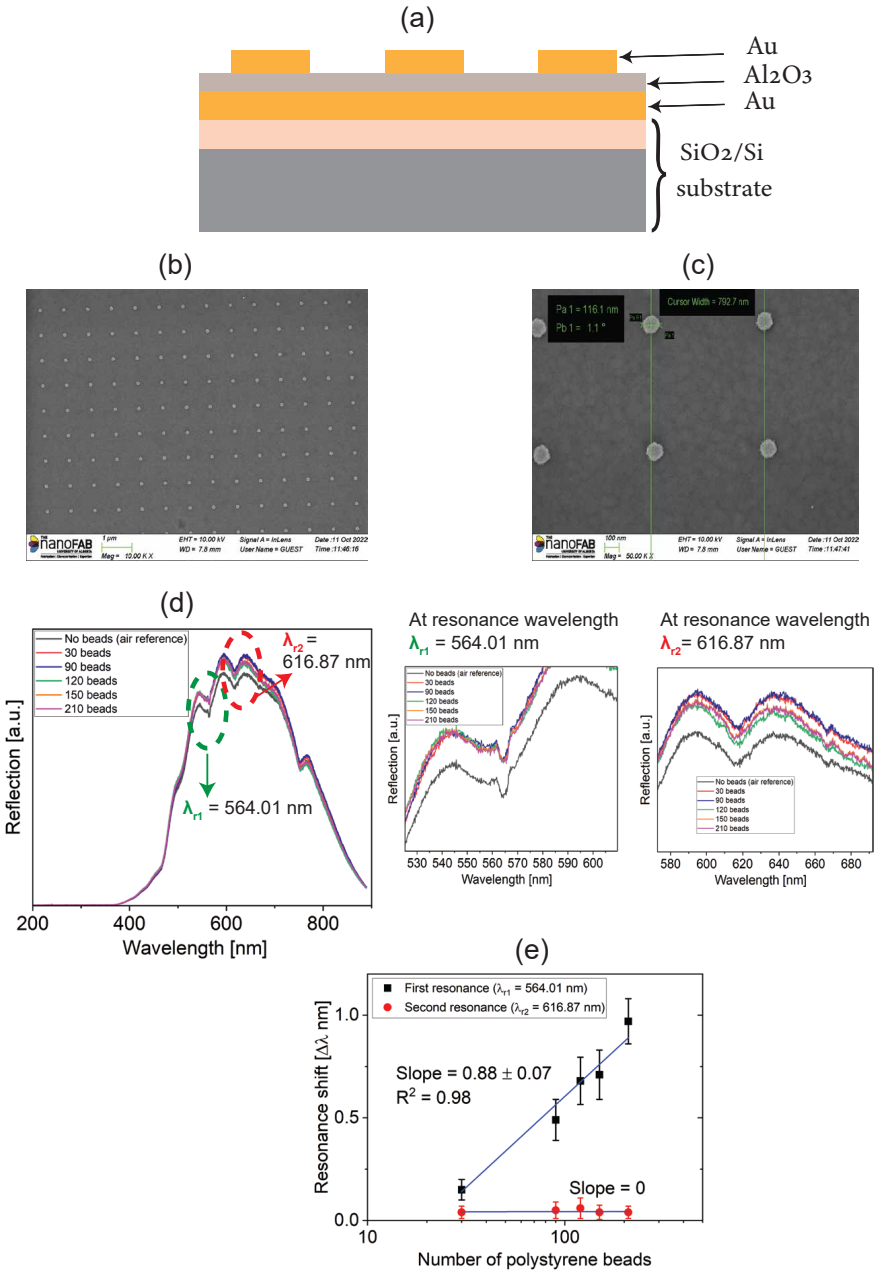

Figure 4.8: (a) The schematic illustration of MIM_configuration_1. (b) and (c) portray the SEM images of fabricated device of the configuration: 5 nm Ti/90 nm Au thin film/5 nm Ti/100 nm Al_2O_3 thin film/Au nanoresonators array of 100 nm diameter with 800 nm pitch, 20 nm height with 5 nm Ti adhesive layer. (d) The reflection spectra were measured by varying numbers of polystyrene beads with MIM_configuration_1 device. The zoomed-in view shows the two major resonance positions marked as $\lambda_{r1} = 564.01$ nm and $\lambda_{r2} = 616.87$ nm. (e) The resonance shift was observed at the $\lambda_{r1} = 564.01$ nm and plotted against the increase in the number of polystyrene beads and the detection sensitivity obtained 0.88 ± 0.07 nm/decade, whereas, resonance shift at $\lambda_{r2} = 616.87$ nm is negligible as observed.

beads are shown in Fig. 4.8 (d) and the two major resonance positions $\lambda_{r1} = 564.01$ nm and $\lambda_{r2} = 616.87$ nm are marked and the enlarged views are portrayed. The resonance shift with respect to the air reference is displayed in Fig. 4.8 (e) for both resonance positions. The detection sensitivity obtained from the slope of the curve $= 0.88 \pm 0.07$ nm/decade and extracted LOD (using equation 2.10) of 8 polystyrene beads at resonance wavelength $\lambda_{r1} = 564.01$ nm. Interestingly, there is no significant resonance shift observed at the second resonance position (as shown in Fig. 4.8 (e)). The first resonance occurs at a wavelength of $\lambda_{r1} = 564.01$ nm, due to the localized surface plasmon resonance (LSPR) of the array of Au nanoresonators. This means that the resonant field is available on the surrounding surface of each Au nanoresonator. As a result, the presence of any 100 nm-sized polystyrene particle can cause the resonance wavelength to shift. On the other hand, the second resonance at $\lambda_{r2} = 616.87$ nm is due to the waveguide mode generated by the stacked layers of the bottom Au mirror layer and the Al_2O_3 thin film. The guided mode is primarily confined in the Al_2O_3 layer and has no access to the top surface. Therefore, no resonance shift is observed due to the presence of polystyrene beads.

Similarly, we also performed reflection measurements of the MIM nanopillars array (MIM_configuration_2) shown in the schematic Fig. 4.9 (a). The simulation optimized device is fabricated (configuration: 5 nm Ti/90 nm Au/5 nm Ti/20nm Al_2O_3/5 nm Ti/20 nm Au, 100 nm diameter and 200 nm pitch), and the SEM image is portrayed in Fig. 4.9 (b). The device was tested with the same polystyrene bead concentrations. The reflection spectra are shown in Fig. 4.9 (c), and the enlarged view of resonance shift at $\lambda_r = 573.4$ nm is illustrated. The resonance wavelength red-shifts with the increase in number of polystyrene beads is shown in Fig. 4.9 (d) and detection sensitivity obtained $S = 6.54 \pm 0.7$ nm/decade for 100 nm sized polystyrene beads and extracted LOD (using equation 2.10) of 3 beads.

In Table 4.3, we have presented a comparison between the results obtained from

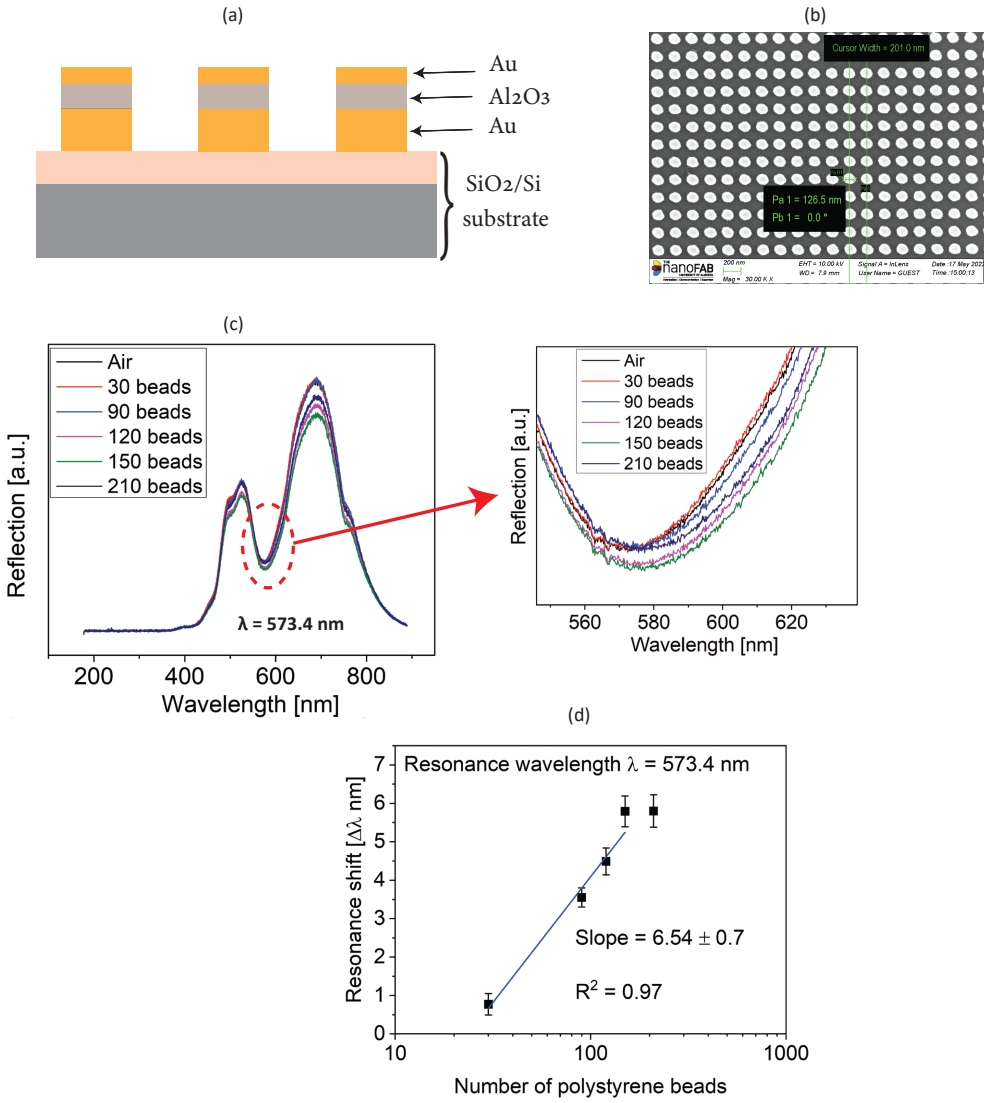

Figure 4.9: (a) Schematic illustration of MIM nanopillar array (MIM_configuration_2) device. (b) Top view SEM image of the fabricated MIM_configuration_2 device. (c) Reflection spectra were measured by varying the number of polystyrene beads. The resonance wavelength (red-circled) enlarged view demonstrates the shift in resonance wavelength (at $\lambda = 573.4$ nm). (d) The resonance shift against the number of polystyrene beads is shown, and the linear response's slope represents the detection sensitivity $S = 6.54 \pm 0.7$ nm/decade.

Table 4.3: Comparison of sensing parameters obtained from simulation and experimental studies of two MIM configurations. Units of the parameters are - Sensitivity (S): nm/decade, resonance linewidth (FWHM): nm, figures of merit (FOM): per number of polystyrene beads in log-scale, limits of detection (LOD): number of polystyrene beads.

Configurations	Simulation					Experiment				
	S	$FWHM$	$Q-factor$	FOM	LOD	S	$FWHM$	$Q-factor$	FOM	LOD
MIM_configuration_1	2.83	7.59 at $\lambda = 850$ nm	111.98	0.37	10	0.88	23.53 at $\lambda = 564.01$ nm	23.96	0.03	8
MIM_configuration_2	33.13	96.18 at $\lambda = 726$ nm	7.54	0.34	10	6.54	91.22 at $\lambda = 573.4$ nm	6.28	0.07	3

simulation and experimental studies. Our findings show that the MIM_configuration_2 has a higher capability of particle detection both in simulation and experimental measurement as compared to the MIM_configuration_1. However, the resonance wavelength positions obtained from FDTD simulations are different from the fabricated devices due to variations in the dimensions of the nanoresonator and the roughness of its surface and sidewalls, which affect the resonance characteristics. The higher sensitivity of MIM_configuration_2 is due to the leaky behaviour of individual MIM nanopillars and a larger surface area. The resonance field in this type of MIM nanoresonator structure leaks out and becomes localized on the top and sidewall surface of the nanopillars. As a result, if there are particles present on the top surface, they disturb the resonance field, leading to a higher resonance shift. This in turn provides a higher detection sensitivity. In comparison, the waveguide resonance mode is mostly confined within the Al_2O_3 thin film layer of MIM_configuration_1, resulting in weaker interaction with polystyrene particles and a lower sensing response. On the other hand, the LSPR field generated from the Au nanoresonators exists on the surface and contributes to the measured sensitivity in MIM_configuration_1. This leaky behaviour of MIM_configuration_2 is evident from the larger FWHM (both with simulation and experiment) at resonance position in case of MIM_configuration_2 compared to the MIM_configuration_1. This highlights the MIM_configuration_2 with leaky resonance is a more efficient platform for biosensing and is expected to deliver more accurate

and sensitive results, thereby enhancing the overall quality and reliability of biosensing applications.

Fabricating MIM configurations comes with several challenges. These include: (a) the process of evaporating oxide thin film stacks with metal thin films for lift-off is not perfect, (b) etching metal and oxide film stacks is difficult due to limitations of the highly selective etching mask, and (c) integrating 2D materials such as, MoS_2 sandwiched between two metal layers is challenging because of the high-temperature growth of 2D materials which generates defects on the metal thin films.

4.4 Summary

In this chapter, we have discussed the design, fabrication process, and experimental measurements of two different MIM nanoresoantor configurations. We have validated the FDTD simulation optimized design with the varying concentrations of 100 nm sized polystyrene beads by our custom-made optical setup (optical reflection spectroscopy). In simulation, the MIM nanopillar array (MIM_configuration_2) demonstrates the best sensitivity of 256.2 $\pm$ 2.01 nm/decade at resonance λ = 1175.12 nm compared to sensitivity 9.58 $\pm$ 1.38 nm/decade at resonance λ = 1087.2 nm of MIM_configuration_1. In experimental bead testing measurement, MIM_configuration_2 shows the best detection sensitivity of $S = 6.54 \pm 0.7$ nm/decade compared to the $S = 0.88 \pm 0.07$ nm/decade of MIM_configuration_1. The sensitivity is higher with the MIM_configuration_2, which is because of the controlled leaky nature of individual MIM nanopillar and the higher surface area of the MIM geometry. Also, for specific bioanalyte detection, the Au surface can be biofunctionalized accordingly. For SARS-CoV-2 detection, the functionalization steps discussed in chapter 5 can be used to attach the SARS-CoV-2 on the device surface.

As discussed earlier, the fabrication challenges of MIM resonator configurations have limited our exploration of other insulator materials such as TiO_2 and MoS_2, which we have previously demonstrated in Chapter 3. Therefore, we propose to investigate the

use of pure plasmonic metal nanoresonators and dielectric/semiconductor metasurfaces for detecting small-sized bioanalytes. Details on this proposal will be discussed in the upcoming chapters.

Chapter 5

Ultra-sensitive detection of SARS-CoV-2 with functionalized gold plasmonic nanoresonator array

5.1 Introduction

In Chapter 3 and Chapter 4, we discussed the configurations of metal-insulator-metal (MIM) nanoresonators. Our goal was to obtain the best structural parameters of MIM nanoresonators to achieve the best sensitivity for detecting SARS-CoV-2 with ultra-low concentration using 100 nm-sized polystyrene particles. However, different types of MIM configurations pose various fabrication challenges, which can increase the cost and complexity of mass production. In this context, localized surface plasmon resonance (LSPR) sensors based on pure plasmonic metal nanoresonators have great potential. One of the key advantages of localized surface plasmon resonance (LSPR) based biosensors is that induced resonant field is available only within $\backsim$100 nm surrounding the nanoresonator surface, and this greatly reduces the signal interference effects due to the presence of other elements in the bulk sample solution [140]. Early diagnosis and rapid testing reduce transmission rates of virus infection, and we need point-of-care devices for that purpose. LSPR-based biosensors have been demonstrated to detect different bioanalytes such as virus [62], bacteria [62], proteins [141],

etc. A few works have reported surface plasmon resonance-based SARS-CoV-2 detection. G. Qiu et.al.[142] have reported Au nanoislands-based plasmonic photothermal biosensor to detect specific gene sequences of SARS-CoV-2 with a limit of detection (LOD) 0.22 pM from a multigene mixture. Another recent work [143] demonstrated SARS-CoV-2 spike protein S1 detection using a plasmonic toroidal metasurface with the LOD 4.2 fM.

Our study focuses on designing using the FDTD simulations and fabrication of a leaky Au nanoresonator-based biosensing platform for SARS-CoV-2 detection with a uniform sensitivity over a 100 μm $\times$ 100 μm active sensing area. The Au nanoresonator array was optimized to detect 100 nm-sized bioanalytes as it matches the size of SARS-CoV-2. We have biofunctionalized the fabricated devices (as illustrated in Fig. 5.1) and demonstrated the SARS-CoV-2 virus-like particles (VLPs) detection of varying concentrations.

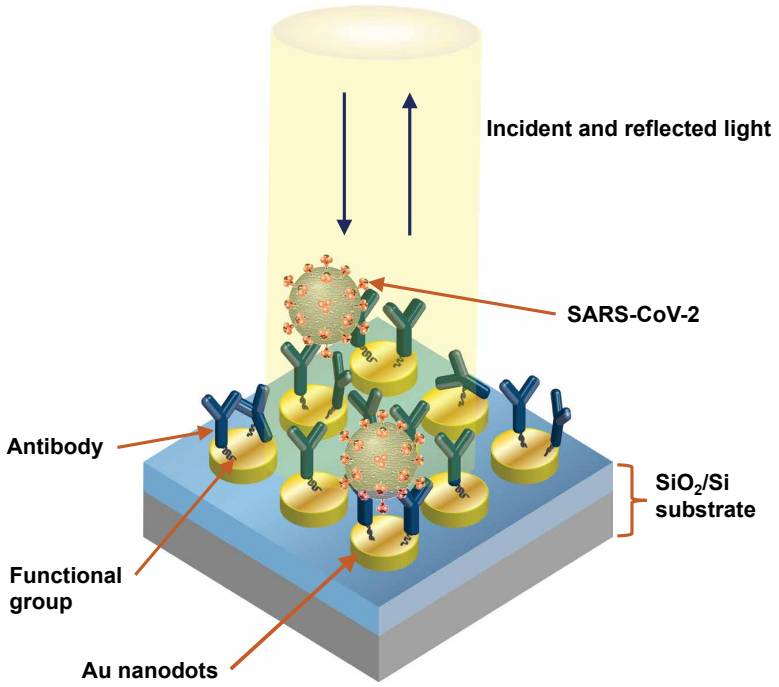

Figure 5.1: Schematic image illustrates the surface functionalized Au nanoresonator array for SARS-CoV-2 virus-like particle detection. We have used a normal incident unpolarized broadband light source for excitation and reflected light collected to a spectrometer via an optical fiber.

5.2 Materials and Methods

5.2.1 Simulation Method

Here, we have performed design simulation of Au nanoresonator array by finite difference time domain (FDTD) simulations using commercially available FDTD solution software package (Ansys Inc.[108]). The details of the FDTD simulations are provided in Appendix A. Simulations were performed by varying the diameter (D) and pitch (P – center to center distance between two adjacent nanoresonators) of Au nanoresonators while keeping the height of each Au nanoresonator fixed at 50 nm. Periodic boundary conditions were applied in both X and Y directions, perfectly matched layer (PML) in Z directions (see schematic illustration of simulation set up in Appendix Fig. B.1(a)). The mesh size used was 5 nm^3. An array of 11 $\times$ 11 Au nanoresonators was placed on the top of SiO_2/Si substrate. A broadband (λ = 400 – 2000 nm) plane wave source was placed above the Au nanoresonator array for reflection simulation. The reflection spectrum was collected by placing a frequency domain two-dimensional (2D) monitor behind the source injection plane. The reason is both the incident and reflected light are present at the front of the source, whereas only the reflected light field is present behind the source plane. The reflection spectrum was collected using separate TE (s-polarized) and TM (p-polarized) plane wave sources. The reflection spectra are identical for both polarizations owing to the circular shape geometry of each nanoresonator (supplementary Fig. B.1(b)). Therefore, reflection spectra recorded with the TM polarized (p-polarized) light source were used for the rest of the simulation study. Resonance shifts from the simulated spectra were further analyzed using Origin and MATLAB.

5.2.2 Materials and reagents

Polystyrene beads of diameter 100 nm and 3 μm were purchased from Sigma-Aldrich and Polysciences Inc., respectively. 10$\times$ Phosphate buffered saline (PBS) stock so-

lution, dimethyl sulfoxide (DMSO), Tris base, Dulbecco's Modified Eagle Medium (DMEM), and ultrapure water were purchased from Fisher Scientific. 10× PBS was diluted using ultrapure water to obtain 1×PBS solution (pH = 7.4). Tris base was dissolved in ultrapure water, and concentrated HCl was added to prepare 1M Tris-HCl solution (pH = 7.5). 3,3'-dithiodipropionic acid di(N-hydroxy succinimide ester) (DSP) was purchased from Sigma Aldrich. Recombinant Anti-SARS-CoV-2 spike S1 antibody (1 mg/mL) was purchased from antibodies-online Inc. SARS-CoV-2 spike S1 antibody was diluted to 250 μg/mL with 1×PBS solution. SARS-CoV-2 virus-like particles (VLPs) in DMEM were purchased from Virongy. The concentrated VLP solution contains approximately 10^8 copies of VLPs per μL. The VLP solution was diluted using DMEM for measurements.

5.2.3 Fabrication of gold nanoresonators array

The Au nanoresonator array is fabricated by electron beam lithography (EBL) using the Raith150 Two EBL system available at the Nanofab facility at the University of Alberta. 10 mm × 10 mm SiO_2/Si substrate pieces were piranha cleaned and baked at 180°C for 5 minutes on a hotplate for fabricating the Au nanoresonator array. ZEP 520A positive tone EBL resist was spin-coated (spin speed: 5000 (rpm), ramp: 2000 (rpm/sec), spin time: 40 sec) on them by Brewer spinner and baked again at 180°C for 1 minute. During the EBL patterning, we optimized the EBL exposure parameters: 10 kV, 20 μm aperture, and 100 μC/cm^2 area dose. 100 μm × 100 μm write field and 1000× magnification was used to expose the 100 nm diameter and 200 nm pitch patterns. 3 × 3 arrays of Au nanodots with 100 μm area were exposed, and the resist was then developed using ZED N50 developer for 15 sec and MIBK:IPA (1:3) for 10 sec subsequently at room temperature and dried with N_2 gun immediately. We have deposited 50 nm thick Au with a 5 nm Ti adhesive layer on the patterned substrates using the electron beam evaporation technique. After the gold deposition, the substrates were sunk into the hot remover PG bath and placed

at a hotplate at 75°C. After every 40 minutes of the whole 2-hour lift-off process, the remover PG solution was changed to a fresh solution to avoid any re-deposition. Also, the remover PG containing the glass petri dish was shaken manually to prevent the lift-off gold residue from sticking to the nanostructures. After the gold lift-off, the substrates were cleaned with isopropyl alcohol (IPA) solution and dried with N_2 gun. The details of the fabrication process flow are illustrated in Appendix Fig. B.2.

5.2.4 Functionalizing Au nanoresonators with SARS-CoV-2 antibodies

The Au nanoresonator arrays were functionalized with SARS-CoV-2 spike S1 antibodies using DSP self-assembled monolayer (SAM). During the functionalization, the disulfide bond of DSP breaks and is chemisorbed on the Au surface, whereas the NHS-ester (N-hydroxysuccimide ester) part of DSP is reactive to the amine groups of proteins such as anti-SARS-CoV-2 spike S1 antibody. The Au nanoresonator arrays were cleaned with chloroform, acetone, isopropanol (IPA), deionized (DI) water, and dried under nitrogen. 10 mM DSP solution was prepared using DMSO for each reaction. The Au nanoresonator arrays were immersed in 10 mM DSP solution for 30 minutes at room temperature to activate the surface with DSP functional groups. After the reaction, the devices were rinsed thoroughly with DMSO and DI water and dried under nitrogen. Then, the SARS-CoV-2 spike S1 antibody solution (250 μg/mL in PBS) was immediately added to the DSP-modified Au nanoresonator arrays using a micropipette and left for 2 hours under ambient conditions. The device was rinsed several times with 1×PBS and DI water to remove non-specific adsorption and reaction by-products. Lastly, the un-reacted DSP was quenched by immersing the Au nanoresonator arrays in 1 M Tris-HCl buffer (pH = 7.5) for 15 minutes, and the chip was washed with DI water and 1×PBS after the reaction. The functionalized Au nanoresonators were stored in 1×PBS solution at 4°C before measurements.

Different concentrations of SARS-CoV-2 virus-like particles (VLPs) were prepared

by diluting the VLPs with DMEM medium. We prepared varying concentrations of SARS-CoV-2 VLPs containing 10^0 VLPs/μL to 10^4 VLPs/μL on the day of measurements, and all the concentrations were stored in 4°C before measurements. For testing with different VLP concentrations, 50 μL solution of a particular concentration was drop cast onto the 9 devices and was incubated for 1 hour to ensure the antibody-antigen binding reaction of SARS-CoV-2 VLPs with the antibodies. After the incubation period of a particular VLP concentration, the chip was washed with DMEM solution to remove any unbound VLPs, and then 50 μL of fresh DMEM solution was added before the measurement to ensure that there was no signal acquired from unspecific adsorption of VLPs.

5.2.5 Optical measurement setup

We have made a customized optical setup in our lab, and the photograph is shown in Fig. 3(a). Optics setup consists of a broadband light source SLS201L (λ = 360 – 2600 nm) from Thorlabs Inc. [144]. The light is collimated with the collimator connected to the light source and then incident onto the two mirrors (M1 and M2) placed at 45° angles to each other in free space. The reflected light from the M2 mirror was again passed through a collimator, and then incident on the 50:50 beam splitter (model: BSW26, λ = 350 – 1100 nm) placed 45° angles to the light path to get a beam vertically normal incident to the microscope objective. Nikon PLAN 10×/0.25 microscope objective with a working distance of 10.5 mm was used to focus the light on the substrates mounted on the XYZ translation stage. The longer working distance objective lens was chosen to ensure the lens did not touch the solution on the chip during measurements. The reflected light from the Au nanoresonators array on SiO_2/Si substrates was collected with the same objective lens and passed through the beam-splitter and focused via a lens with a focal length of (F) = 100 mm and $f/4$ which is matched with the spectrometer's f-number. An optical fiber was placed exactly at the focal point of the collection lens to direct the reflected light to the

spectrometer connected to it on the other end of the fiber. We used an Ocean Optics USB4000 spectrometer with a wavelength range between 177 nm – 889 nm and a resolution of 1.34 nm. The beam spot size is approximately 800 μm. The blue arrow in Fig. 5.3(a) displays the light path through the optical components. A CCD camera (model: Chameleon CMLN-13S2M Point Grey Research) was used to locate the devices on the chip, and the XYZ translation stage was used to align each device to the center of the beam spot. The spectrometer's optical fiber replaced the camera to collect reflected light. The spectrometer's optical fiber replaced the camera to collect the reflected light. Post-processing and signal analysis to calculate the resonance shift were performed by Origin and MATLAB.

5.3 Results and Discussions

5.3.1 Design Simulations

FDTD simulations were performed on Au nanoresonator arrays by varying the diameter (D) and pitch (P), two crucial design parameters for plasmonic field localization. Here, we have chosen Au as the plasmonic material for the nanoresonators, because it is a chemically stable plasmonic metal (less chance of oxidation compared to other plasmonic metals e.g., Ag, Cu & Pt, etc.) which can be biofunctionalized [145]. The nanoresonator size was chosen to obtain a larger overlap of the strongly localized resonant plasmonic field surrounding individual Au nanoresonators with bioanalytes such as SARS-CoV-2. The disturbance of the plasmonic field due to the presence of the bioanalyte induces a red-shift in the resonance wavelength ($\Delta\lambda$ nm). The following parameters demonstrate the performance of the Au nanoresonator array sensor:
Sensitivity (S): The resonance shift ($\Delta\lambda$ nm) to the change in the number of the analytes or the concentration of analytes (Δc beads or VLPs per μL) is defined as the detection sensitivity denoted by the following equation.

$$S = \frac{\Delta\lambda}{\Delta c} \tag{5.1}$$

Resonance linewidth ($\delta\lambda$ nm): Full-width at half maximum (FWHM) at resonance wavelength. The larger $\delta\lambda$ value defines leaky resonance and low Q-factor.

Limit of detection (LOD): The minimum number or concentration of bioanalytes that can be detected represents LOD. To extract the LOD from our experimental measurements, we have utilized the three-sigma rule, defined in the equation 2.10.

Figure of Merit (FOM): Figure of merit is one of the useful metrics to describe the performance and is defined as the ratio of the sensitivity (S) to the full width at half maximum (FWHM) ($\delta\lambda$ nm).

$$FOM = \frac{S}{\delta\lambda} \tag{5.2}$$

Here, we have chosen the nanoresonator's diameter of 100 nm, 150 nm, and 200 nm with the corresponding pitch - 200 nm, 250 nm, and 300 nm, respectively, with a height of 50 nm to perform FDTD simulation. The edge-to-edge gap of two neighboring nanoresonators was kept at 100 nm so that SARS-CoV-2 could be positioned between the two nanoresonators depending on the antibody's orientation and analytes do not fall onto the substrate. A schematic of the Au nanoresonators array on SiO_2/Si substrate is shown in Fig. 5.2(a). Resonant plasmonic field ($|\mathbf{E}|^2$) distribution (see Fig. 5.2(b)) recorded on the Au nanoresonators array (diameter – 100 nm and pitch – 200 nm) surface displays the field coupling between the neighboring Au nanoresonators which makes the whole surface sensitive. This helps to achieve a stronger interaction with the target bioanalytes. To verify the sensing capability of our proposed platform, polystyrene particles of 100 nm diameter were distributed (Gaussian distribution) over the surface of Au nanoresonators, and the resonance shift was calculated by varying the number of particles. Here, we have used polystyrene as the constituent material of the 100 nm sized particles (matching with the size of SARS-CoV-2 [146]) in simulation because the refractive index of polystyrene ($n = 1.4519$) in the visible wavelength range matches well with most of the bioanalytes [147]. There are multiple resonance dip positions present on the reflection spectrum, but we have chosen only one that is in the visible wavelength range so that, experimentally, we

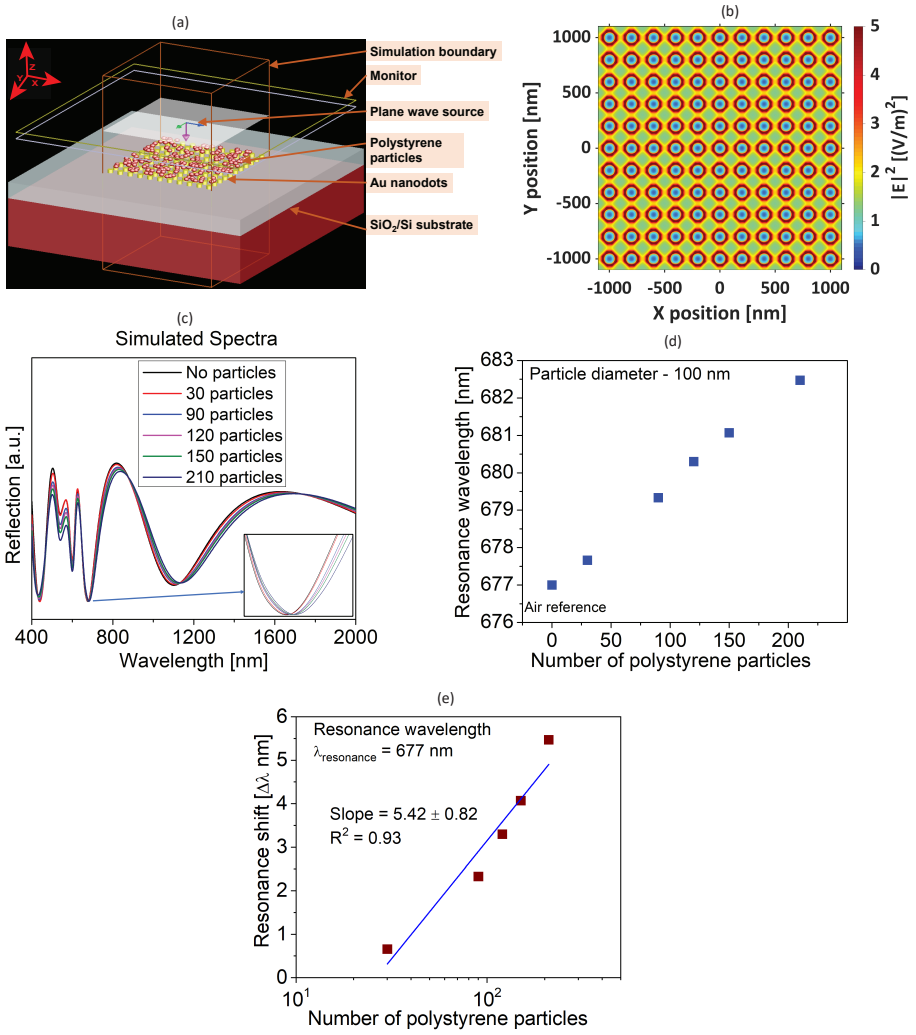

Figure 5.2: Design simulation: (a) Schematic shows the FDTD simulation set up, where a broadband plane wave source (λ = 400 – 2000 nm) is placed on the top, and light is normal incident on the Au nanoresonators array. Here, the plane wave source is TM polarized. 100 nm-sized polystyrene particles are distributed (Gaussian) on the Au nanoresonator surface. The reflected light was recorded by a 2D monitor placed above the plane wave source. We have used an 11 $\times$ 11 Au nanoresonator array with periodic boundary conditions in X and Y directions and perfectly matched layer (PML) boundary conditions in Z direction. (b) The top view of $|\mathbf{E}|^2$ obtained from D = 100 nm and P = 200 nm array configuration shows the plasmonic field intensity distribution and coupling among the Au nanoresonators makes the whole surface sensitive. (c) Reflection spectra were recorded by the 2D monitor for varying numbers of polystyrene particles. The enlarged view in the inset displays the resonance shift with the increased number of polystyrene particles. (d) Resonance wavelength positions were plotted against the number of polystyrene particles. (e) The semi-log plot shows the resonance shift ($\Delta\lambda$ nm) calculated to the air reference (when no particles are present λ = 677 nm) and depicts a linear red-shift with the number of particles with the sensitivity = 5.42 $\pm$ 0.82 nm/decade.

can use a silicon photodetector array to measure the reflection spectrum. The dip in the reflection spectrum (black line referring to the air background reference) in Fig. 5.2(c) shows the resonance peak position at $\lambda = 677$ nm. This resonance wavelength linearly red-shifts with the increase in the number of particles (see the enlarged view of spectra in Fig. 5.2(c) inset) on the Au nanoresonators array surface, shown in Fig. 5.2(d). The calculated resonance shift with the increase in the number of polystyrene particles is shown in Fig. 5.2(e), and the slope of this curve represents sensitivity based on eqn 5.1.

The sensitivity of the nanophotonic platform with different sets of design parameters is presented in Table 5.1. The detection sensitivity of the polystyrene particle (100 nm diameter) decreases with an increase in the diameter of the individual Au nanoresonator. The highest sensitivity (slope of the resonance shift curve in Fig. 5.2(e)) S = 5.42 nm/decade is obtained with a diameter of 100 nm and pitch of 200 nm Au nanoresonator array configuration. This bolsters the fact that the Au nanoresonator's diameter and pitch play a significant role in detecting 100 nm particles, which matches the size of SARS-CoV-2. Here, we have focused on the resonance shifts in the visible range only to make the design compatible with a portable point-of-care system using LEDs as the light source and a silicon photodiode array.

Table 5.1: FDTD simulation with varying design parameters: diameter (D in nm) and pitch (P in nm) of Au nanoresonators considering fixed height of 50 nm.

Configurations		Sensitivity
Diameter (nm)	Pitch (nm)	(nm/decade)
100	200	5.42
150	250	4.97
200	300	2.86

5.3.2 Testing with polystyrene beads

We have considered the best design parameters D = 100 nm and P = 200 nm to fabricate the Au nanoresonator array devices. For experiments, a 3 × 3 Au nanoresonator

array with 9 devices was fabricated on SiO_2/Si substrate. Each Au nanoresonator array size is 100 × 100 μm^2, and the edge-to-edge gap between two adjacent arrays was designed to be 1.4 mm, so there would not be any signal interference from adjacent devices while measuring one device. Detailed fabrication process steps are discussed in experimental methods, and the schematic in Appendix Fig. B.2 shows the process flow. Our customized optical setup for the reflection spectroscopy measurements is displayed in Fig. 5.3(a), and the details are described in the experimental methods (optical measurement setup) section. The scanning electron microscope (SEM) image of the fabricated Au nanoresonator array is shown in Fig. 5.3(b). To verify the sensitivity obtained from the simulation results, we measured the reflection spectra (as shown in Fig. 5.3(c)) of the Au nanoresonator array with the presence of polystyrene beads. The measured spectra in Fig. 5.3(c) show that the resonance position is red-shifted with the increase in the number of polystyrene beads (see the enlarged view in Fig. 5.3(c) inset) which confirms our simulation results.

To confirm the repeatability, each concentration was measured on 6 separate devices of 2 different chips. The resonance wavelength position for $n = 6$ repetitions is shown in Fig. 5.3(d). Resonance shift ($\Delta\lambda$ nm) was calculated with respect to the air background reference $\lambda_{air(mean)} = 579.05 \pm 0.58$ nm (mean resonance wavelength position for $n = 6$ devices). The detection sensitivity (S) was calculated from the slope of the linear response of the resonance shift curve (see Fig. 5.3(e)) as $S = 17.05 \pm 3.25$ nm/decade and extracted LOD of 7 polystyrene beads. The resonance line width (FWHM) at $\lambda = 579.05$ nm is 127.6 nm, and we obtain a Q-factor of 4.5, demonstrating the leaky nature of the Au nanoresonator array. Experimental demonstration of 100 nm sized polystyrene beads detection highlights the capability of our proposed Au nanoresonator array device for small bioanalytes (e.g., SARS-CoV-2, H1N1 influenza virus, or other 100 nm sized viruses) detection. A notable observation is that the experimentally measured sensitivity ($S = 17.05 \pm 3.25$ nm/decade) is higher than the simulated sensitivity ($S = 5.42$ nm/decade) for 100 nm-sized beads. Following

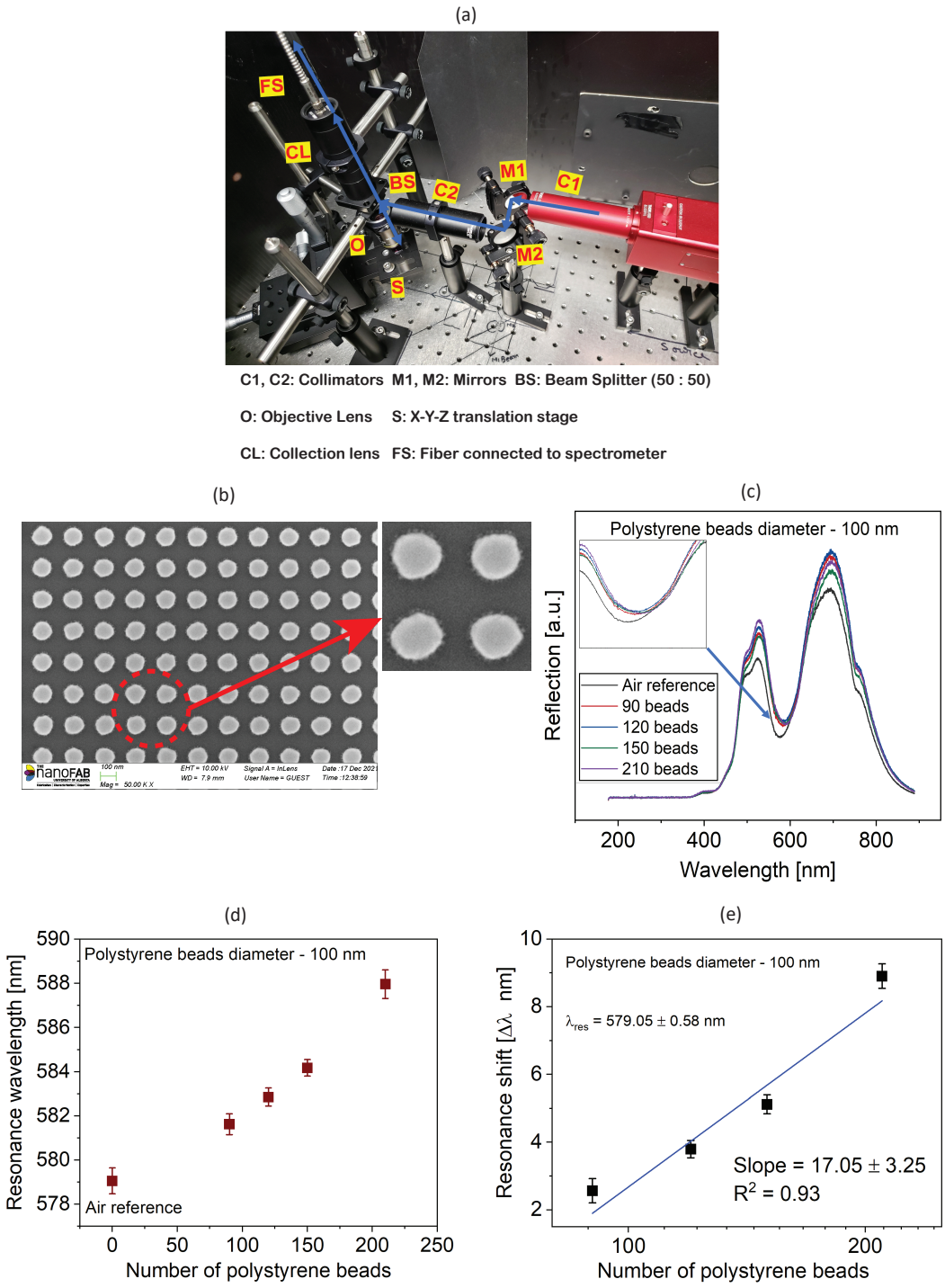

Figure 5.3: (a) Customized optics setup for reflection measurements. (b) scanning electron microscope (SEM) image shows the Au nanoresonator array. The enlarged view displays Au nanoparticles surrounding each Au nanoresonator. (c) Reflection spectra correspond to single device measurements with varying numbers of 100 nm-sized polystyrene beads. The Inset image shows that the resonance position red-shifts as the number of beads increases. (d) The mean resonance position ($n = 6$ repetitions on six separate devices) shows the linear shift with the number of beads. (e) Semi-log plot of resonance shift ($\Delta\lambda$ nm) versus the number of polystyrene beads, where $\Delta\lambda$ was calculated to the air reference position ($\lambda_{air} = 579.05 \pm 0.58$ nm). The sensitivity obtained 17.05 ± 0.58 nm/decade.

lift-off, the Au nanoresonators are encircled by Au nanoparticles, as evidenced by the magnified view of the SEM image in Figure 5.3 (b). The combined localized surface plasmon resonance signal emanating from the Au nanoparticles encircling each Au nanoresonator greatly amplifies the signal. Consequently, a more substantial resonance shift is observed, leading to higher detection sensitivity for 100 nm polystyrene beads. The device design (diameter and pitch of Au nanoresonators) can easily be modified to detect other bioanalytes of different dimensions. The detection of 3 μm diameter polystyrene beads has been shown in Appendix Fig. B.3(a) and (b) with the same Au nanoresonators array device with a sensitivity of $S = 1.92 \pm 0.28$ nm/decade.

Bead measurement results demonstrate that the plasmonic field interaction varies with the size of beads, which also impacts the sensitivity. The leaky resonant plasmonic field by the optimized Au nanoresonator array (D = 100 nm and P = 200 nm) has a larger overlap with the 100 nm sized beads, which are either positioned on the Au nanoresonators surface or at the gap between two adjacent Au nanoresonators, compared to the 3 μm sized polystyrene beads. Thus, the 100 nm beads have a higher detection sensitivity than the 3 μm beads.

5.3.3 SARS-CoV-2 virus like particles (VLPs) detection

We fabricated new sets of Au nanoresonators array devices and used them for biofunctionalization. The reagents and materials used for surface activation and biofunctionalization steps are discussed in experimental methods. Schematic Fig. 5.4(a) illustrates the steps for antibody functionalization and SARS-CoV-2 VLPs immobilization on the Au nanoresonator array. The reference reflection spectra for the fabricated devices were measured before functionalization. Two reference spectra were measured: (i) with air background (black curve) and (ii) with DMEM solution (red curve) shown in Fig. 5.4(b). 50 μL DMEM solution was used to ensure full coverage of all the 9 devices on the chip for all the measurements carried out in the

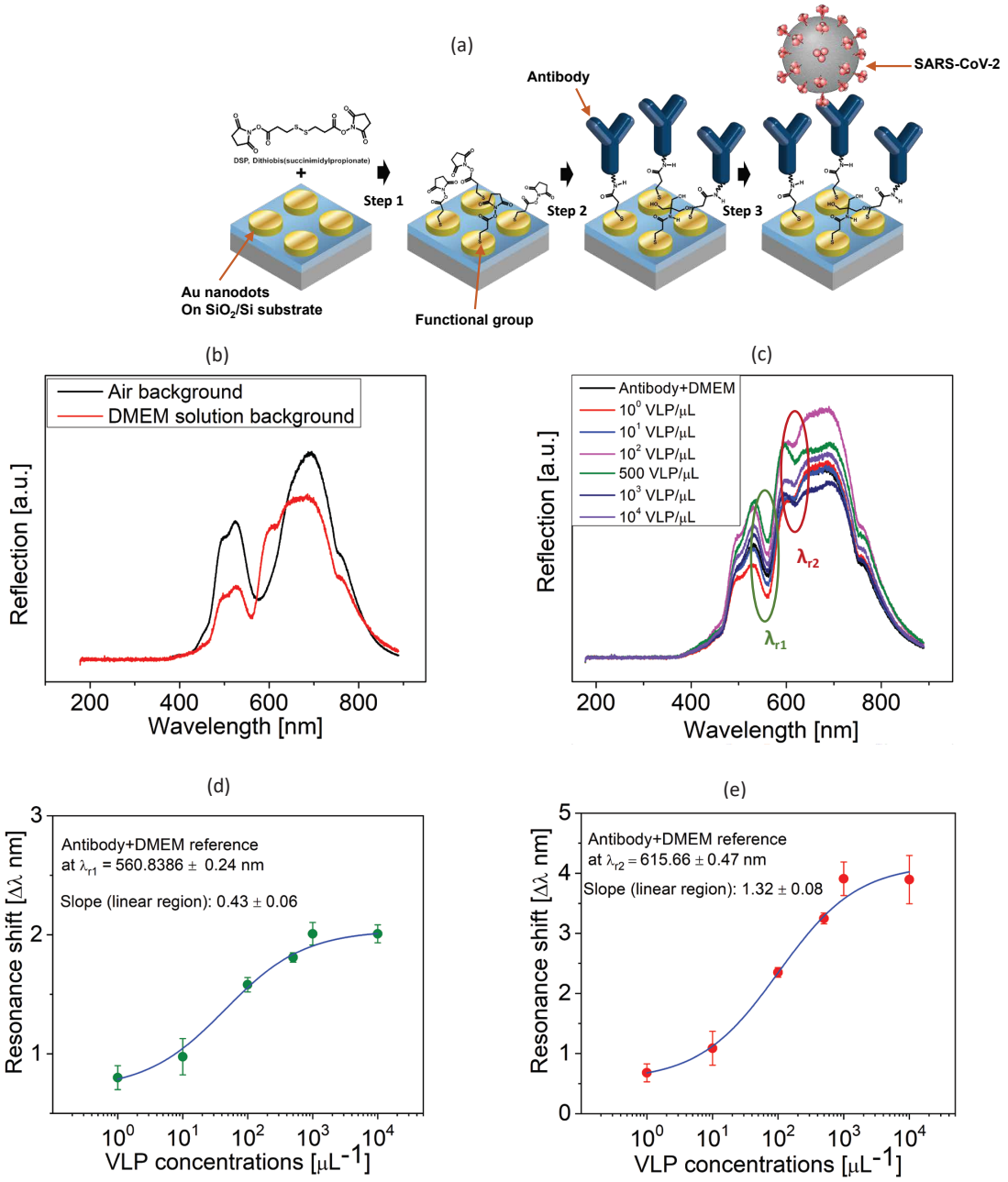

Figure 5.4: (a) Schematic illustration shows the functionalization steps and SARS-CoV-2 virus-like particles binding steps. (b) Fabricated Au nanoresonator arrays (D = 100 nm and P = 200 nm) were first measured in air background (black curve), and DMEM solution background (red curve) shows the resonance characteristics. (c) After antibody functionalization, devices were measured with 50 μL DMEM (black curve) presence. The resonance positions with the presence of antibody $\lambda_{1\_antibody} = 560.83 \pm 0.24$ nm and $\lambda_{2\_antibody} = 615.66 \pm 0.47$ nm, which are used as the reference for measuring VLP concentrations. VLP concentrations ranging from 10^0 μL^{-1} – 10^4 μL^{-1} were tested on all 14 devices of 2 different chips. (d) The resonance shift curve with respect to the $\lambda_{1\_antibody}$ = 560.83 ± 0.24 nm and the linear region shows the sensitivity $S_{r1} = 0.43 \pm 0.06$ nm/decade and (e) shows the resonance shift with respect to the $\lambda_{2\_antibody} = 615.66 \pm 0.47$ nm and sensitivity achieved $S_{r2} = 1.32 \pm 0.08$ nm/decade. The sigmoidal fit curve shows the LOD of 1 VLP μL^{-1} for both resonance positions.

solution environment. The device resonance position was observed at λ_{air} = 578.60 ± 0.50 nm for the air background, whereas two separate resonance dips λ_{1_DMEM} = 560.21 ± 0.07 nm and λ_{2_DMEM} = 615.08 ± 0.04 nm are found in the DMEM spectrum as shown in Fig. 5.4(b). The λ_{1_DMEM} = 560.21 ± 0.07 nm matches with the absorption peak of DMEM reported [148], whereas the resonance at λ_{2_DMEM} = 615.4 nm is related to the change in surface refractive index with the addition of DMEM solution (from $n = 1$ (air) to $n = 1.33$ (DMEM) [148]) induces LSPR shift of Au nanoresonator array.

A SiO_2/Si substrate half-covered with Au thin film (50 nm thick Au with 5 nm Ti adhesive layer) was used to verify the surface activation conditions by the self-assembled monolayer of DSP functional group (as shown in step 1 of schematic Fig. 5.4(a)). We confirmed that the DSP group has high selectivity to the Au surface as compared to the SiO_2 substrate surface (detailed discussion in Appendix B and FTIR spectra are presented in Fig. B.4). We then proceeded with activation of the Au nanoresonators' surface (of all the 9 devices in a single chip) with the self-assembled monolayer of the DSP functional group (as shown in step 1 of schematic Fig. 5.4(a)) and anti-SARS-CoV-2 spike S1 antibody was attached on the Au nanoresonators array (step 2 of schematic Fig. 5.4(a)) with the process step discussed in the experimental methods section. The reflection spectrum corresponding to the antibody (black curve shown in Fig. 5.4(c)) was collected after antibody attachment and adding 50 μL fresh DMEM covering all 9 devices. During the fabrication process, one device got scratched, and therefore, the defective one in the 3×3 array was ignored during measurements, and the other 8 devices were measured. To verify the repeatability of our measurements and process steps, we have measured 14 devices of 2 different chips. After the reflection measurements, the chip was submerged into fresh DMEM solution and stored in 4°C to avoid denaturing of the antibody. SARS-CoV-2 VLP solution was then added to these antibody functionalized devices (preparation of VLPs is discussed in the experimental methods section) starting from the lowest concentration (10^0 VLP μL^{-1})

and gradually increased to higher concentration (10^4 VLPs μL^{-1}). SARS-CoV-2 VLP reflection spectra were measured from all the functionalized devices, and the spectra corresponding to different VLP concentrations are presented in Fig. 5.4(c), where the two distinct resonance locations are marked as λ_{r1} and λ_{r2}. The resonance shifts from all 14 devices with respect to the antibody reference were analyzed, and the results are presented in Fig. 5.4(d) and (e). The sigmoidal curve fit for both the 5.4(d) and (e) curves demonstrates the upper limit of 10^3 VLPs μL^{-1} concentration and the lower limit of detection is 10^0 VLP μL^{-1}. The highest resonance shift $\Delta\lambda$ observed at λ_{r1} is smaller (maximum shift of 2 $\pm$ 0.09 nm with 10^3 VLPs μL^{-1}) compared to the λ_{r2} (maximum shift of 3.9 $\pm$ 0.2 nm with 10^3 VLPs μL^{-1}). The sigmoidal fit curve also provides the linear response region of both the resonance shift curves as shown in Fig. 5.4(d) and (e) with a steeper linear resonance shift observed in Fig. 5.4(e) for λ_{r2}. The detection sensitivity obtained from the slope of the curves (from the linear part of the curve) is $S_{r1} = 0.43 \pm 0.06$ nm/decade and $S_{r2} = 1.32 \pm 0.08$ nm/decade for λ_{r1} and λ_{r2} resonance positions, respectively. This experimental observation defines the best detection sensitivity obtained $S = 1.32 \pm 0.08$ nm/decade for the SARS-CoV-2 VLPs with the limit of detection achieved 1 VLP μL^{-1}. From the VLP measurements, we obtain the full width at half maximum (FWHM) is 24.32 nm, and FOM = 0.01 μL^{-1} at the resonance position of λ_{r1}.

To confirm that the linear resonance shift is purely due to the antibody-immobilized SARS-CoV-2 VLPs and not a fluctuation due to the DMEM, we have conducted a test by diluting fresh DMEM (refractive index $n = 1.3370$) solution with PBS (refractive index $n = 1.3348$) and tested on an unfunctionalized device, but no resonance shift was observed either at λ_{r1} or at λ_{r2} (see Appendix Fig. B.5) resonance positions. Specific antibody-SARS-CoV-2 interaction was also authenticated by testing all the above-mentioned VLP concentrations diluted in DMEM on 8 unfunctionalized (no surface activation and antibody were attached) devices fabricated on a separate chip which showed no significant resonance shifts (see the Appendix Fig. B.6). This corrobo-

rates that our proposed functionalized Au nanoresonator array-based device platform can specifically detect SARS-CoV-2 virus-like particles with remarkably lower detection limit. The functionalized technique demonstrates that our proposed device can be used for clinical testing with samples collected from COVID-19 patients. Recent work from our group has reported the detection of clinical samples from COVID-19 patients using the organic electrochemical transistor (OECT) device, and the same biofunctionalization technique was used [149]. We also compared our results with the existing works based on localized surface plasmon resonance biosensor platforms as presented in Table 5.2.

Table 5.2: Comparison of different nanoplasmonic LSPR systems for SARS-CoV-2 detection. Here S defines the detection sensitivity in nm/decade. LOD defines the lower limit of detection.

Nanophotonic systems	Simulation	Beads (100 nm diameter) sensing (experimental)	SARS-CoV-2 sensing (experimental)
Au nanoislands [142]	NA	NA	LOD: 0.22 pM of RdRp SARS-CoV-2 gene sequence
Au nanocups array [62]	NA	NA	LOD: 370 Virus particles mL^{-1}
Toroidal metasurface [143]	NA	NA	LOD 0.42 fM of SARS-CoV-2 spike S1 protein
Au nanoresonators array **(This Work)**	$S = 5.42 \pm 0.82$ nm/decade	$S = 17.05 \pm 3.25$ nm/decade	$S = 1.32 \pm 0.08$ nm/decade and LOD: 1 VLP μL^{-1} of SARS-CoV-2 VLPs

The anti-SARS-CoV-2 spike S1 antibody used in our work also can be used to immobilize other SARS-CoV-2 variants such as Omicron, Delta, etc. It is important to note that this device platform could be used to detect different analytes of 100 nm size with proper functionalization against a particular target analyte, but the design configuration needs to be tuned if the target bioanalyte's size is different. Here, we have used standard nanofabrication techniques for the fabrication of Au nanoresonators, which can be used in scalable production. A small active sensing area (100×100 μm^2) is also advantageous to a full wafer-scale larger number of device production, which will help rapid testing of a high volume of test samples in a single step. The custom optical setup used in this work can be miniaturized further by using an LED of the required wavelength range and a photodiode array detector, which

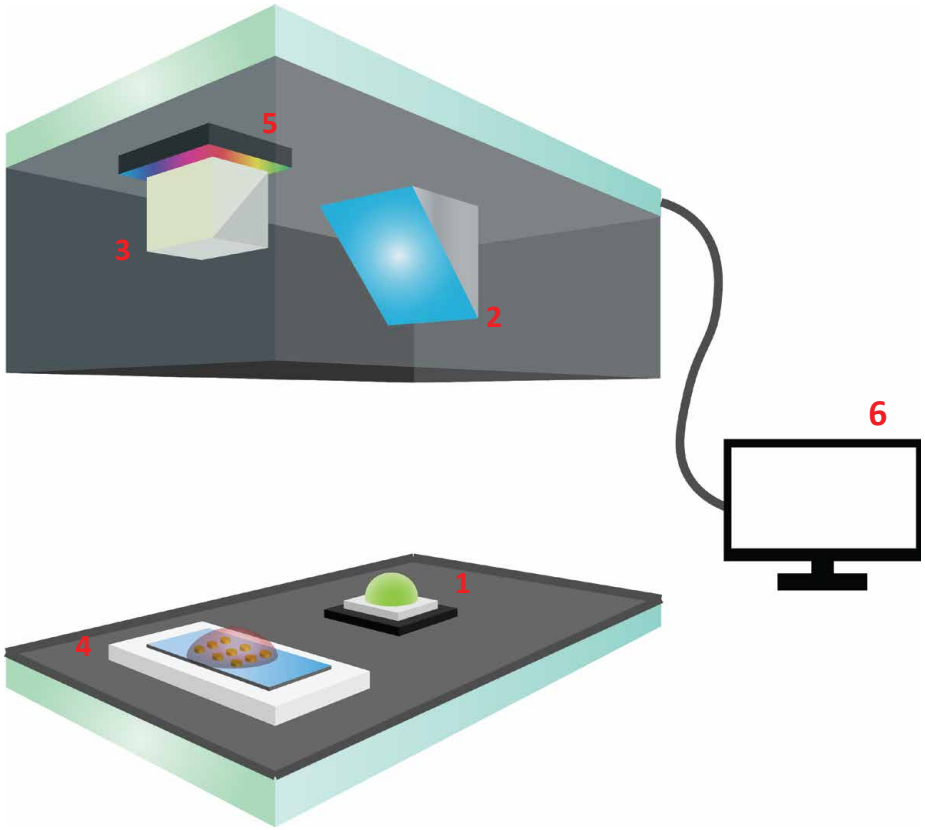

1: LED, , 2: Mirror, 3: Beam splitter (50:50), 4: sample on a holder, 5: photodiode array, 6: Computer for data collection and analysis

Figure 5.5: Schematic image illustrates future the point-of-care device with Au nanoresonators array for SARS-CoV-2 detection.

makes this platform promising for portable applications. A schematic illustration of a prospective point-of-care diagnostic system for SARS-CoV-2 detection is shown in Fig. 5.5, demonstrating the working of the compact nanophotonic diagnostic platform.

5.4 Summary

In this work, we proposed the design of Au nanoresonator array-based SARS-CoV-2 detection platform. Best simulation design parameters were used for fabricating the devices. Devices were first tested with polystyrene beads of 100 nm diameter, and detection sensitivity achieved $S_{beads} = 17.05 \pm 3.25$ nm/decade. We have demonstrated detection of SARS-CoV-2 virus-like particles with the anti-SARS-CoV-2 spike S1 antibody functionalized Au nanoresonator array. We have achieved one of the lowest reported LOD of 1 VLP μL^{-1} solution with the best VLP detection sensitivity S_{VLP} $= 1.32 \pm 0.08$ nm/decade. Also, the required test sample is only 50 μL, which is sufficient for measuring 9 devices, significantly smaller than other works reported. This highlights the importance of proposed technique for ultra-sensitive with low sample volume. Additionally, this plasmonic platform exhibits potential of on-chip large-volume testing of SARS-CoV-2 clinical samples collected from COVID-19 patients. Our proposed platform sketch a direction of a point-of-care nanophotonic biosensor platform for rapid detection of small-size pathogens with ultra-low LOD. Our future plan is to miniaturize this measurement setup, as demonstrated in the previous section and conduct a large volume of clinical samples collected from COVID-19 patients to establish this technique for future generation lab-on-a-chip technology. In the next chapter, we have proposed different metasurface-based geometry based on MoS_2, a novel quantum material to detect 100 nm-sized particles.

Chapter 6

Designs of Leaky MoS_2 Nanoresonaotrs for Small Size Bioanalytes Detection

6.1 Introduction

In previous chapters, we have delved into biosensing platforms based on plasmonic Au and MIM nanoresonators. We have demonstrated that the Au nanoresonator array device boasts the capability to detect SARS-CoV-2, with a detection limit as low as a single virus-like particle. However, the major disadvantages of plasmonic systems are: (a) plasmonic nanostructures suffer from material absorption losses, (b) exponential decay of resonance field in air makes it tough to get good overlap with the target analytes, (c) energy dissipation into heat, which can denature the biomolecules and proteins. On the other hand, high refractive index dielectric or, semiconductor nanostructures offer a promising alternative for sub-wavelength localization of light through Mie resonances [76]. Dielectric/semiconductor resonant nanophotonics is an emerging research field with applications ranging from biosensing [150], topological nanophotonics [151–153], and nonlinear photonics [154], metalens and imaging [155, 156], and quantum photonics [157–160]. Unlike metallic structures, dielectric nanoresonators can support electric and magnetic Mie modes, making them more versatile for different applications [161].

The major advantage of dielectric/semiconductor nanostructures is: (i) the resonant characteristics of light in high-index dielectric/semiconductor nanostructures can replicate sub-wavelength effects in plasmonics without energy dissipation into heat, (ii) high refractive index dielectric/semiconductor nanoresonators are available for various applications across a wide wavelength range from visible to NIR depending on the materials and geometry chosen, (iii) confinement of electromagnetic fields within the dielectric/semiconductor structures results in high Q factors of subwavelength nanoresonators. Careful design of meta-atoms (i.e., single nanostructure) and arrangements to periodic arrays can suppress radiative decay and enhance field confinement, leading to the formation of high-Q resonances. However, the strong electric hotspot generated due to the Mie resonance is located inside each nanoresonator, making it difficult to access biomolecules attached to the outer surface. This creates a great challenge for biosensing applications as target bioanalytes cannot easily overlap with the resonance field, impacting the sensing performances. To solve this problem, a leaky dielectric/semiconductor nanoresonator design is mandatory to allow easier access to the resonance field for biosensing and achieving high sensitivity. Transition metal dichalcogenide (TMDC) materials have drawn great attraction from researchers, material scientists, and engineers due to their unique optoelectronic properties [162]. The key property of these materials is: a single atomic layer shows direct bandgap and changes to indirect bandgap in the bulk (thickness above 5 nm). A few works have reported that bulk TMDCs are also useful for different applications [163–166]. A noteworthy optical property of TMDCs, they possess a very high refractive index ($n > 4$) and low absorption coefficient ($k < 1$) [167] at the single atomic layer thickness as well as bulk material in the visible and near-infrared (NIR) wavelength range. Because of their high refractive index with lower absorption losses at higher spectral wavelengths, low-loss optical waveguides and different nanophotonic structures can be fabricated using various TMDCs [168–170]. Although metasurface and Mie resonances have been well studied in several high-index dielectric and

semiconductor materials (e.g., TiO_2, Si, GaAs, GaN, etc.), 2D layered TMDCs are a recent addition to this area of research. The primary reasons for using different multilayer TMDC materials highlighted in the existing works are: (i) multilayer TMDCs possess large exciton oscillator strength [171] and high-refractive index ($n > 4$) support strong confinement of waveguide mode, (ii) low extinction coefficient ($k \approx 1$) manifests low loss of waveguide transport [172], (iii) multilayer TMDCs have optical anisotropy (in-plane and out-of-plane) [168], which helps to confine in-plane and out-of-plane waveguide modes [170], (iv) Multilayer (bulk) TMDC materials support optical resonant Mie modes, which can not occur at atomically thin monolayer due to their limited thickness [173, 174].

The field of metaphotonics using multilayer TMDCs is new and raising interest to many researchers. However, there are no reports found of multilayer TMDC metasurface-based platforms for small-size bioanalyte sensing applications. Here, we propose three different configurations of bulk MoS_2 based metasurface for detection of 100 nm size bioanalytes. MoS_2 as nanoresonator's material was used because of its high refractive index and low absorption loss in the visible and NIR wavelength and has been proven to have low cytotoxicity and genotoxicity [175, 176]. Also, many biosensing platforms have been reported with MoS_2 signifies biocompatibility [177–179]. We have performed finite difference time domain (FDTD) simulations to design and study 100 nm sized bioanalytes sensing.

6.2 Simulation Methods

The design optimization of the MoS_2 metasurface was conducted by finite difference time domain (FDTD) simulations using the FDTD solution software package (Ansys Inc. [108]). We have used periodic boundary conditions both in X and Y directions, and perfectly matched layer (PML) in Z direction. The mesh size used was 5 nm^3. A broadband (λ = 400 – 2000 nm) plane-wave source incident on the top of the MoS_2 metasurface and the 2D monitor was placed above the plane wave source position to

record the reflection spectrum. We have collected the reflection spectrum by using both the TE (s-polarized) and TM (p-polarized) polarized plane wave sources separately, and they are identical (see Fig. 6.1). The spectrum was recorded with the TM-polarized (p-polarized) plane wave source is presented in the following sections to analyze the MoS_2 metasurfaces' sensing performances. Resonance shifts from the simulated spectra were analyzed in Origin and MATLAB.

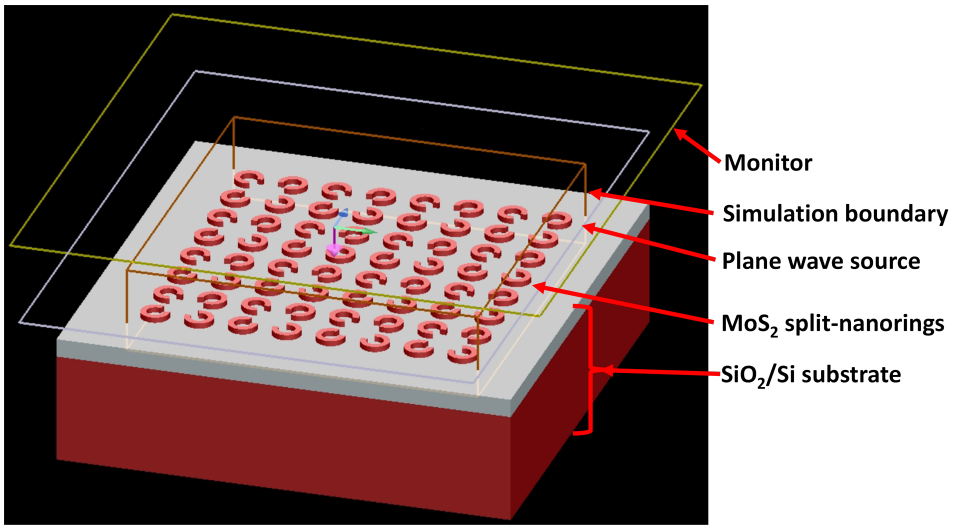

Figure 6.1: Finite difference time domain (FDTD) simulation setup with the MoS_2 split-nanorings array is portrayed. A broadband plane wave source is placed on the top of the nanoresonators array, and a 2D field monitor is placed behind the source plane to collect the reflection spectrum from the array. The same setup was also used for simulating other MoS_2 metasurface configurations.

6.3 Design and Working of MoS_2 Nanoresonators

According to the Mie theory [180, 181], resonance occurs when the wavelength of light inside the nanostructure becomes comparable to its size: $2R \approx \frac{\lambda}{n}$, where n is the refractive index of nanostructure's material, R is the nanostructure's radius, and λ is the wavelength of light [182, 183]. The Mie resonance modes depend on the geometry, size, and refractive index of constituent materials. To achieve the resonance to occur in the visible to NIR wavelength range, the nanostructure's material needs to have a high refractive index (n) [76]. Multipolar resonances (such as electric dipole

(ED), magnetic dipole (MD), electric quadrupole (EQ), and magnetic quadrupole (MQ) resonance modes, etc.) are generated due to the interaction of electric and magnetic fields inside the nanoresonator. The spectral position and resonance modes can be controlled by manipulating the size, shape, pitch (the gap between two adjacent nanoresonators), nanoresonator's material, and lattice arrangement. In this work, two different meta-atom structures are explored: (i) split-nanoring and (ii) equilateral nanotriangle of bulk MoS_2 as the fundamental building block to construct the three different metasurface designs: (i) configuration 1: cross-facing MoS_2 split-nanorings (Fig. 6.2 (a)), (ii) configuration 2: MoS_2 split-nanorings chain-like array (Fig. 6.2 (b)) and, (iii) configuration 3: MoS_2 equilateral triangles facing each other 6.2 (c)). In the rest of the parts of this chapter, we refer to them as configuration 1, configuration 2, and configuration 3, respectively. A schematic of finite difference

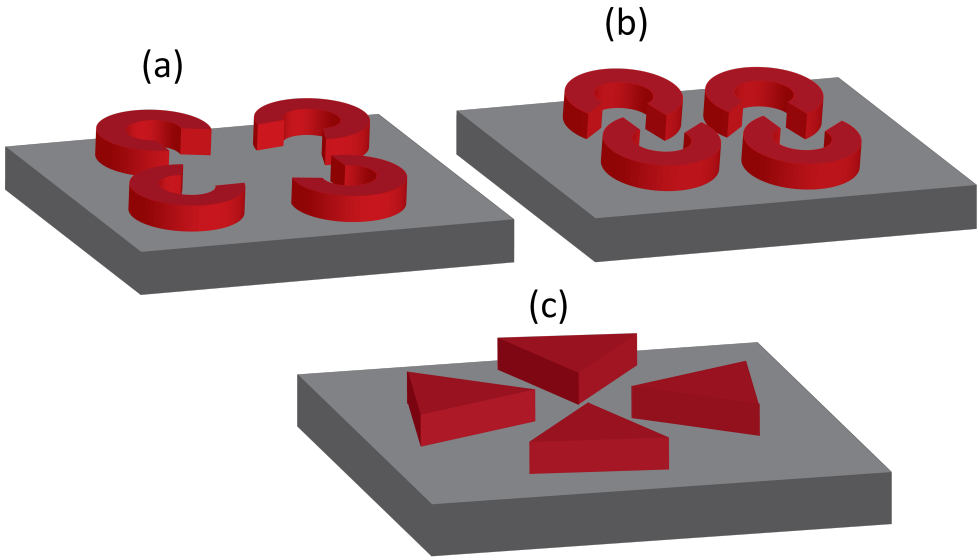

Figure 6.2: MoS_2 metasurface unit-cell configurations: (a) configuration 1: unit-cell consists of 4 MoS_2 split-nanoring resonators are cross-faced, (b) configuration 2: unit-cell made of a chain-like structure of MoS_2 split-nanorings, and (c) configuration 3: unit-cell constructed with the four cross-faced MoS_2 equilateral triangles. All three unit-cell configurations formed a 2D array on SiO_2/Si substrate for conducting the detection performance with polystyrene particles.

time domain (FDTD) simulation setup is shown in Fig. 6.1(a), and the details of the

simulation are discussed in Section 6.2. The MoS_2 metasurface properties and field confinement can be tuned by varying all of the following parameters. For the split-nanorings-based sensor designs (shown in Fig. 6.2(a) and (b)), we have varied the design parameters of each configuration: inner diameter (D_{in}), outer diameter (D_{out}), split-gap (s), the gap (G) between two adjacent nanorings and height ($H_{nanoring}$). In the case of the equilateral nanotraingles array (in Fig. 6.2 (c)), the cross-facing gap among all the four nanotriangles corners in one unit-cell and the height of naotriangles ($H_{triangle}$) were varied to optimize the sensor's performance.

We have analyzed the device performance with polystyrene particles of 100 nm diameter distributed over the device surface. Here, we have chosen polystyrene as the material because the refractive index matches well with most of the bioanalytes and the size (100 nm) matches the dimension of SARS-CoV-2 and Influenza H1N1 virus. To achieve the controlled leaky nature of each MoS_2 nanoring resonator, we have proposed symmetry breaking MoS_2 split-nanoring design. The split gap manifests a balance between the leaky nature and resonator confinement of individual MoS_2 nanoring. The leaky field and cross-coupling between adjacent split-nanorings in one unit-cell are shown in Fig. 6.3 (a) and (b) illustrating the top-view (XY view) of configuration 1 and configuration 2, respectively. The arc opening of each nanoring defines the split-gap, which brings the resonance field out to the surface so that, uniform and high surface sensitivity throughout the device surface can be achieved. The electric dipole mode field is confined in the high-index MoS_2 ring's nano-loop. Split-gap broke the symmetry of nanoring, effectively controlling individual MoS_2 nanoring's E-field leakage, which is evident in the side-view E-field distribution of split-nanoring configurations as shown in Fig. 6.3(d) and (e). Thereby, the leaky resonance field is localized on the surrounding surface and hollow spaces in the MoS_2 split-nanoring resonators. For biosensing applications, target bioanalytes are attached to the surface and the disturbance of the resonance field induces a resonance shift, which is transduced as the sensor performance.

For the nanotriangle-based sensor design, the gap among four cross-facing nano-

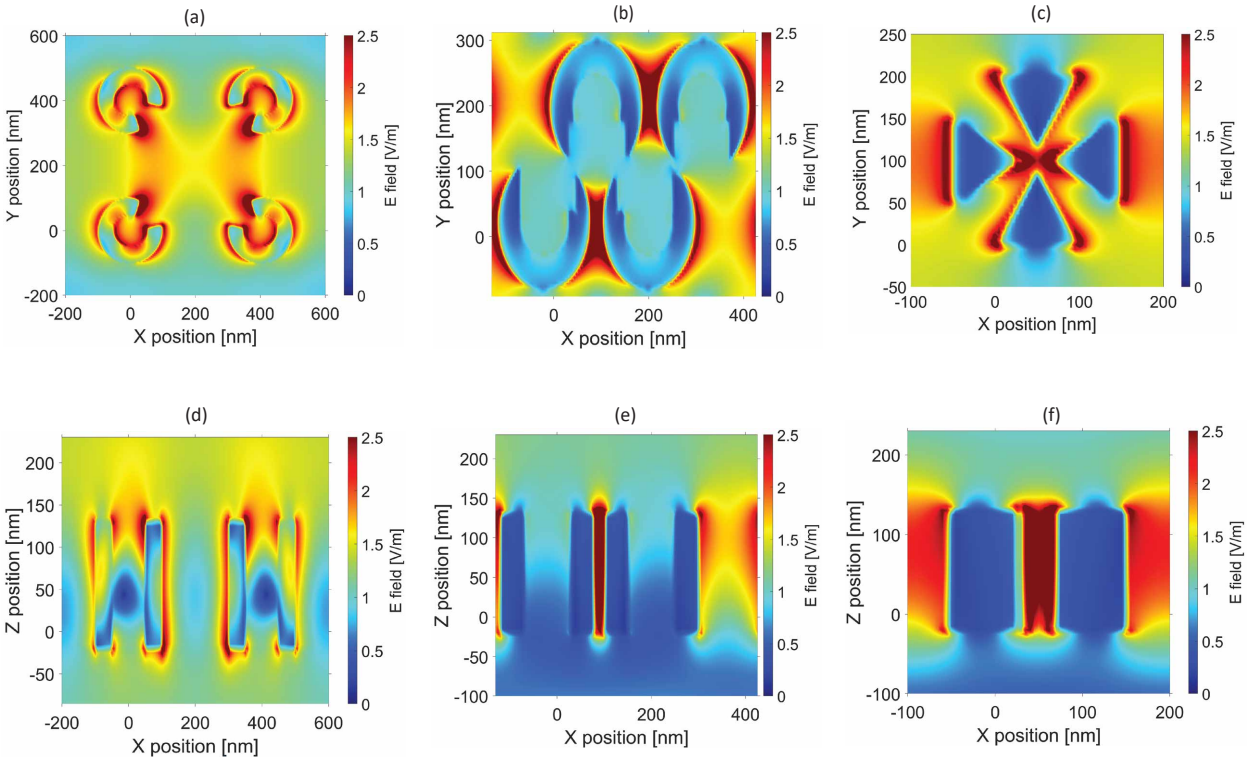

Figure 6.3: E field distribution of unit-cell configurations: (a) top-view shows E field distribution on cross-faced MoS_2 split-nanorings (configuration 1), (b) top-view shows E field distribution on chain-like MoS_2 split-nanorings (configuration 2), (c) top-view shows E field distribution on MoS_2 equilateral triangles (configuration 3). Figures (d), (e), and (f) depicts the side-view (XZ view) collected by a 2D XZ monitor placed parallel to X-axis to record the E field distributions of leaky nanoresonator's sidewall as well as in the hollow space. Both top-view and side-view E field distributions for configuration 1, configuration 2, and configuration 3 were collected at $\lambda = 831.5$ nm, $\lambda = 1348.6$ nm, and $\lambda = 1158$ nm, respectively. For all these figures, the plane wave source was TM (p-polarization) polarized.

triangles, and the height of MoS_2 nanotriangle were varied to get optimum sensor performance. Here, we have chosen 100 nm as the side length of each MoS_2 equilateral triangle, so that each nanotriangle's surface overlaps with the target analyte of 100 nm diameter. The goal was to obtain high resonance field enhancement on the device surface and stronger overlap with the analytes on the surface to obtain higher surface sensitivity. Fig. 6.3 (c) and (f) represent the top (XY) and side-view (XZ) of E-field distributions of MoS_2 nanotriangle metasurface unit-cell. Intense and lo-

calized near-fields create a E-field hotspot present in the gap of MoS_2 nanotriangles. Fig. 6.4 (a), (b), and (c) illustrates the resonance E field distribution throughout the top surface of the proposed three configurations.

In the following section 6.4, simulated sensing performances are analyzed for all

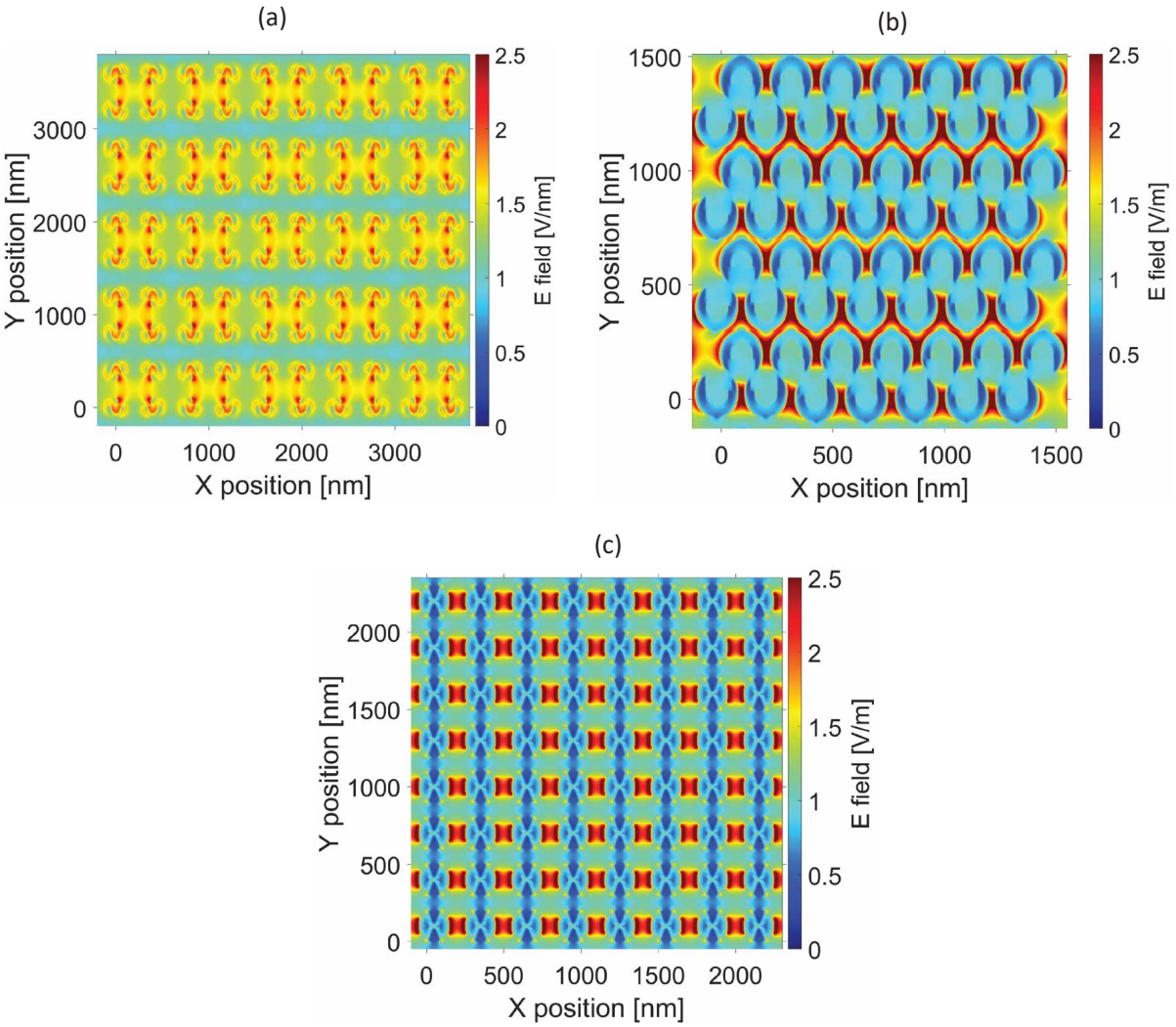

Figure 6.4: Resonance electric field distributions for different configurations: (a) The top-view E field of 2D array of MoS_2 split-nanorings array (configuration 1) recorded at $\lambda = 831.5$ nm, (b) top-view of chain-like MoS_2 split-nanorings array (configuration 2) collected at $\lambda = 1348.6$ nm, and (c) top-view of MoS_2 equilateral nano triangles array (configuration 3) at $\lambda = 1158$ nm.

three MoS_2 metasurface configurations.

6.4 Results and Discussions

We have carried out simulations with the TE (s-polarize) and TM polarized (p-polarize) plane wave source separately to check the device's polarization-sensitive behavior. Figures 6.5 (a), (b), and (c) depict the reflection spectra collected (without any particles on it) for three MoS_2 metasurface configurations with the TE and TM polarization conditions. It can be observed that reflection spectra are exactly similar for both configuration 1 (Fig. 6.5 (a)) and configuration 3 (Fig. 6.5 (c)), making them polarization-insensitive metasurfaces. Therefore, an unpolarized light source can measure these devices, which reduces optical components in the setup. However, resonance dip positions for the spectra obtained from the MoS_2 split-nanorings chain-like structure (configuration 2) are fairly similar for the TE and TM polarizations, although they do not overlap exactly. In the rest of this chapter, we have analyzed detection sensitivity with TM polarized source only to compare all of their sensing performances.

For biosensing applications, the resonance field should be accessible on the top surface to achieve larger field overlap and stronger interaction with the bioanalytes for high detection sensitivity. Here, we have chosen the inner diameter of each nanoring such that the inner hollow space matches well with the target bioanalyte's size to be detected to ensure a larger overlap with the leaky resonance field. Stronger overlap and interaction of the leaky resonance field with the target bioanalytes such as the SARS-CoV-2 virus, and H1N1 virus, outcomes a higher detection sensitivity.

We have performed a reflection simulation with varying polystyrene particles (1 to 1000 particles each of 100 nm diameter) distributed (Gaussian distribution) over the MoS_2 metasurface configurations separately to analyze the sensing performances. In this work, we have used 100 nm diameter polystyrene particles because the refractive index of polystyrene matches with the bioanalytes and 100 nm size matches the size

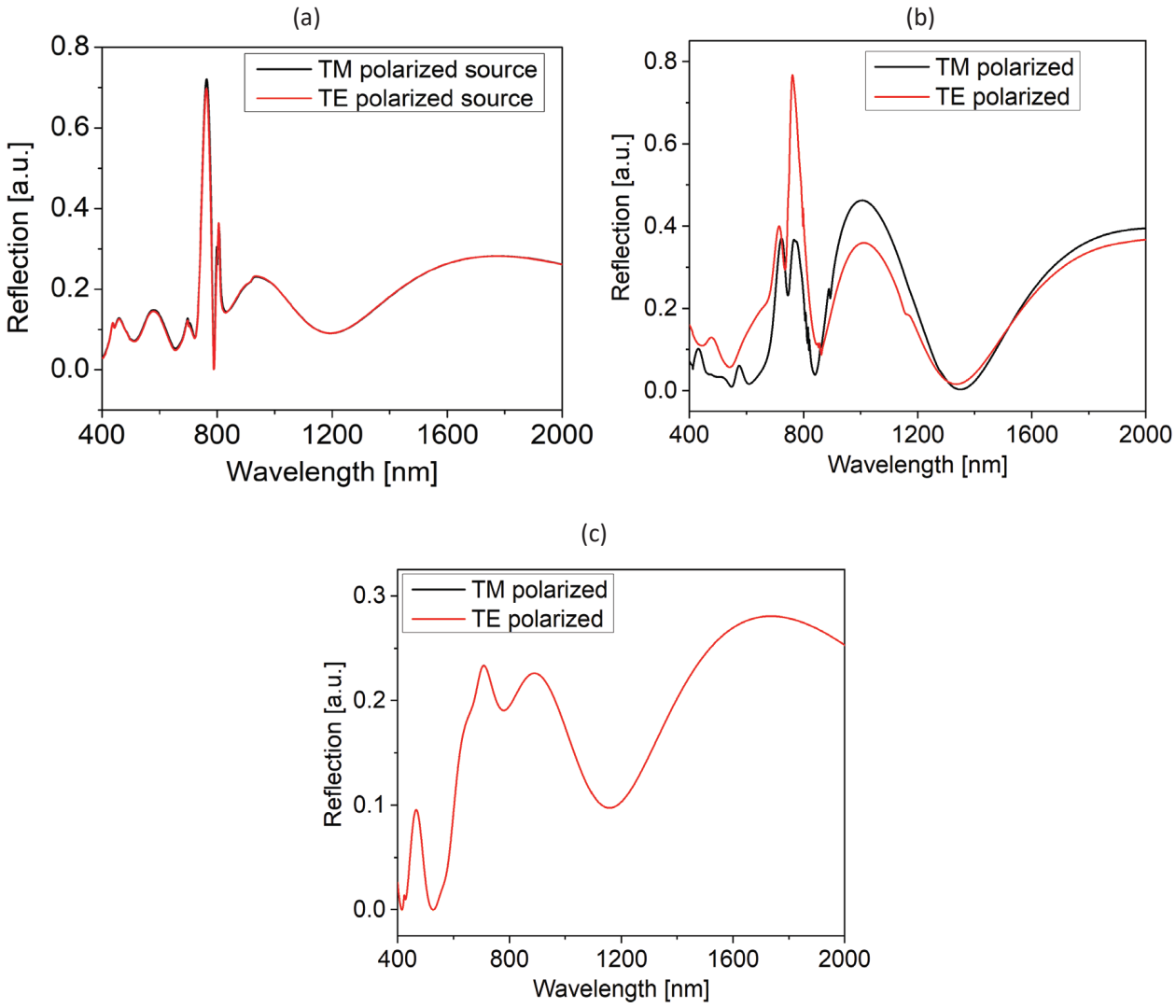

Figure 6.5: Reflection spectra recorded both with TE (s) and TM (p) polarization sources for the device configurations (a) cross-facing split-nanorings array (configuration 1), (b) split-nanorings chain-like array (configuration 2), and (c) nanotriangles array (configuration 3).

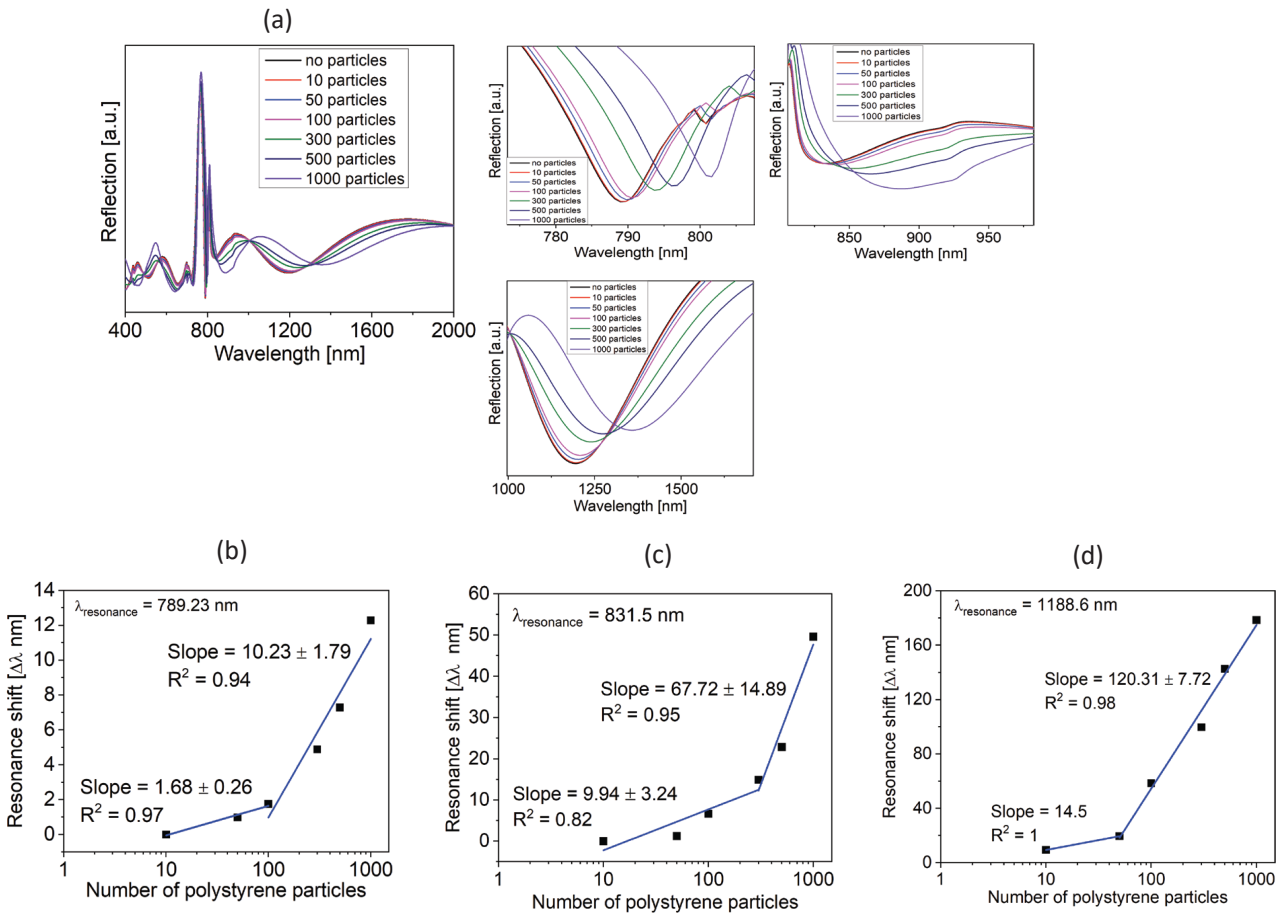

Figure 6.6: Reflection spectra of MoS_2 split-nanorings array (configuration 1): (a) The reflection spectra with varying numbers of polystyrene particles, whereas, the inset images show the enlarged view of resonance dip locations to view the wavelength shift with the particle number increases. Figures (b), (c), and (d) demonstrate the piece-wise linear response of resonance shift versus the number of polystyrene particles at resonance wavelength locations $\lambda_{resonance}$ = 789.23 nm, 831.5 nm, and 1188.6 nm, respectively. The slope of linear response demonstrates the detection sensitivity. Here, the dimensions used for simulation: inner diameter D_{in} = 100 nm, outer diameter D_{out} = 200 nm, split-gap (s) = 50 nm, gap between two adjacent split-nanorings (G) = 200 nm and thickness of MoS_2 = 150 nm. For all these plots, the plane wave source was TM (p-polarization) polarized.

of these viruses [184]. The reflection spectra shown in Fig. 6.6 (a) for configuration 1, and the inset images show the enlarged view of the resonance wavelength locations. There are multiple resonance dip locations in the reflection spectra that define the cross-coupling effects of adjacent MoS_2 meta-atoms (such as coupling between two adjacent split-nanorings as seen in Fig. 6.3). The resonance wavelength red-shifted with the increase in number of polystyrene particles representing the piece-wise linear response curves ((see Fig. 6.6 (b), (c), and (d))). The slopes obtained from the resonance shift curves signify the detection sensitivity. The best detection sensitivity obtained is 14.5 nm/decade for the 10 to 50 particles range and 120.31 $\pm$ 7.72 nm/decade (at $\lambda_{resonance}$ = 1188.6 nm) for the 50 to 1000 particles range. It can be observed that the sensitivity is higher at the higher number density range (50 to 1000 particles range). The reason is the higher number density of polystyrene particles on the device surface increases the effective local refractive index of the surrounding environment, and this reduces the restoring force of the resonance electric field, lowering the energy (frequency), hence red-shift occurs at the resonance wavelength peak. The minimum number of particles (limit of detection (LOD)) can be detected by using this MoS_2 split-nanoring metasurface (configuration 1) - 10 particles. We have

Table 6.1: Summary of sensitivity obtained from different design parameters of MoS_2 split-nanorings array metasurface (configuration 1)

Inner diameter (D_{in} nm)	Outer diameter (D_{out} nm)	Split-gap (s nm)	Gap (G nm)	Height (H nm)	Sensitivity (nm/decade) λ_r = 400 - 900 nm range	Sensitivity (nm/decade) λ_r = 900 - 2000 nm range
100	200	50	100	150	7.67	193.17
100	200	50	200	150	67.72	120.31
100	200	50	200	10	36.69	80.30
100	200	50	200	5	38.48	86.02
100	200	50	100	2.1 (3 ML)	36.7	41.93
100	200	50	200	2.1 (3 ML)	31.5	60.57
100	200	50	100	1.3 (2 ML)	39.01	74.27
100	200	50	200	1.3 (2 ML)	77.8	58.64
100	200	50	100	0.65 (1 ML)	NA	NA
100	200	50	200	0.65 (1 ML)	NA	NA

summarized the sensing performance parameters in Table 6.1 for varying dimensions of MoS_2 metasurface configuration 1. It is visible that, the sensitivity (of 100 nm-

sized polystyrene particle detection) is enhanced by increasing the height of individual MoS_2 split-nanorings and reducing the gap between two adjacent split-nanorings. Reducing the thickness of MoS_2 to monolayer (1 ML) $\approx$ 0.65 nm, bilayer (2 ML) $\approx$ 1.3 nm, and trilayer (3 ML) $\approx$ 2.1 nm, impose restrictions along the height axis (Z) directions to support the resonant Mie modes at visible or NIR range [171, 173, 174]. Reduction of the gap between two neighboring MoS_2 split-nanorings, strengthens the coupling of the resonance field and thereby enhances the resonance field distribution over the device surface.

We choose the split-nanorings dimensions: D_{in} = 100, D_{out} = 200, split-gap (s) = 50 nm, height (H) = 150 nm and varying the gap-between two rings (G) to study further the MoS_2 split-nanorings chain-like array (configuration 2). Reflection simulations were performed by varying the number of polystyrene particles as shown in Fig. 6.7 (a). Although there are multiple resonance dip locations, there are no consistent shifts in resonance wavelength except at $\lambda = 1348.6$ nm (see the inset image of Fig. 6.7(a)). Fig. 6.7(b)) illustrates the linear response of the resonance shift curve with the increase in the number of polystyrene particles (of 100 nm diameter). The best detection sensitivity obtained with this metasurface (configuration 2) is 102.07 $\pm$ 8.7 nm/decade and the LOD is 50 particles. Table 6.2 summarizes the detection sensitivity of metasurface configuration 2 with varying dimensions.

Comparing both the MoS_2 split-nanorings-based configurations 1 and 2 (from Table 6.1 and Table 6.2), it is observed that the cross-facing MoS_2 split-nanorings array (configurations 1) demonstrated better sensing performance both at the shorter wavelength range (λ = 400 - 900 nm) and longer wavelength range (λ = 900 - 2000 nm range) compared to the metasurface configuration 2. This gives the flexibility to choose this metasurface design for the practical use of biosensors in a particular range of wavelengths (either visible or, NIR). It is noteworthy that LOD for 100 nm size polystyrene particle detection is also lower (10 particles) with metasurface configuration 1 compared to configuration 2 (50 particles). This highlights the significance of

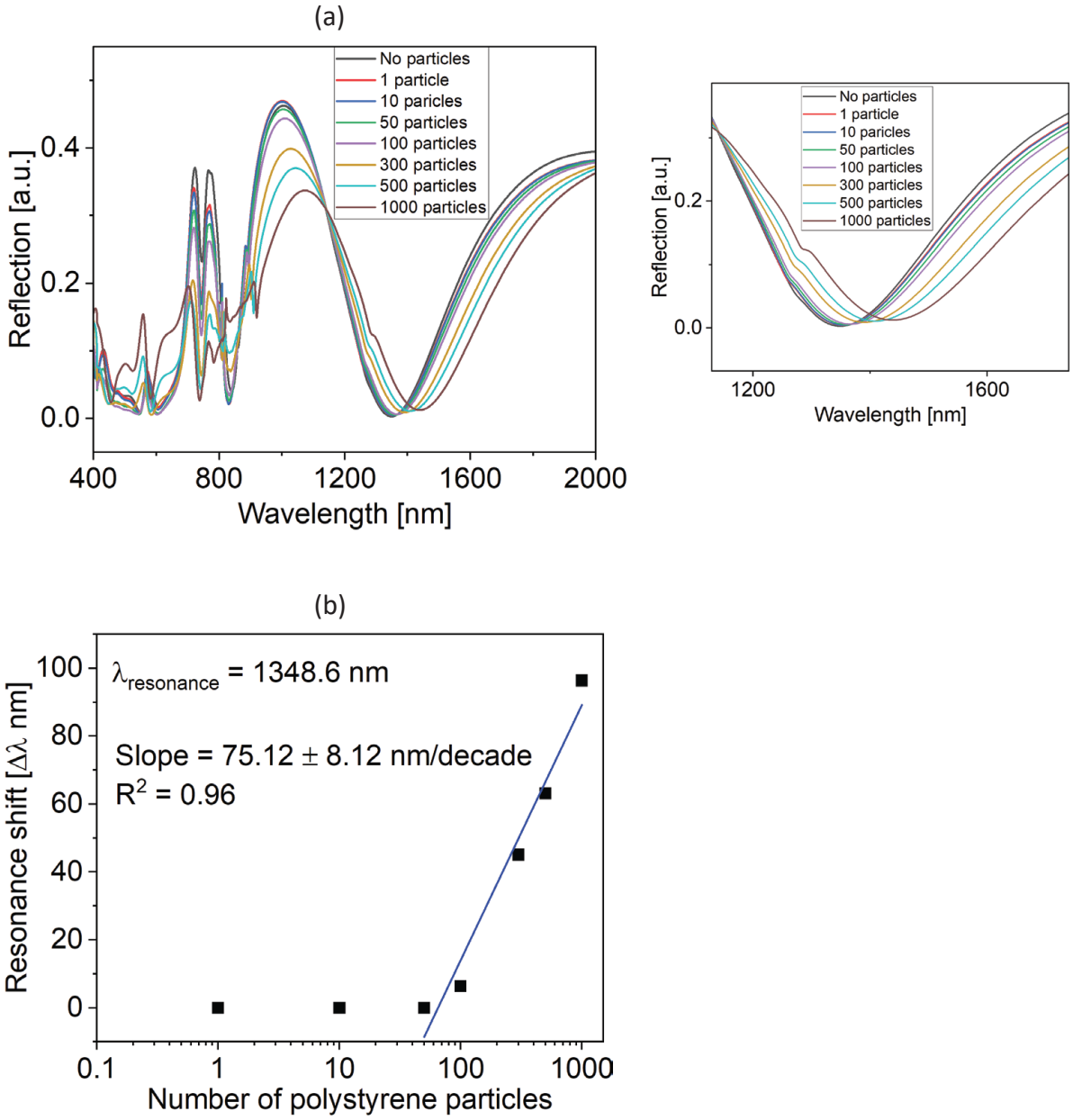

Figure 6.7: (a) Reflection spectra collected from MoS_2 split-nanorings chain-like array (configuration 2: D_{in} = 100 nm, D_{out} = 200 nm, split-gap = 50 nm, gap between two adjacent split-nanorings (G) = 20 nm) with the numbers of polystyrene particles, and the inset image show the zoomed-in view of resonance dip location. Fig. (b) shows the linear response of resonance shift (λ = 1348.6 nm) with the number of particles. The resonance dips within the 400 - 900 nm range do not show a clear shift. TM (p-polarization) polarized plane wave source was used for this study.

the proposed MoS_2 split-nanorings metasurface configurations in small-sized bioanalytes sensing applications.

Table 6.2: Summary of sensitivity obtained from different design parameters of MoS_2 split-nanorings chain-like array metasurface (configuration 2).

Inner diameter (D_{in} nm)	Outer diameter (D_{out} nm)	Split-gap (s nm)	Gap (G nm)	Height (H nm)	Sensitivity (nm/decade) λ_r = 400 - 900 nm range	Sensitivity (nm/decade) λ_r = 900 - 2000 nm range
100	200	50	20	150	NA	75.12
100	200	50	50	150	NA	102.07

Further, we also have performed simulations (see reflection spectra in Fig. 6.8 (a)) with MoS_2 equilateral nanotriangle array metasurface (configuration 3). Each side length of the equilateral triangle was chosen to be 100 nm, the gap between two neighboring unit cells was 100 nm, and the gap between corners of two face-to-face triangles was chosen to be 30 nm to obtain enhanced coupling of resonance E field in the gap between four nanotriangles as seen in Fig. 6.3 (c) and (f). The linear response of the resonance shift curves with the number of particles is presented in Fig. 6.8 (b) and (c) for the visible and NIR spectral range, respectively. It is visible that sensitivity is higher (19.65 ± 9.06 for the 10 - 100 particles and 305.31 ± 29.24 for the 200 - 1000 particles) at the NIR spectral range (Fig. 6.8 (c)) and the LOD achieved 10 particles. Increasing the gap between two face-to-face nanotriangle corners does not show a consistent red-shift in resonance wavelength.

In practical application, a silicon photodiode array sensor is convenient to use. Therefore, we only focus on the biosensor's response at the 400 - 900 nm wavelength range. The best detection sensitivity obtained in the range of 400 to 900 nm with MoS_2 split-nanorings array (configuration 1) is 67.72 ± 14.89 nm/decade at $\lambda_{resonance} = 831.5$ nm. The resonance line width (FWHM) is 54.21 nm, and the Q-factor = 15.33. On the contrary, the MoS_2 split-nanorings array (configuration 2) does not show a significant resonance shift in the wavelength range of 400 to 900 nm. However, in the

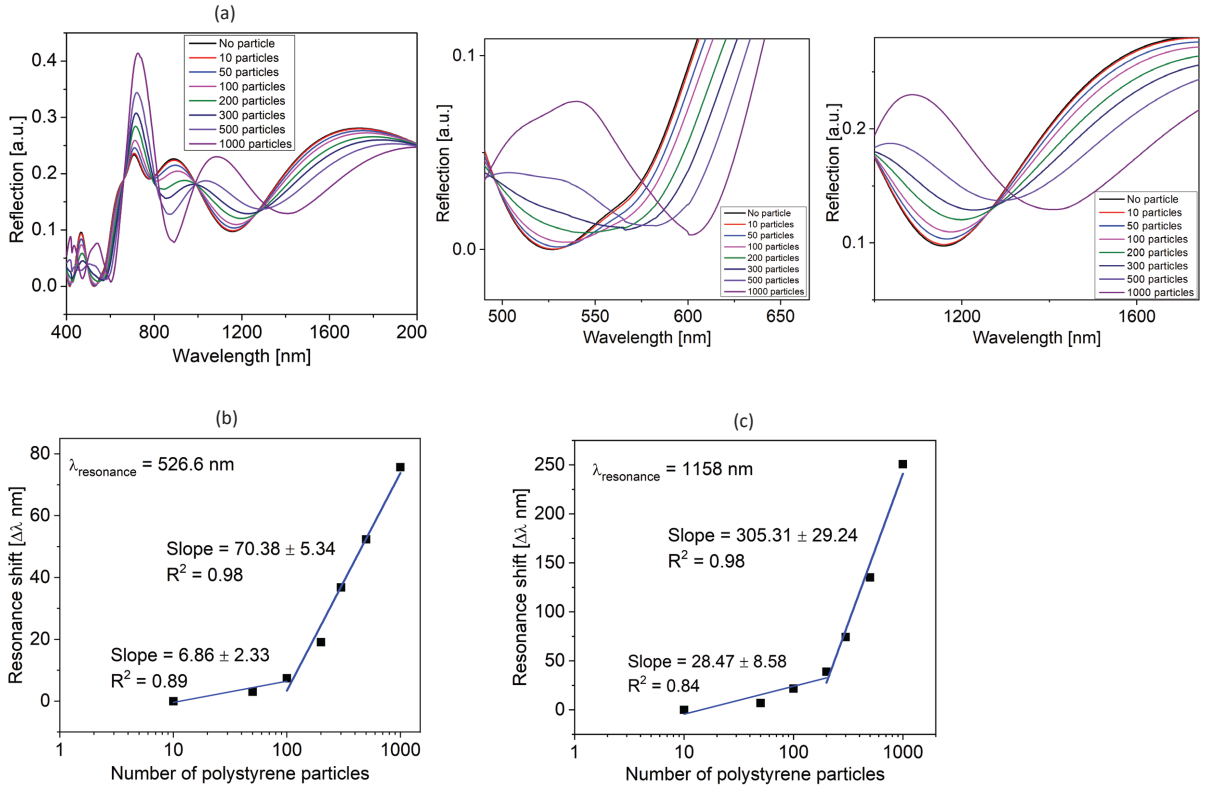

Figure 6.8: Fig. (a) shows the reflection spectra for the MoS_2 equilateral nanotriangles array (configuration 3: each side length of 100 nm and the gap between two face-to-face corners is 30 nm), and the inset images display the resonance wavelength position shifts with the number of particles. Figures (b) and (c) represent resonance shift curves at the resonance wavelength $\lambda = 526.6$ nm and $\lambda = 1158$ nm, respectively. TM polarized plane wave source was used to simulate this configuration.

case of MoS_2 nanotriangles array (configuration 3), we obtain a sensitivity of 70.38 $\pm$ 5.34 at $\lambda_{resonance}$ = 526.6 nm, and the resonance line width of 88.66 nm provides Q-factor = 5.93.

6.5 Summary

In this chapter, we have proposed novel MoS_2 metasurface configurations for small-size bioanalytes sensing applications. We have analyzed 100 nm size polystyrene particle detection sensitivity and compared the sensing performances of three MoS_2 metasurface configurations. The best design configuration is the MoS_2 nanotriangle array metasurface (configuration 3) with a sensitivity of 305.31 $\pm$ 29.24. However, fabricating equilateral triangle structures with 100 nm side length could be challenging such as the corners of triangles could become rounded. Also, fabricating the MoS_2 split-nanoring chain-like array (configuration 2) is challenging because achieving fabrication resolution, such as a small gap between two adjacent split-nanorings, could be difficult. Based on our analysis, we have selected the cross-facing MoS_2 split-nanoring metasurface (configuration 1) for further experimental studies and fabrication. This configuration displays sensing abilities across a wide range of wavelengths, making it an ideal candidate for implementing a biosensing platform with the desired wavelength. The following chapter will showcase the experimental studies with PLD-grown MoS_2 thin films that are highly crystalline and uniform across a large area. We will also describe the fabrication process of the MoS_2 split-nanoring metasurface and present our findings from testing it with polystyrene beads.

Chapter 7

Leaky MoS_2 Nanoresonaotrs for Small Size Analytes Detection

7.1 Introduction

In the last chapter 6, we have discussed different metasurface configurations and their working mechanisms. This chapter focuses on the fabrication and experimental studies of the proposed leaky MoS_2 split-nanoring resonators for biosensing applications. We have used the best design parameters obtained from Finite Difference Time Domain (FDTD) simulations in the previous chapter 6. Experimental studies of dielectric metasurface-based biosensing and refractive-index sensing platforms have recently been reported. Y. Jahani et al., [185] describes a new imaging technique that can detect extracellular vesicles, including exosomes, in real-time for the diagnosis of breast cancer with a limit of detection (LOD) down to 204 fM solution. The dielectric metasurface was constructed by amorphous silicon nanostructures (a single unit cell combines a circular and an elliptic disk). A. Tittl et al., [186] proposed a high Q factor metasurface based on a two-dimensional array of Si ellipse structures for molecular fingerprint (protein A/G) detection. They have conducted molecular composition analysis of a complex bioassay by metasurface-based imaging. O. Yavas et al., [73] proposed Si nanoresonator array combined with advanced microfluidics to detect cancer protein markers (specifically, prostate-specific antigen or PSA) in human blood serum with LOD of 0.69 ng/mL that allows for early detection of cancer.

Nanopatterning and developing Mie resonator-based metasurface with different transition-metal dichalcogenide (TMDC) materials (such as MoS_2, WS_2, $MoSe_2$, etc) have not been studied well. The research area of 2D materials-based nanophotonics is growing fast due to the ability to design diverse nanophotonic systems. Nanoresonators made with multilayer TMDCs could enhance the optical properties of these materials and emerge different optical phenomena (such as optical emission and confinement, enhanced scattering, strong excitonic light-matter interaction [187, 188], optical anisotropy [189], and different Mie resonance modes [171, 190]), build a strong foundation for metasurface biosensors. In recent years, a few experimental studies have demonstrated Mie-like resonances with the TMDCs as nanoresonator material. V. E. Babicheva [191] studied lattice resonances with periodic arrays of WS_2 nanoantennas for efficient light control at the nanoscale dimension. P. G. Zotev et al., [169] proposed hexagonal shape WS_2 nanoantennas to enhance the photoluminescence (PL) (by the factor of 240) of monolayer WSe_2 integrated on top of WS_2 Mie resonators. A. V. Prokhorov et al., [192] theoretically demonstrated a MoS_2 metasurface consisting of 2D nanodisks array with a hole in it, and introduced the quasi-trapped mode (QTM) resonance. They have demonstrated strong near-field enhancement, leading to a narrowband absorption around the telecom wavelength (λ = 1550 nm), which can be used for polarization-sensitive sensors and meta-coatings on several optical components. In another recent study by F. Shen et al., [171], 1D gratings and 2D nanodisk array metasurface made of bulk MoS_2 (thickness 110 $\pm$ 10 nm) are fabricated and they have studied the interactions of Mie resonance modes (magnetic surface lattice resonances) with the excitons of MoS_2, which could open new directions to TMDC metaphotonics. B. Munkhbat et al., [193] fabricated different nanophotonic structures (2D nanoholes array, nanodisk array, 2D photonic crystal, and waveguide-coupled microring resonators) with bulk WS_2 showed a roadmap to TMDC nanophotonics for light confinement, narrowband absorption, and waveguide applications.

The existing literature does not show any work of 2D TMDC Mie resonator-based

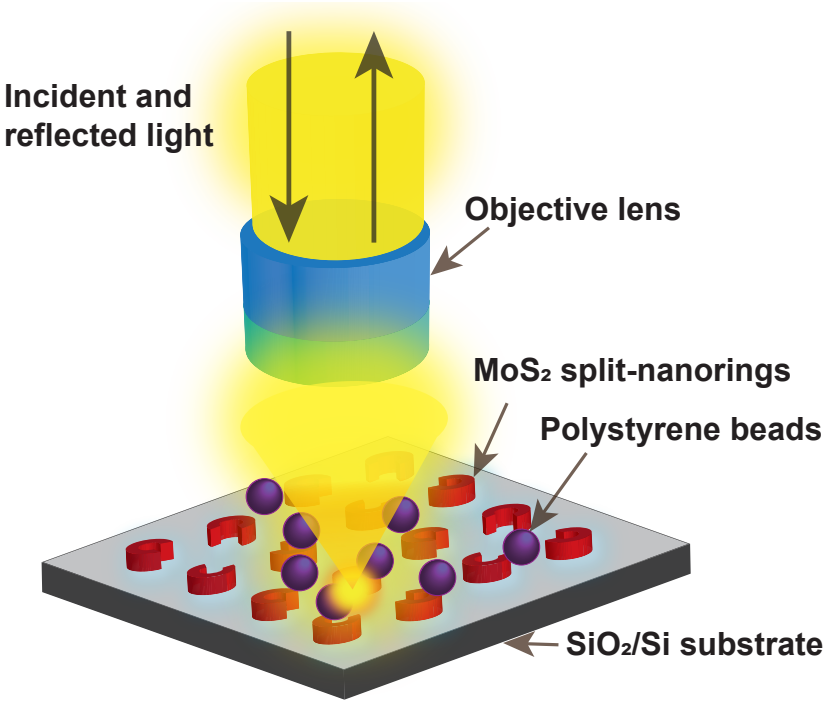

Figure 7.1: Schematic illustration of MoS_2 split-nanorings array for 100 nm sized polystyrene beads detection.

platform for biosensing applications. The major reason is the challenges of getting a larger area of high-quality uniform thin films of TMDC materials, which can be processed further with standard nanofabrication techniques. This chapter demonstrated the fabrication process and experimental measurements of MoS_2 split-nanorings array for biosensing applications. The reason behind choosing MoS_2 is that it has a high refractive index ($n > 4$) and low absorption ($k < 1$) at the visible range of wavelengths independent of thickness [194]. This property helps to achieve light confinement in the nanoresonators and offers opportunities to manipulate light fields at the nanoscale. Also, MoS_2 has been previously used in several biosensing platforms such as single nucleotide [195] and polynucleotide molecular [196] detection, breast cancer biomarker detection by the photoluminescence of monolayer MoS_2 flakes [197]. MoS_2 has also proven to be low cytotoxic and genotoxic [175] and a bio-compatible material. In the previous chapter 6, we have proposed three different MoS_2 metasurface configurations and performed the Finite-Difference Time-Domain (FDTD) method (Ansys

Inc. [108]) to optimize the design of the MoS_2 nanorings array. Here, we fabricate the cross-faced leaky MoS_2 split-nanoring resonator array (configuration 1) for small-size bioanalytes detection. This work presents a novel method for fabricating a large area MoS_2 patterning with high repeatability and reproducibility. As proof of concept of biosensing application, we have also presented polystyrene beads testing with the fabricated devices. Fig. 7.1 illustrates the polystyrene beads detection scheme using MoS_2 split-nanorings array.

7.2 Materials and Methods

7.2.1 Pulsed Laser Deposition Method for MoS_2 growth

MoS_2 thin film of desired thickness was grown by matrix-assisted pulsed laser evaporation (MAPLE) system (PVD Products Inc.) on piranha-cleaned SiO_2/Si substrates. The pulsed laser deposition (PLD) system consists of a high-energy (laser energy: 400 mJ) KrF laser (λ = 248 nm) incident on a solid target of MoS_2 in a vacuum chamber with an incident angle of 45° (see Fig. 7.2). The PLD process is well-known for achieving a controlled growth of stoichiometric thin films of complex compounds with epitaxial matching. Fig. 7.3 shows the photograph of our PLD instrument, and the labels indicate different parts of the system. The samples are first loaded in the load-lock chamber and then transferred to the main deposition chamber to avoid contamination of the deposition chamber. A commercially available MoS_2 target was purchased from Kurt J. Lesker with a 99.9% purity. The target diameter was 1" and 0.25" thick. The high-energy laser pulses ablate the target material surface and generate a plasma consisting of atoms, ions, and radicals, known as the plume. The laser fluence was optimized to 0.8 mJ/cm^2 (with the presence of the aperture), so that laser pulses have enough energy to overcome the ablation threshold of target and initiate the laser ablation process. The base pressure of the deposition chamber in the PLD system was 10^{-7} Torr. The substrates were attached on the substrate holder, which

is placed 5 cm above the MoS_2 target, and the substrate holder is connected to a lamp heater. The maximum temperature of the heater can reach 1000°C. To obtain a highly crystalline MoS_2 thin film, PLD growth parameters such as the substrate to target distance, substrate temperature during growth, post-growth annealing temperature and chamber condition (inert Ar or N_2 gas pressure), and the number of pulses to get the desired thickness are optimized in our lab. The number of laser pulses was optimized to get the desired thickness of MoS_2 110 pulses (1 monolayer (ML)), 170 pulses (2 ML), 240 pulses (3 ML), 410 pulses (5 nm thick), 820 pulses (10 nm thick), 12220 pulses (150 nm thick). The schematic Fig. 7.2 illustrates the PLD system and its working. Bulk MoS_2 thin film of 150 nm thickness was deposited on a SiO_2/Si

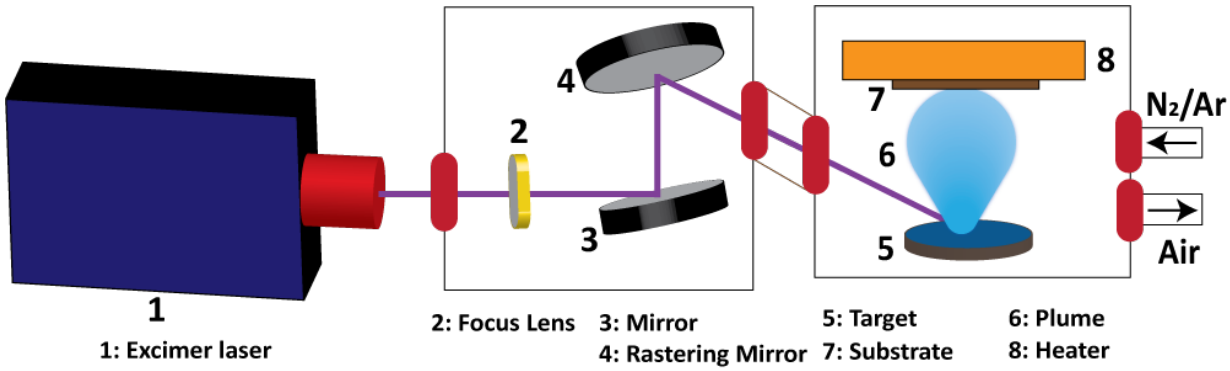

Figure 7.2: Schematic illustration of pulsed laser deposition (PLD) system

at a substrate temperature of 700°C with the above mentioned 12220 laser pulses with the laser repetition rate is 5 Hz. In-situ post-deposition annealing at the same substrate temperature but in an Argon (Ar) atmosphere (0.5 mT) for 30 minutes was performed to improve the crystal quality of the MoS_2 thin films. The growth rate was determined by analyzing the atomic force microscopy (AFM) thickness profile on different samples with varying number of pulses grown.

One of our previously published works [198] demonstrated a highly crystalline large area PLD grown MoS_2 thin film. The as-grown MoS_2 thin film was further characterized by several techniques such as, Raman spectroscopy, X-ray diffraction (XRD), X-ray photoelectron spectroscopy (XPS), atomic force microscopy (AFM), Helium

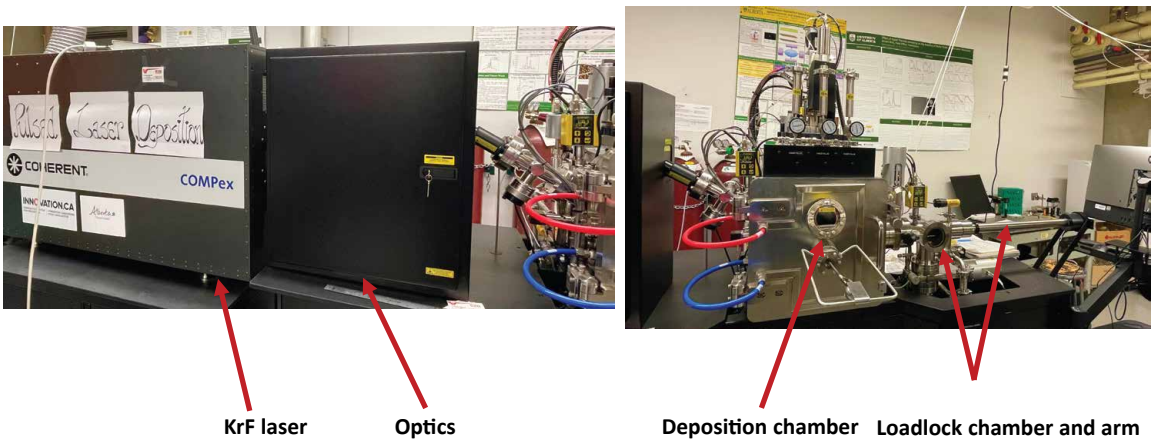

Figure 7.3: Photograph shows our lab's matrix-assisted pulsed laser evaporation (MAPLE) system from PVD Products Ltd.

ion microscopy (HiM) to confirm the quality and uniformity of MoS_2 thin film. Raman shift in Fig. 7.4 (a) confirms the number of layers. Fig. 7.4 (b) and (c) depicts the X-ray photoelectron spectroscopy (XPS) analysis and the demonstrated peak locations at ∽229.59 eV and ∽232.69 eV correspond to the 2H Mo^{4+} $3d^{5/2}$ and $3d^{3/2}$ states of Mo, as observed from the existing reported literature [199, 200]. Also the peak locations at ∽2312.6199 and ∽236.19 eV demonstrate the states of the 2H Mo^{6+} $3d^{5/2}$ and $3d^{3/2}$ states, respectively, as seen from the literature [201]. We also have observed a peak at ∽226.85 eV which matches well with the literature for the S 2s core peak [201]. The peaks of Mo^{4+} correspond to the 2H Mo in MoS_2, which is semiconducting, while the presence of states of Mo^{6+} could indicate either sulfur vacancies during growth or the possibility of MoO_3 formation within the film.21 Therefore, a higher Mo^{4+} : Mo^{6+} ratio is desirable for a better quality of thin films from a device application perspective. The two ratios were determined by comparing the areas under the respective peaks. This ratio was found to be 13.1:1, implying a mostly 2H MoS_2 film with minimal MoO_3.

The transmission electron microscopy (TEM) image in Fig. 7.4 (d) represents the highly crystalline structure of MoS_2, and the number of 3 monolayers (ML) was further confirmed by diffractogram analysis. To verify the stacking and the number of

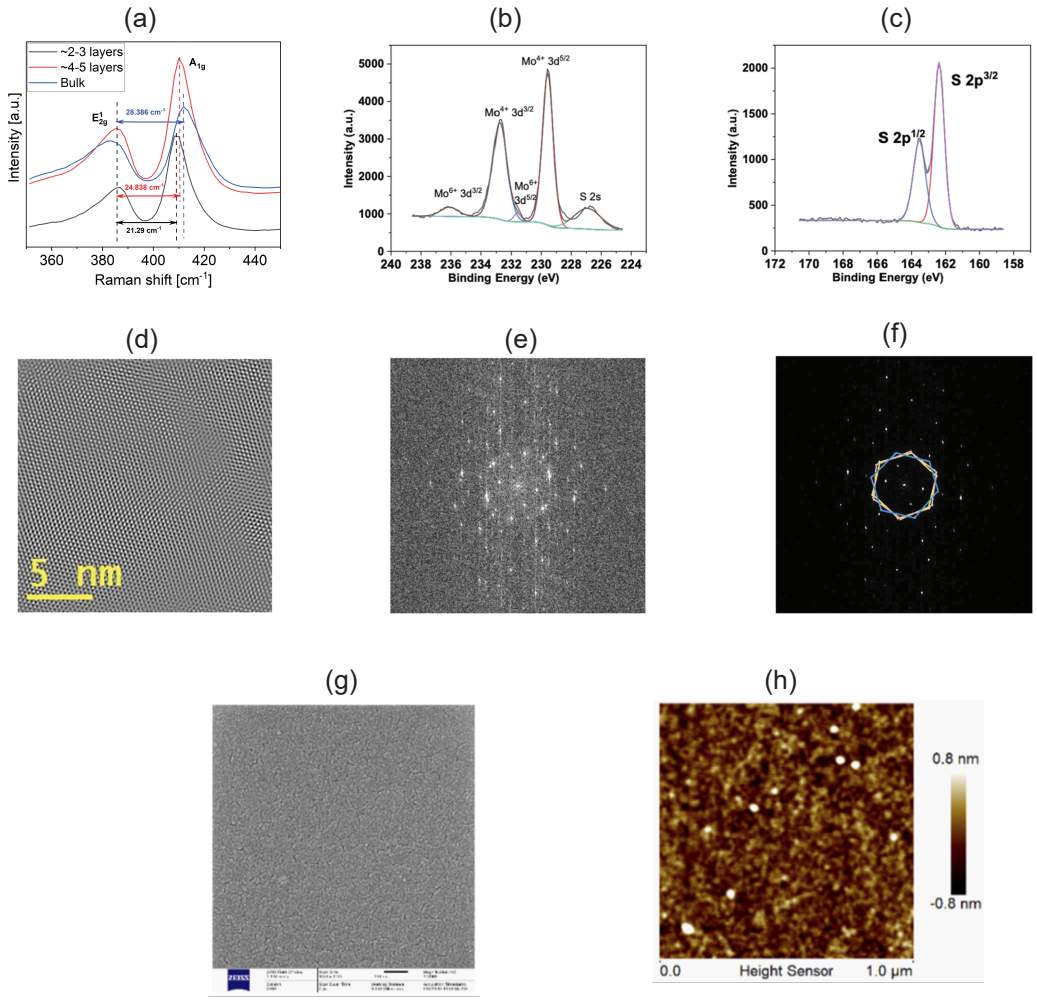

Figure 7.4: Material characterization of PLD grown MoS_2 thin film: (a) Raman spectroscopy of varying thickness. (b) and (c) X-ray photoelectron spectroscopy (XPS) of bulk (60 nm thick) MoS_2 thin film. (d) Transmission electron microscopy (TEM) image of MoS_2 on the SiN_x membrane (e) diffractogram of TEM image obtained after fast Fourier transform, and (f) estimation of the number of MoS_2 monolayers from the diffractogram as three monolayers with an ABA stacking. (g) and (h) Helium ion microscope (HiM) and atomic force microscopy (AFM) images of MoS_2 thin film (3 nm thickness). The images are taken from our published work [198]

monolayers in the thin film using TEM, we grew ∽3 nm MoS_2 thick films. The TEM image for this sample is shown in Fig. 7.4(d), which has a scale bar of 5 nm. A hexagonal lattice structure with regulated bonds formed across the 2D plane can be clearly observed in this figure, indicating the epitaxial growth of MoS_2 via PLD. As this sample was grown on the SiO_2/Si substrate, we obtain high crystallinity without lattice matching. Fig. 7.4(e) shows the electron diffraction pattern of the area imaged in Fig. Fig. 7.4(d). At the center of the pattern, we observe three distinct hexagons with varying intensities, indicating a 3 MLs MoS_2 growth. This diffraction pattern was converted to a dark field image to observe these three MLs better. The diffraction pattern indicates that each consecutive monolayer is rotated by ∽60° with respect to each other, as seen in Figures 7.4(e) and 5(f). This indicates that the MoS_2 film has an ABA stacking. The Helium ion microscope (HiM) and atomic force microscope (AFM) images (see Fig. 7.4 (g) and (h)) of MoS_2 illustrate the surface morphology with the RMS roughness of ∽0.17 nm indicating smoother films for only fewer ML thickness. A short dwell time of 2 μs was used for HiM imaging of the MoS_2 film to reduce the burning of the MoS_2 surface due to the focused He ion beam while imaging.

7.2.2 Fabrication Process of MoS_2 nanoresonators

One of the key novelties of this work is to establish a scalable fabrication process of MoS_2 nanoresonators on a large area PLD growth thin film instead of a small few micron flakes for biosensing applications. Here, we have optimized each step of the fabrication process. Nanoresonator patterns were designed with the Raith design software and fabricated using the RAITH150 Two EBL System. The PLD as-grown MoS_2 (150 nm) thin film is coated with a negative type electron-beam lithography (EBL) resist ma-N 2403. The spin coating parameters - spin-speed (rpm): 3000, time: 60 sec, post-coating annealing: at 80°C for 4 minutes. The EBL process parameters were also optimized to obtain high-resolution nanoresonator structures.

Our optimized condition- beam voltage: 30 kV, aperture used: 15 μm, area dose: 270 μC/cm^2. We have used 100 μm write field and 1000X magnification. Each patterned device area is also 100 μm $\times$ 100 μm, and the distance between two neighboring devices is 1.4 mm apart (edge-to-edge distance) to avoid any signal interference during optical measurements. After EBL patterning, the chips were developed in MF 319 developer for 32 sec and then immediately dipped into DI water for 30 sec, which acts as a development stopper. The EBL patterned devices were used for inductively coupled reactive ion etching (ICP RIE) to dry etch the MoS_2. Our optimized ICP RIE conditions to etch 150 nm thick MoS_2 are ICP power: 150 Watt, RF power: 10 Watt, chamber pressure: 10 mTorr, SF_6 gas flow: 15 sccm, etching time: 2 min. The schematic Fig. 7.5 depicts the proposed process flow of MoS_2 split-nanoring resonators. Fig. 7.6 (a) shows the SEM image taken after EBL patterning and ICP RIE were performed (with the presence of EBL resist), and Fig. 7.6 (b) represents the MoS_2 split-nanoring after removing the EBL resist using acetone bath for 15 minutes. The height of the MoS_2 split-nanoring structures was $\backsim$150 nm measured by AFM after EBL resist strip-off (see AFM profile in Fig. 7.6(c)). The crystalline property of PLD as-grown MoS_2 (thickness 150 nm) thin film was confirmed by XRD as shown in Fig. 7.6(d). The inset image represents the peak fitting, which defines the center peak location at 14.6° with the narrow width (FWHM) = 0.86° representing the high Crystallinity of the structure and this MoS_2 XRD peak matches with the reported value in the literature [202].

7.2.3 Optical Measurements Setup

We have made a customized optical setup in our lab, and a photograph is shown in Fig. 7.7. The optics setup consists of a broadband light source SLS201L (λ = 360 – 2600 nm) purchased from Thorlabs [144]. The light is collimated with the collimator connected to the light source and then incident onto the two mirrors (M1 and M2) placed at 45° angles to each other in free space. The reflected light from M2 mirror

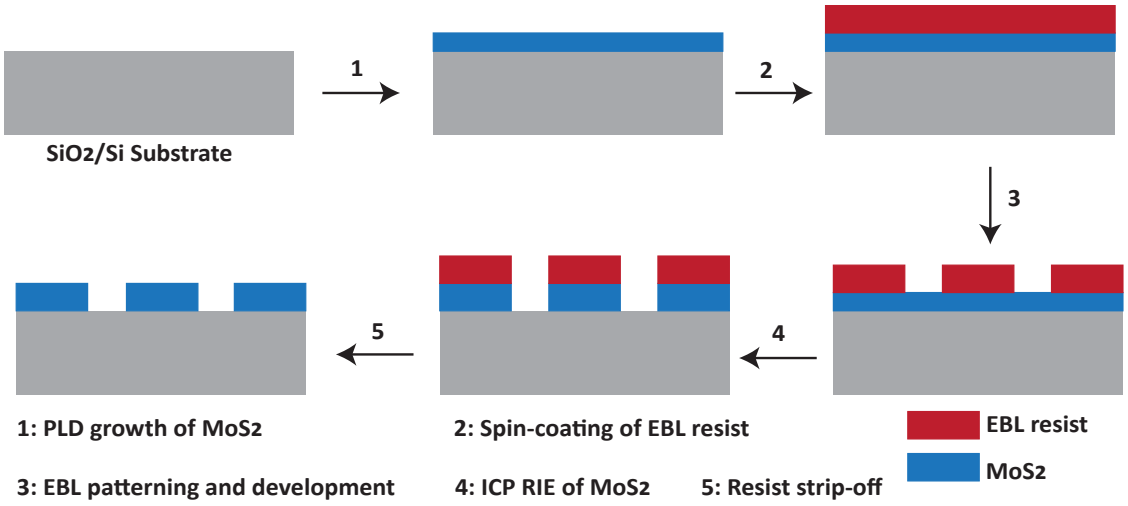

Figure 7.5: Fabrication process flow

was again passed through a collimator and then incident on the 50:50 beam splitter (model: BSW26) placed at 45° angles to the propagation path of light. This makes a normal incident light beam on the microscope objective, and the microscope objective focuses the light beam on the sample surface placed on an X-Y-Z translation stage with a micrometer. We used Nikon PLAN 10×/0.25 with a working distance of 10.5 mm objective lens in our setup. The incident light on the sample surface was reflected from the MoS_2 split-nanoring resonators array on the SiO_2/Si substrate. The reflected light was also collected by the same objective lens and passed across the beam-splitter and the collection lens (focal length (F) = 100 mm) and finally reached the optical fiber where one end of the fiber is connected to an optical tube and the other end of it is connected to a spectrometer (Ocean optics USB4000 wavelength range λ = 177 nm - 810 nm with resolution = 1.34 nm). The focused beam spot size on the sample is $\backsim$800 μm. A CCD camera (model: Chameleon CMLN-13S2M Point Grey Research and software: Point Grey FlyCap2) was used to examine the device and make sure the device was correctly aligned with the beam spot. After aligning each device with the beam spot, the camera was alternatively replaced by the spectrometer's optical fiber to collect the reflection spectrum and the spectral information was recorded using Oceanview software. Postprocessing and data analysis to calculate the resonance

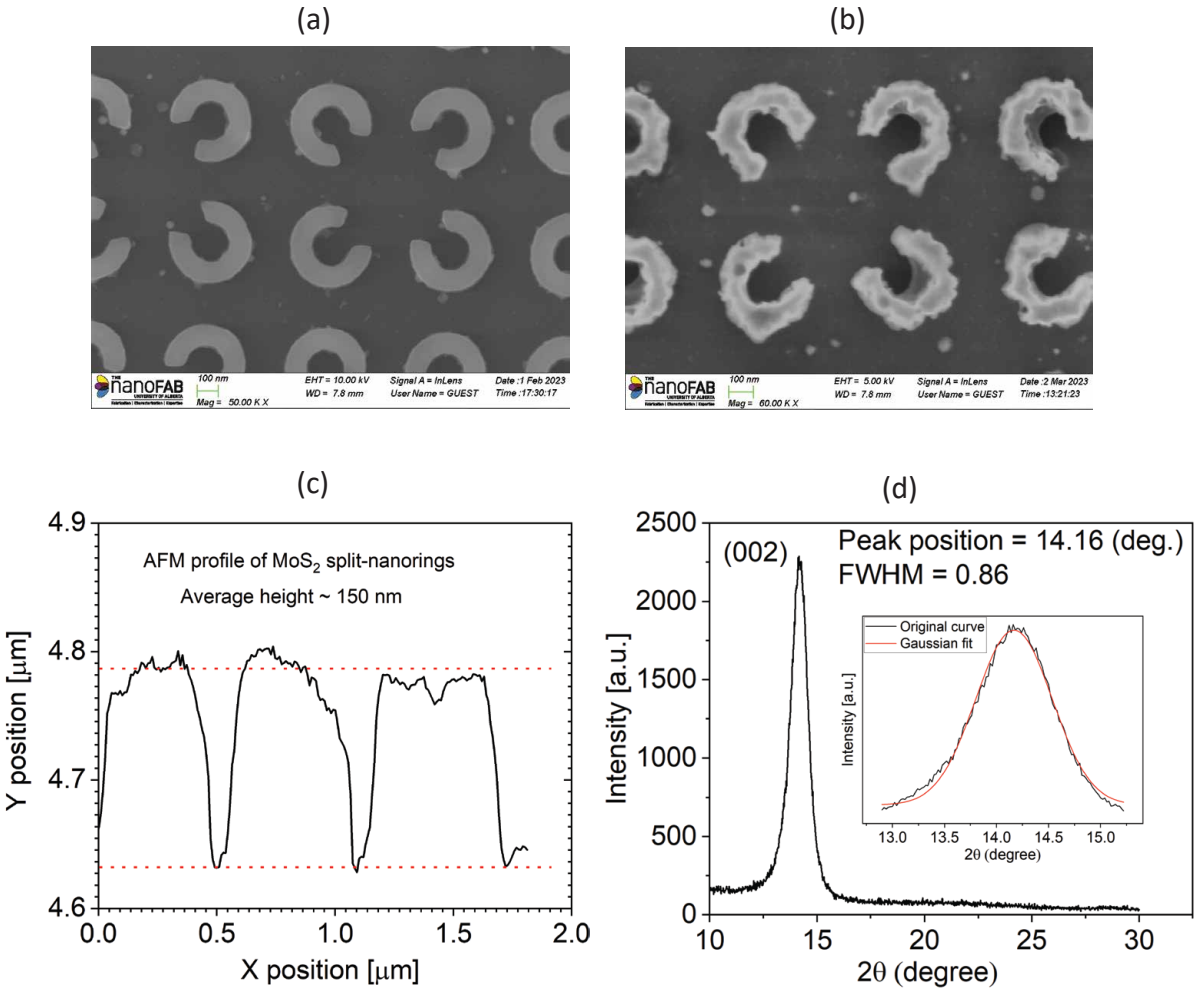

Figure 7.6: (a) Scanning electron microscope (SEM) images of MoS_2 split-nanorings array after ICP RIE (before removing resist) and (b) after strip-off resist, (c) AFM profile image taken after ICP RIE and strip-off the resist showing the average height of 150 nm of MoS_2 split-nanorings. (d) XRD spectrum of 150 nm thick MoS_2 thin film grown on SiO_2/Si substrate.

shift were performed by Origin Lab and MATLAB.

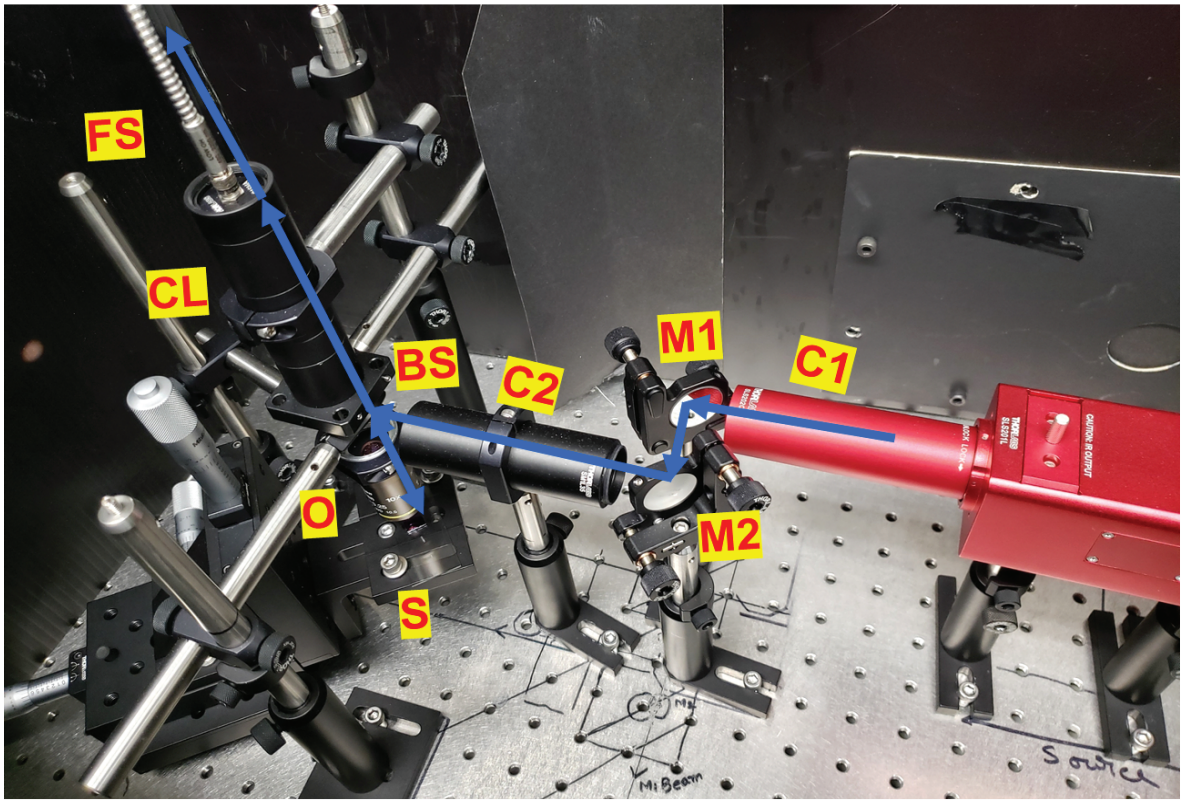

Figure 7.7: Photograph shows the custom lab-made Optics setup. The blue arrow represents the light path through the optics components.

7.3 Results and Discussions

We have performed experimental measurements of polystyrene beads (100 nm diameter) of varying concentrations with the lab-made custom optical setup shown in Fig. 7.7. The polystyrene beads were diluted with deionized (DI) water, and different concentrations ranging from 33 beads/μL to 10^4 beads/μL solution were prepared. 0.3 μL solution of each concentration (resulting in 10 beads to 3000 beads) was drop

cast on 3 different devices separately, and the resonance shifts (averaged from 3 devices) are calculated. Fig. 7.8 (a) shows the reflection spectra measured with the presence of the polystyrene beads, where the inset image shows an enlarged view of resonance wavelength shifts. Fig. 7.8 (b) displays the resonance shift with the number of polystyrene beads, and the slope of the linear response curve demonstrates the experimental detection sensitivity of 4.90 ± 0.63 nm/decade for the 10 to 90 beads range and 13.71 ± 1.7 nm/decade for the 150 to 300 beads range, respectively. It is observed that the minimum number of polystyrene beads that can be detected (LOD) is 4, with the resonance shift observed $\delta\lambda = 0.04$ nm. We have also calculated resonance line-width (FWHM) = 54.8 nm at $\lambda = 566.24$ nm, Q-factor = 10.33, and figures of merit (FOM) = 0.25 (per number of beads in log-scale). Experimental measurements demonstrate that our proposed leaky MoS_2 split-nanoring array is vital for small size ($\backsim$100 nm) bioanalytes detection with ultra-low sample concentration.

We have conducted measurements on the same MoS_2 split-nanorings array device with the polystyrene beads of 1 μm diameter of varying concentrations, and the reflection spectra are shown in Fig. 7.9 (a). The enlarged view of the resonance wavelength displays the red-shift of resonance wavelength with an increase in the number of polystyrene beads. The resonance shift is plotted against the number of polystyrene beads shown in Fig. 7.9 (b). The sensitivity obtained is 1.69 ± 0.79 nm/decade and 10.25 ± 3.48 nm/decade for 30 to 150 and 150 to 300 polystyrene beads, respectively. Notably, the detection sensitivity for the 100 nm-sized polystyrene beads is higher than the 1 μm beads. The split-nanorings size is well-matched with the target beads size of 100 nm, and the resonance field overlap with the 100 nm sized beads is large. On the other hand, only a small area of the 1 μm beads overlaps with the resonance field, creating a lower resonance shift.

In experiments, the fabricated dimensions (as seen in Fig. 7.6) are not the same as our optimized simulated design parameters as discussed in the previous Chapter 6. This is because of the EBL resist resolution and the limitations of ICP RIE etching MoS_2

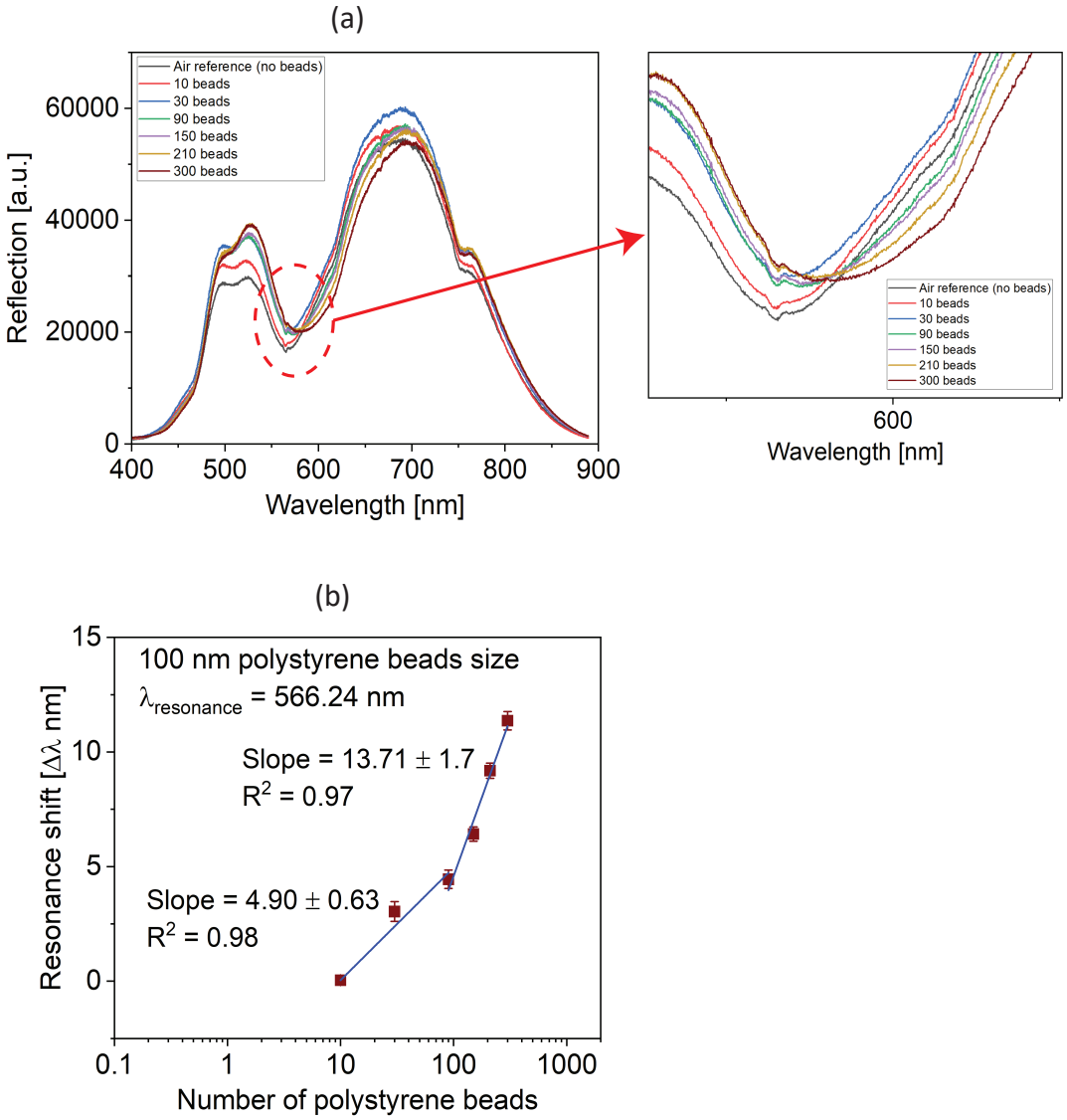

Figure 7.8: Experimental measurements: (a) Reflection spectra with and without the presence of polystyrene beads of 100 nm diameter, and the inset image depicts the enlarged view of the resonance position. (b) The resonance shift curve illustrates the linear response with increased polystyrene beads. Here, each polystyrene bead's diameter is 100 nm.

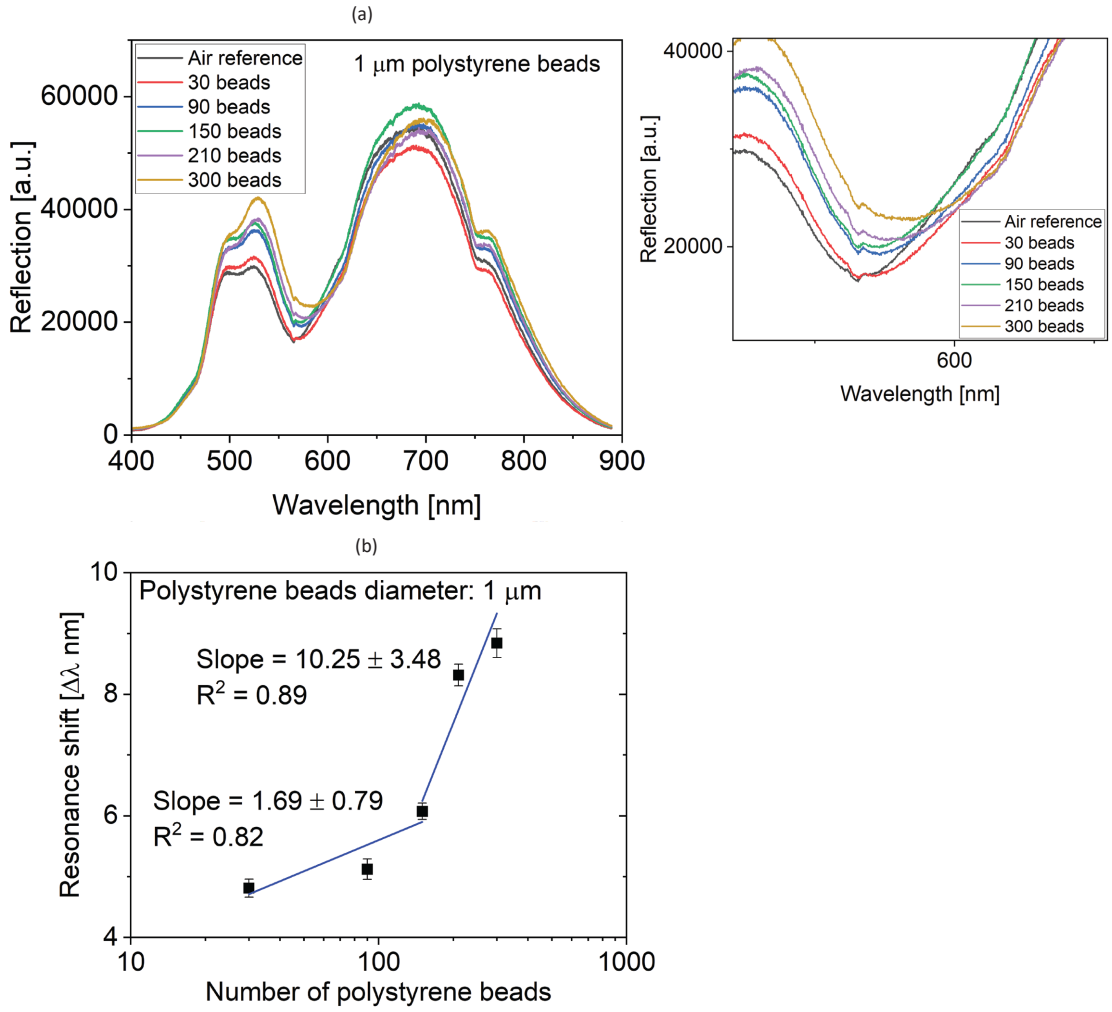

Figure 7.9: 1 μm beads testing: (a) the reflection spectra measured with and without the presence of polystyrene beads. The resonance wavelength red-shifted as seen in the enlarged view resonance wavelength. (b) The resonance shift is plotted against the number of polystyrene beads. The piece-wise linear response of the resonance shift curve shows the best sensitivity of 10.25 $\pm$ 3.48 nm/decade for 1 μm size polystyrene beads.

split-nanorings structure. The aspect ratio (height : width) of the simulation optimized design was 150:100 = 1.5 for individual MoS_2 split-nanoring structure. ICP RIE of MoS_2 with that aspect ratio was difficult because the lowest available ICP power in the system was undercut due to over-etching, and the structures were damaged. The main reason is most of the standard RIE systems were not designed particularly for MoS_2 or other 2D materials, which need low ICP and RF power sources for operation. The difference between the simulation results presented in Chapter 6 and experimental detection sensitivity are due to multiple reasons: (i) sidewall and top surface roughness of fabricated MoS_2 split-nanoring due to the process steps e.g., development of EBL resist with MF 319 developer solution, (ii) ICP RIE etching of MoS_2 split-nanoring, which severely impacts the nanoresonator's Q-factor, leaky behavior, and overall surface quality.

Table 7.1 summarizes our device's sensing performance metrics and compares our device performance parameters with some of the recent dielectric nanoresonator-based biosensing platforms. The simulation and experimental results show the promises of our proposed MoS_2 split-nanoring resonators array-based biosensing platform, which can further be functionalized to detect the SARS-CoV-2 virus specifically. The biofunctionalization process of MoS_2 is demonstrated in the recently published work by J. Wei et.al. [204]. The MoS_2 surface was activated triaminopropyltriethoxy-silane (APTES). The $-OH$ functional groups on the MoS_2 surface react with the silanol of APTES. Then, the SARS-CoV-2 antibody was attached to the functionalized MoS_2 surface for further measurements and attachments of the SARS-CoV-2 antigen.

Table 7.1: Summary of existing dielectric metasurface sensing platforms and comparison with our proposed leaky MoS_2 split-nanorings array metasurface

Dielectric metasurface	Analyte	Sensitivity	FWHM	Q-factor	LOD	FOM
Silicon nanodisks[150]	glucose concentration	86 nm RIU^{-1}	NA	NA	NA	NA
Silicon nanorings and nanobar unit[203]	RI of substance on surface	986 nm RIU^{-1}	14 nm	520	NA	32.7 RIU^{-1}
Silicon nanodisks[74]	breast cancer biomarker ErbB2 and RI medium (DI water and ethanol mixture)	720 nm RIU^{-1}	NA	NA	0.7 ng ML^{-1}	NA
Silicon photonic crystal microcavity [95]	370 nm diameter polystyrene bead	NA	NA	NA	1 bead	NA
MoS_2 split-nanorings array (our work)	polystyrene beads (100 nm)	13.71 nm/decade	54.8 nm	10.33	4 beads	0.25

7.4 Summary

This chapter demonstrates the optimization of the fabrication process of the leaky MoS_2 split-nanoring array and optical measurements of our fabricated devices for biosensing applications. We have shown the testing of varying concentrations of 100 nm polystyrene beads. Our proposed device shows the experimental best detection sensitivity of 13.71 nm/decade and extracted LOD of 4 polystyrene beads. This MoS_2 split-nanoring array platform can be used for further biofunctionalization to detect specific biomolecules such as SARS-CoV-2.

Chapter 8

Summary and Future Works

In this thesis, different categories of nanophotonic biosensors were developed with the aim of small-sized $\leq$ 100 nm bioanalytes sensing. We have explored two primary categories of nanophotonic sensing platforms: (i) plasmonic and (ii) semiconductor metasurface sensors. The design parameters such as diameter, pitch, geometrical shape, and thickness were optimized for both systems to obtain higher detection sensitivity. The optimized design parameters were used for fabricating devices and demonstrated the bioanalytes detection. The significant potential of both nanophotonic biosensors as point-of-care diagnostic platforms is demonstrated.

In Chapter 3, we discussed a design optimization study for a MIM nanopillar array-based nanophotonic biosensing platform that can be tuned to control the leaky behavior of optical fields in individual MIM nanopillars. This was accomplished by modifying the nanopillars' shape, size, pitch, thickness, and materials used for each nanopillar. We also studied the MIM nanopillar's arrangements (square and hexagonal shape of arrays) to achieve uniform sensitivity throughout the device surface. We have demonstrated the detection sensitivity of 101.68 nm RIU^{-1} for device surface refractive index change, where RIU stands for refractive index unit change and 17.66 nm/decade for 100 nm sized polystyrene particles with LOD of 1 particle. Our study shows that relative intensity change at the resonance wavelength also increases with the number of particles distributed over the MIM nanopillar array surface. Our

research findings have uncovered a revolutionary approach to improving the performance of nanophotonic biosensors when dealing with small-sized bioanalytes and established the fact that controlled leaky characteristics in plasmonic MIM nanoresonators are the key to success, than high Q resonators.

In Chapter 4, we have optimized two different MIM nanoresonator configurations performing FDTD simulations. After determining the best design parameters, we fabricated the MIM nanoresonator configurations and conducted experimental measurements using 100 nm-sized polystyrene beads. Our experimental results showed that the MIM nanopillar array had the highest detection sensitivity of $S = 6.54 \pm 0.7$ nm/decade and extracted LOD of 3 polystyrene beads, while the other configuration (Au nanoresonators array on Al_2O_3/Au thin film stack) yielded a sensitivity of 0.88 ± 0.07 nm/decade and LOD of 8 beads. Furthermore, we have addressed the concerns of the manufacturing process and explored methods for enhancing the experimental sensitivities.

In the chapter 5 of thesis, I focused on designing the plasmonic Au nanoresonators for SARS-CoV-2 detection. I performed FDTD simulations to optimize the design parameters of Au nanoresonators, intending to detect bioanalytes of 100 nm in size. The simulation showed that the highest sensitivity of 8.51 nm/decade could be achieved with an array of Au nanoresonators that were 100 nm in diameter and had a pitch of 200 nm. With these optimized design parameters, I fabricated the devices for experimental measurements. I tested the fabricated devices with polystyrene beads of 100 nm diameter, and the bead testing revealed a detection sensitivity of $S_{beads} = 17.05 \pm 3.25$ nm/decade with LOD of 7 polystyrene beads. This result demonstrates the capability of sensing 100 nm-sized bioanalytes in practice. With this motivation, we have fabricated more devices to functionalize for specific detection of SARS-CoV-2. Incorporating the anti-SARS-CoV-2 spike S1 antibody into these devices makes the Au nanoresonators highly specific to SARS-CoV-2. We have reached an extremely low detection limit of 1 VLP μL^{-1} solution with a VLP detection sensitivity of S_{VLP}

= 0.99 ± 0.10 nm/decade. Our cutting-edge plasmonic biosensing platform is a revolutionary tool in the field of disease diagnosis. It has the potential to transform the way we detect SARS-CoV-2, offering unparalleled precision, reliability, and sensitivity with an incredibly low test sample volume of only 1 μL. This breakthrough technology is a true game-changer, and we are confident that it will set a new standard in disease diagnosis. Our highly integrable and scalable nanophotonic biosensing platform is the recommended solution for label-free, rapid detection of SARS-CoV-2, making it an ideal technique for conducting large-volume clinical sample testing.

In Chapter 6, We innovated an avant-garde 2D material metasurface design by constructing tunable leaky MoS_2 nanoresonators, a biocompatible quantum material to revolutionize biosensing technologies. We explored three novel configurations of MoS_2 metasurfaces that are ideal for detecting small bioanalytes and compared their effectiveness. MoS_2 was selected as the nanoresonator's material due to its high refractive index and low absorption coefficient in the visible wavelength range. MoS_2 has been proven to be one of the most biocompatible materials with minimal cytotoxicity. Additionally, its easy bio-functionalization process makes it an ideal choice for various biomedical applications. The best-simulated sensitivity of three MoS_2 nanoresonator configurations are 120 ± 7.72 nm/decade (with cross-faced split nanorings array configuration), 75.12 ± 8.12 nm/decade (with split nanorings chain-like array configuration), and 305.31 ± 29.24 nm/decade (with nanotriangles array configuration) for 100 nm polystyrene particles detection. This study presents a new direction for Mie resonators based on 2D materials in biosensing applications.

In Chapter 7, we have demonstrated the keystone methodology, which enables the fabrication of compact, scalable on-chip sensor arrays consisting of MoS_2 split-nanorings. We also conducted experiments to demonstrate the sensing capabilities and analyze the critical factors that significantly impact the detection of small-sized (100 nm) analytes. Initially, a MoS_2 thin film was grown by the pulsed laser deposition (PLD) technique, and then fabricated the nanoresonator array. Our experiments yielded a

detection sensitivity of 13.71 nm/decade and LOD of 4 polystyrene beads. Although the original design was intended for 100 nm-sized analytes, it can be tuned to accommodate other sizes. The MoS_2 nanoresonator array exhibits near-field enhancement, which makes it an excellent candidate for quantum sensing applications. Additionally, the facile integration of this array with other 2D materials offers endless scientific possibilities. With our cutting-edge technology, we are on the verge of revolutionizing the field of quantum sensing and ushering in a new era of scientific exploration.

Future Work:

- The research in this thesis highlights the tremendous potential of nanophotonic biosensing platforms for future applications. To make these platforms more accessible outside of a laboratory setting, the next step is to create a miniaturized, portable version of the proposed optical system. This can be achieved by integrating optical components into a 6" × 6" × 6" box. Planar photonic integration can be employed to enhance the degree of miniaturization further. This involves on-chip light sources, optical waveguides, active sensing devices, on-chip detectors, and electronic signal processing systems being integrated into a chip (also known as a lab-on-a-chip) arranged in a 1D array. This will enable the independent functioning of the lab-on-a-chip to detect different pathogens simultaneously. Additionally, nanophotonic biosensors can be used with smartphones to reduce costs. This will make it more affordable to utilize light sources, high-resolution cameras, high-quality image processing, and wireless communication systems provided by smartphones.

- In our thesis, we have only used Au as the plasmonic material. However, other plasmonic materials, such as Ag and Pt, can also be used to study the effect of biosensor performances.

- In the future, the MIM nanoresonator devices can be biofunctionalized to demon-

strate *E. Coli* bacteria as this is a common threat to food production industries. Therefore, a compact, non-invasive nanophotonic biosensor could help with rapid testing of food contamination.

- MoS_2 nanoresonator array can be biofunctionalized to demonstrate virus detection, such as Influenza flu viruses as a common virus attacks large populations in North America every year.

- The potential of photonic resonators that incorporate monolayer to few-layer MoS_2 remains vastly untapped. This is despite the fact that MoS_2 displays distinct charge distributions when the number of monolayers is changed. We propose to harness these unique properties by combining them with our groundbreaking split-nanoring structures. The result would be an unparalleled platform for ultra-sensitive detection - one that could revolutionize the field.

- The use of two-dimensional (2D) materials would revolutionize the development of light emission, photodetection, and low-loss waveguiding technologies along with our proposed MoS_2 nanoresonstor biosensing platform. By relying solely on such materials, it is possible to create a wearable biosensor that does not require external light sources or detectors. The addition of artificial intelligence to these biosensors can further enhance their capabilities and enable seamless integration into digital healthcare systems, paving the way for the future of the Internet of Things (IoT).

- Clinical studies need to be conducted to evaluate the effectiveness of the proposed nanophotonic biosensing platforms on COVID-19 patient samples. These sensors can measure patient samples, analyze data using personalized apps, and transmit results to doctors and hospitals for early diagnosis and patient monitoring. Combining nanophotonic structures with advanced functional coatings is necessary for accurately analyzing complex bio-assays and operating in biolog-

ical environments. These developments can produce cost-effective and portable biosensors that cater to healthcare demands, food safety, and environmental monitoring. We envision that such advancements have the potential to elevate our collective standard of living and provide greater service to humanity.

- A photonic inverse design empowered by a machine learning technique can be employed to improve the simulation matching with the experimental dimensions to obtain the desired resonance characteristics. This approach will enable us to achieve resonance characteristics similar to those observed in the experiments, thus increasing the accuracy of our simulations.

- Integration of quantum emitters of 2D materials such as hBN with our proposed MoS_2 nanoresonators can be a next-generation technology for quantum sensing applications.

Bibliography

[1] K. Sadani, P. Nag, X. Y. Thian, and S. Mukherji, "Enzymatic optical biosensors for healthcare applications," *Biosensors and Bioelectronics: X*, vol. 12, p. 100 278, 2022.

[2] B. Kaur, S. Kumar, and B. K. Kaushik, "Novel wearable optical sensors for vital health monitoring systems—a review," *Biosensors*, vol. 13, no. 2, p. 181, 2023.

[3] A. Haleem, M. Javaid, R. P. Singh, R. Suman, and S. Rab, "Biosensors applications in medical field: A brief review," *Sensors International*, vol. 2, p. 100 100, 2021.

[4] A. Sharma, M. Badea, S. Tiwari, and J. L. Marty, "Wearable biosensors: An alternative and practical approach in healthcare and disease monitoring," *Molecules*, vol. 26, no. 3, p. 748, 2021.

[5] R. Gu, Y. Duan, Y. Li, and Z. Luo, "Fiber-optic-based biosensor as an innovative technology for point-of-care testing detection of foodborne pathogenic bacteria to defend food and agricultural product safety," *Journal of Agricultural and Food Chemistry*, vol. 71, no. 29, pp. 10 982–10 988, 2023.

[6] S. Gavrilaș, C. Ș. Ursachi, S. Perța-Crișan, and F.-D. Munteanu, "Recent trends in biosensors for environmental quality monitoring," *Sensors*, vol. 22, no. 4, p. 1513, 2022.

[7] J. J. Ong, T. D. Pollard, A. Goyanes, S. Gaisford, M. Elbadawi, and A. W. Basit, "Optical biosensors-illuminating the path to personalized drug dosing," *Biosensors and Bioelectronics*, vol. 188, p. 113 331, 2021.

[8] A Matthew, "Current biosensor technologies in drug discovery," *Drug discovery*, vol. 69, 2006.

[9] V. Garzón, D. G. Pinacho, R.-H. Bustos, G. Garzón, and S. Bustamante, "Optical biosensors for therapeutic drug monitoring," *Biosensors*, vol. 9, no. 4, p. 132, 2019.

[10] L. K. McGoldrick and J. Halámek, "Recent advances in noninvasive biosensors for forensics, biometrics, and cybersecurity," *Sensors*, vol. 20, no. 21, p. 5974, 2020.

[11] H. Costanzo, J. Gooch, and N. Frascione, "Nanomaterials for optical biosensors in forensic analysis," *Talanta*, p. 123 945, 2022.

[12] L. C. Clark Jr, S. Kaplan, E. C. Matthews, P. K. Edwards, and J. A. Helmsworth, "Monitor and control of blood oxygen tension and ph during total body perfusion," *Journal of Thoracic Surgery*, vol. 36, no. 4, pp. 488–496, 1958.

[13] L. C. Clark Jr and C. Lyons, "Electrode systems for continuous monitoring in cardiovascular surgery," *Annals of the New York Academy of sciences*, vol. 102, no. 1, pp. 29–45, 1962.

[14] K. Cammann, "Bio-sensors based on ion-selective electrodes," *Fresenius Zeitschrift für Analytische Chemie*, vol. 287, no. 1, pp. 1–9, 1977.

[15] D. R. Thevenot, K. Toth, R. A. Durst, and G. S. Wilson, "Electrochemical biosensors: Recommended definitions and classification," *Pure and applied chemistry*, vol. 71, no. 12, pp. 2333–2348, 1999.

[16] K. V. Serebrennikova, A. N. Berlina, D. V. Sotnikov, A. V. Zherdev, and B. B. Dzantiev, "Raman scattering-based biosensing: New prospects and opportunities," *Biosensors*, vol. 11, no. 12, p. 512, 2021.

[17] O. Ambartsumyan, D. Gribanyov, V. Kukushkin, A. Kopylov, and E. Zavyalova, "Sers-based biosensors for virus determination with oligonucleotides as recognition elements," *International Journal of Molecular Sciences*, vol. 21, no. 9, p. 3373, 2020.

[18] S. Vasudevan, P. Srinivasan, J. B. B. Rayappan, and A. P. Solomon, "A photoluminescence biosensor for the detection of n-acyl homoserine lactone using cysteamine functionalized zno nanoparticles for the early diagnosis of urinary tract infections," *Journal of Materials Chemistry B*, vol. 8, no. 19, pp. 4228–4236, 2020.

[19] J. T. Metternich, J. A. Wartmann, L. Sistemich, R. Nißler, S. Herbertz, and S. Kruss, "Near-infrared fluorescent biosensors based on covalent dna anchors," *Journal of the American Chemical Society*, vol. 145, no. 27, pp. 14 776–14 783, 2023.

[20] Y. Song, Y. Cong, B. Wang, and N. Zhang, "Applications of fourier transform infrared spectroscopy to pharmaceutical preparations," *Expert opinion on drug delivery*, vol. 17, no. 4, pp. 551–571, 2020.

[21] M. M. El-Wekil, K. K. Abdelhady, R. A. A. Salam, and G. M. Hadad, "Applications of fourier transform infrared spectroscopic method for simultaneous quantitation of some hypoglycemic drugs in their binary mixtures," *Spectrochimica Acta Part A: Molecular and Biomolecular Spectroscopy*, vol. 213, pp. 249–253, 2019.

[22] H. Bi, C. M. Duarte, M. Brito, V. Vilas-Boas, S. Cardoso, and P. Freitas, "Performance enhanced uv/vis spectroscopic microfluidic sensor for ascorbic acid quantification in human blood," *Biosensors and Bioelectronics*, vol. 85, pp. 568–572, 2016.

[23] M. Lopez *et al.*, "Characterization of the size distribution and aggregation of virus-like nanoparticles used as active ingredients of the hebernasvac therapeutic vaccine against chronic hepatitis b," *Advances in Natural Sciences: Nanoscience and Nanotechnology*, vol. 8, no. 2, p. 025 009, 2017.

[24] V. Filipe, A. Hawe, and W. Jiskoot, "Critical evaluation of nanoparticle tracking analysis (nta) by nanosight for the measurement of nanoparticles and protein aggregates," *Pharmaceutical research*, vol. 27, pp. 796–810, 2010.

[25] N. S. Fracchiolla, S. Artuso, and A. Cortelezzi, "Biosensors in clinical practice: Focus on oncohematology," *Sensors*, vol. 13, no. 5, pp. 6423–6447, 2013.

[26] T. Arakawa, D. V. Dao, and K. Mitsubayashi, "Biosensors and chemical sensors for healthcare monitoring: A review," *IEEE Transactions on Electrical and Electronic Engineering*, vol. 17, no. 5, pp. 626–636, 2022.

[27] H. Efendić, L. S. Bećirović, A. Deumić, and L. G. Pokvić, "Biosensors in monitoring public health: Industry 4.0 applications–a review," *IFAC-PapersOnLine*, vol. 55, no. 4, pp. 38–44, 2022.

[28] I. Cicha, R. Priefer, P. Severino, E. B. Souto, and S. Jain, "Biosensor-integrated drug delivery systems as new materials for biomedical applications," *Biomolecules*, vol. 12, no. 9, p. 1198, 2022.

[29] M. Thakur and K. Ragavan, "Biosensors in food processing," *Journal of food science and technology*, vol. 50, pp. 625–641, 2013.

[30] P Yáñez-Sedeño, L Agüí, R Villalonga, and J. Pingarrón, "Biosensors in forensic analysis. a review," *Analytica chimica acta*, vol. 823, pp. 1–19, 2014.

[31] H. A. Alhadrami, "Biosensors: Classifications, medical applications, and future prospective," *Biotechnology and applied biochemistry*, vol. 65, no. 3, pp. 497–508, 2018.

[32] C. Chen and J. Wang, "Optical biosensors: An exhaustive and comprehensive review," *Analyst*, vol. 145, no. 5, pp. 1605–1628, 2020.

[33] B. Kuswandi, "Simple optical fibre biosensor based on immobilised enzyme for monitoring of trace heavy metal ions," *Analytical and Bioanalytical Chemistry*, vol. 376, pp. 1104–1110, 2003.

[34] H. Li *et al.*, "A new and rapid approach for detecting covid-19 based on s1 protein fragments," *Clinical and Translational Medicine*, vol. 10, no. 2, e90, 2020.

[35] O. Calvo-Lozano *et al.*, "Label-free plasmonic biosensor for rapid, quantitative, and highly sensitive covid-19 serology: Implementation and clinical validation," *Analytical chemistry*, vol. 94, no. 2, pp. 975–984, 2021.

[36] F. Khozeymeh *et al.*, "Hollow-core fiber-based biosensor: A platform for lab-in-fiber optical biosensors for dna detection," *Sensors*, vol. 22, no. 14, p. 5144, 2022.

[37] M. Makela and P. T. Lin, "Detection of sars-cov-2 dna targets using femtoliter optofluidic waveguides," *Analytical Chemistry*, vol. 93, no. 9, pp. 4154–4159, 2021.

[38] M. Loyez *et al.*, "Rapid detection of circulating breast cancer cells using a multiresonant optical fiber aptasensor with plasmonic amplification," *ACS sensors*, vol. 5, no. 2, pp. 454–463, 2020.

[39] D. Chicea, C. Leca, S. Olaru, and L. M. Chicea, "An advanced sensor for particles in gases using dynamic light scattering in air as solvent," *Sensors*, vol. 21, no. 15, p. 5115, 2021.

[40] A. Levin *et al.*, "Dynamic light scattering biosensing based on analyte-induced inhibition of nanoparticle aggregation," *Analytical and bioanalytical chemistry*, vol. 412, pp. 3423–3431, 2020.

[41] L. Liu, F. He, Y. Yu, and Y. Wang, "Application of fret biosensors in mechanobiology and mechanopharmacological screening," *Frontiers in Bioengineering and Biotechnology*, vol. 8, p. 595 497, 2020.

[42] Y. H. Isayama and H. E. Hernández-Figueroa, "High-order multimode waveguide interferometer for optical biosensing applications," *Sensors*, vol. 21, no. 9, p. 3254, 2021.

[43] A. Psarouli *et al.*, "Fast label-free detection of c-reactive protein using broadband mach-zehnder interferometers integrated on silicon chips," *Talanta*, vol. 165, pp. 458–465, 2017.

[44] G. Allison *et al.*, "A fabry-pérot cavity coupled surface plasmon photodiode for electrical biomolecular sensing," *Nature Communications*, vol. 12, no. 1, p. 6483, 2021.

[45] M. E. Anderson, E. C. O'Brien, E. N. Grayek, J. K. Hermansen, and H. K. Hunt, "The detection of helicobacter hepaticus using whispering-gallery mode microcavity optical sensors," *Biosensors*, vol. 5, no. 3, pp. 562–576, 2015.

[46] T. Endo, H. Kajita, Y. Kawaguchi, T. Kosaka, and T. Himi, "Label-free optical detection of c-reactive protein by nanoimprint lithography-based 2d-photonic crystal film," *Biotechnology Journal*, vol. 11, no. 6, pp. 831–837, 2016.

[47] T. van Leest and J. Caro, "Cavity-enhanced optical trapping of bacteria using a silicon photonic crystal," *Lab on a Chip*, vol. 13, no. 22, pp. 4358–4365, 2013.

[48] S. K. Arya and P. Estrela, "Electrochemical elisa protein biosensing in undiluted serum using a polypyrrole-based platform," *Sensors*, vol. 20, no. 10, p. 2857, 2020.

[49] J. M. Hum, A. P. Siegel, F. M. Pavalko, and R. N. Day, "Monitoring biosensor activity in living cells with fluorescence lifetime imaging microscopy," *International journal of molecular sciences*, vol. 13, no. 11, pp. 14 385–14 400, 2012.

[50] C. Huang, K. Bonroy, G. Reekman, K. Verstreken, L. Lagae, and G. Borghs, "An on-chip localized surface plasmon resonance-based biosensor for label-free monitoring of antigen–antibody reaction," *Microelectronic Engineering*, vol. 86, no. 12, pp. 2437–2441, 2009.

[51] G. Mie, "Beiträge zur optik trüber medien, speziell kolloidaler metallösungen," *Annalen der physik*, vol. 330, no. 3, pp. 377–445, 1908.

[52] R. H. Ritchie, "Plasma losses by fast electrons in thin films," *Physical review*, vol. 106, no. 5, p. 874, 1957.

[53] M. A. Mahmoud, M. Chamanzar, A. Adibi, and M. A. El-Sayed, "Effect of the dielectric constant of the surrounding medium and the substrate on the surface plasmon resonance spectrum and sensitivity factors of highly symmetric systems: Silver nanocubes," *Journal of the American Chemical Society*, vol. 134, no. 14, pp. 6434–6442, 2012.

[54] S. D. Soelberg *et al.*, "A portable surface plasmon resonance sensor system for real-time monitoring of small to large analytes," *Journal of industrial microbiology and biotechnology*, vol. 32, no. 11-12, pp. 669–674, 2005.

[55] K. Narayan and S. S. Carroll, "Spr screening," in *Applied Biophysics for Drug Discovery*. John Wiley & Sons, Ltd, 2017, ch. 6, pp. 93–105, ISBN: 9781119099512.

[56] E. Hecht, "The propagation of light," in *Optics*. Pearson, 2017, ch. 4, p. 104, ISBN: 978-1-292-09693-3.

[57] R. W. Wood, "Xliv. a suspected case of the electrical resonance of minute metal particles for light-waves. a new type of absorption," *The London, Edinburgh, and Dublin Philosophical Magazine and Journal of Science*, vol. 3, no. 16, pp. 396–410, 1902. DOI: 10.1080/14786440209462780.

[58] P. Ren, O. Krupin, P. Berini, and R. N. Tait, "Fabrication of long range surface plasmon waveguide biosensors in a low-index fluoropolymer," *Journal of Vacuum Science & Technology B, Nanotechnology and Microelectronics: Materials, Processing, Measurement, and Phenomena*, vol. 36, no. 4, p. 042 601, 2018.

[59] O. Krupin and P. Berini, "Long-range plasmonic waveguide sensors," pp. 29–55, 2020.

[60] M. Khodami *et al.*, "Fabrication of bloch long range surface plasmon waveguides integrating counter electrodes and microfluidic channels for multimodal biosensing," *Journal of Microelectromechanical Systems*, vol. 30, no. 5, pp. 686–695, 2021.

[61] G. V. Hartland, "Optical studies of dynamics in noble metal nanostructures," *Chemical reviews*, vol. 111, no. 6, pp. 3858–3887, 2011.

[62] L. Huang *et al.*, "One-step rapid quantification of sars-cov-2 virus particles via low-cost nanoplasmonic sensors in generic microplate reader and point-of-care device," *Biosensors and Bioelectronics*, vol. 171, p. 112 685, 2021.

[63] H. Khateb, G. Klös, R. L. Meyer, and D. S. Sutherland, "Development of a label-free lspr-apta sensor for staphylococcus aureus detection," *ACS Applied Bio Materials*, vol. 3, no. 5, pp. 3066–3077, 2020.

[64] A. Belushkin, F. Yesilkoy, and H. Altug, "Nanoparticle-enhanced plasmonic biosensor for digital biomarker detection in a microarray," *ACS nano*, vol. 12, no. 5, pp. 4453–4461, 2018.

[65] D. Kawasaki, H. Yamada, K. Maeno, K. Sueyoshi, H. Hisamoto, and T. Endo, "Core–shell-structured gold nanocone array for label-free dna sensing," *ACS Applied Nano Materials*, vol. 2, no. 8, pp. 4983–4990, 2019.

[66] M. Loyez *et al.*, "Rapid detection of circulating breast cancer cells using a multiresonant optical fiber aptasensor with plasmonic amplification," *ACS sensors*, vol. 5, no. 2, pp. 454–463, 2020.

[67] A. Pors and S. I. Bozhevolnyi, "Plasmonic metasurfaces for efficient phase control in reflection," *Optics express*, vol. 21, no. 22, pp. 27 438–27 451, 2013.

[68] D. K. Gramotnev, A. Pors, M. Willatzen, and S. I. Bozhevolnyi, "Gap-plasmon nanoantennas and bowtie resonators," *Physical Review B*, vol. 85, no. 4, p. 045 434, 2012.

[69] L. P. Hackett, A. Ameen, W. Li, F. K. Dar, L. L. Goddard, and G. L. Liu, "Spectrometer-free plasmonic biosensing with metal–insulator–metal nanocup arrays," *ACS sensors*, vol. 3, no. 2, pp. 290–298, 2018.

[70] S. Sun *et al.*, "All-dielectric full-color printing with tio2 metasurfaces," *ACS nano*, vol. 11, no. 5, pp. 4445–4452, 2017.

[71] F. Yesilkoy *et al.*, "Ultrasensitive hyperspectral imaging and biodetection enabled by dielectric metasurfaces," *Nature Photonics*, vol. 13, no. 6, pp. 390–396, 2019.

[72] J. Tian, H. Luo, Q. Li, X. Pei, K. Du, and M. Qiu, "Near-infrared super-absorbing all-dielectric metasurface based on single-layer germanium nanostructures," *Laser & Photonics Reviews*, vol. 12, no. 9, p. 1 800 076, 2018.

[73] O. Yavas, M. Svedendahl, P. Dobosz, V. Sanz, and R. Quidant, "On-a-chip biosensing based on all-dielectric nanoresonators," *Nano letters*, vol. 17, no. 7, pp. 4421–4426, 2017.

[74] Y. Wang, M. A. Ali, E. K. Chow, L. Dong, and M. Lu, "An optofluidic metasurface for lateral flow-through detection of breast cancer biomarker," *Biosensors and Bioelectronics*, vol. 107, pp. 224–229, 2018.

[75] A. I. Kuznetsov, A. E. Miroshnichenko, Y. H. Fu, J. Zhang, and B. Luk'Yanchuk, "Magnetic light," *Scientific reports*, vol. 2, no. 1, pp. 1–6, 2012.

[76] A. I. Kuznetsov, A. E. Miroshnichenko, M. L. Brongersma, Y. S. Kivshar, and B. Luk'yanchuk, "Optically resonant dielectric nanostructures," *Science*, vol. 354, no. 6314, aag2472, 2016.

[77] R. Merlin, "Metamaterials and the landau–lifshitz permeability argument: Large permittivity begets high-frequency magnetism," *Proceedings of the National Academy of Sciences*, vol. 106, no. 6, pp. 1693–1698, 2009.

[78] A. E. Miroshnichenko and Y. S. Kivshar, "Fano resonances in all-dielectric oligomers," *Nano letters*, vol. 12, no. 12, pp. 6459–6463, 2012.

[79] X. Long, M. Zhang, Z. Xie, M. Tang, and L. Li, "Sharp fano resonance induced by all-dielectric asymmetric metasurface," *Optics Communications*, vol. 459, p. 124 942, 2020.

[80] W. Su, Y. Ding, Y. Luo, and Y. Liu, "A high figure of merit refractive index sensor based on fano resonance in all-dielectric metasurface," *Results in Physics*, vol. 16, p. 102 833, 2020.

[81] P. B. Johnson and R.-W. Christy, "Optical constants of the noble metals," *Physical review B*, vol. 6, no. 12, p. 4370, 1972.

[82] L. Cao, B. Li, and J. H. Zhao, "Etching of sic using inductively coupled plasma," *Journal of The Electrochemical Society*, vol. 145, no. 10, p. 3609, 1998.

[83] D. Kim *et al.*, "High rate etching of 6h–sic in sf6-based magnetically-enhanced inductively coupled plasmas," *Thin Solid Films*, vol. 447, pp. 100–104, 2004.

[84] H. Ekinci, V. V. Kuryatkov, D. L. Mauch, J. C. Dickens, and S. A. Nikishin, "Effect of bcl3 in chlorine-based plasma on etching 4h-sic for photoconductive semiconductor switch applications," *Journal of Vacuum Science & Technology B, Nanotechnology and Microelectronics: Materials, Processing, Measurement, and Phenomena*, vol. 32, no. 5, p. 051 205, 2014.

[85] W. H. Bragg and W. L. Bragg, "The reflection of x-rays by crystals," *Proceedings of the Royal Society of London. Series A, Containing Papers of a Mathematical and Physical Character*, vol. 88, no. 605, pp. 428–438, 1913.

[86] S. Aherfi, P. Colson, B. L. Scola, and D. Raoult, "Giant viruses of amoebas: An update," *Frontiers in Microbiology*, vol. 7, 2016.

[87] A. E. Balaev, K. N. Dvoretski, and V. A. Doubrovski, "Refractive index of escherichia coli cells," in *Saratov Fall Meeting 2001: Optical Technologies in Biophysics and Medicine III*, V. V. Tuchin, Ed., International Society for Optics and Photonics, vol. 4707, SPIE, 2002, pp. 253 –260.

[88] A. Katz *et al.*, "In situ determination of refractive index and size of bacillus spores by light transmission," *Opt. Lett.*, vol. 30, no. 6, pp. 589–591, 2005.

[89] Z. Xie *et al.*, "Highly-sensitive optical biosensor based on equal fsr cascaded microring resonator with intensity interrogation for detection of progesterone molecules," *Opt. Express*, vol. 25, no. 26, pp. 33 193–33 201, 2017.

[90] S. M. Lo, S. Hu, G. Gaur, Y. Kostoulas, S. M. Weiss, and P. M. Fauchet, "Photonic crystal microring resonator for label-free biosensing," *Opt. Express*, vol. 25, no. 6, pp. 7046–7054, 2017.

[91] J. Zhu *et al.*, "On-chip single nanoparticle detection and sizing by mode splitting in an ultrahigh-q microresonator," *Nature Photonics*, vol. 4, pp. 46–49, 2010.

[92] F. Vollmer, S. Arnold, and D. Keng, "Single virus detection from the reactive shift of a whispering-gallery mode," *Proceedings of the National Academy of Sciences*, vol. 105, no. 52, pp. 20 701–20 704, 2008.

[93] Y.-F. Chen, X. Serey, R. Sarkar, P. Chen, and D. Erickson, "Controlled photonic manipulation of proteins and other nanomaterials," *Nano Letters*, vol. 12, no. 3, pp. 1633–1637, 2012.

[94] P. Kang, P. Schein, X. Serey, D. O'Dell, and D. Erickson, "Nanophotonic detection of freely interacting molecules on a single influenza virus," *Scientific Reports*, vol. 5, no. 12087, pp. 1–11, 2015.

[95] M. R. Lee and P. M. Fauchet, "Nanoscale microcavity sensor for single particle detection," *Opt. Lett.*, vol. 32, no. 22, pp. 3284–3286, 2007.

[96] M. Lee and P. M. Fauchet, "Two-dimensional silicon photonic crystal based biosensing platform for protein detection," *Opt. Express*, vol. 15, no. 8, pp. 4530–4535, 2007.

[97] S. E. Baker *et al.*, "Detection of bio-organism simulants using random binding on a defect-free photonic crystal," *Applied Physics Letters*, vol. 97, no. 11, p. 113 701, 2010.

[98] H. Chen, A. M. Bhuiya, R. Liu, D. M. Wasserman, and K. C. Toussaint, "Design, fabrication, and characterization of near-ir gold bowtie nanoantenna arrays," *The Journal of Physical Chemistry C*, vol. 118, no. 35, pp. 20 553–20 558, 2014.

[99] Z. Zhang *et al.*, "Gold crescent nanodisk array for nanoantenna-enhanced sensing in subwavelength areas," *Applied Optics*, vol. 53, no. 31, pp. 7236–7240, 2014.

[100] A. Dhawan, M. Canva, and T. Vo-Dinh, "Narrow groove plasmonic nanogratings for surface plasmon resonance sensing," *Optics Express*, vol. 19, no. 2, pp. 787–813, 2011.

[101] R. Chikkaraddy *et al.*, "Single-molecule strong coupling at room temperature in plasmonic nanocavities," *Nature*, vol. 535, pp. 127–130, 2016.

[102] Y. Shen *et al.*, "Plasmonic gold mushroom arrays with refractive index sensing figures of merit approaching the theoretical limit," *Nature Communications*, vol. 4, no. 2381, pp. 1–9, 2013.

[103] A. Ameen *et al.*, "Plasmonic sensing of oncoproteins without resonance shift using 3d periodic nanocavity in nanocup arrays," *Advanced Optical Materials*, vol. 5, no. 11, p. 1 601 051, 2017.

[104] L. P. Hackett, A. Ameen, W. Li, F. K. Dar, L. L. Goddard, and G. L. Liu, "Spectrometer-free plasmonic biosensing with metal–insulator–metal nanocup arrays," *ACS Sensors*, vol. 3, no. 2, pp. 290–298, 2018.

[105] L. P. Hackett, W. Li, A. Ameen, L. L. Goddard, and G. L. Liu, "Plasmonic metal–insulator–metal capped polymer nanopillars for sers analysis of protein–protein interactions," *The Journal of Physical Chemistry C*, vol. 122, no. 11, pp. 6255–6266, 2018.

[106] L. Qin, S. Wu, J. hua Deng, L. Li, and X. Li, "Tunable light absorbance by exciting the plasmonic gap mode for refractive index sensing," *Opt. Lett.*, vol. 43, no. 7, pp. 1427–1430, 2018.

[107] D. E. Nelson and K. D. Young, "Penicillin binding protein 5 affects cell diameter, contour, and morphology of escherichia coli," *Journal of Bacteriology*, vol. 182, no. 6, pp. 1714–1721, 2000.

[108] *Ansys-Lumerical: https:// www.ansys.com/ products/ photonics/ fdtd.*.

[109] K. L. Kelly, E. Coronado, L. L. Zhao, and G. C. Schatz, "The optical properties of metal nanoparticles: The influence of size, shape, and dielectric environment," *The Journal of Physical Chemistry B*, vol. 107, no. 3, pp. 668–677, 2003.

[110] V. Amendola, R. Pilot, M. Frasconi, O. M. Maragò, and M. A. Iatì, "Surface plasmon resonance in gold nanoparticles: A review," *Journal of Physics: Condensed Matter*, vol. 29, no. 20, p. 203 002, 2017.

[111] N. Guillot *et al.*, "Surface enhanced raman scattering optimization of gold nanocylinder arrays: Influence of the localized surface plasmon resonance and excitation wavelength," *Applied Physics Letters*, vol. 97, no. 2, p. 023 113, 2010.

[112] L. Jiang *et al.*, "Probing vertical and horizontal plasmonic resonant states in the photoluminescence of gold nanodisks," *ACS Photonics*, vol. 2, no. 8, pp. 1217–1223, 2015.

[113] P. Ghosh, V. Thambi, A. Kar, A. L. Chakraborty, and S. Khatua, "Light-induced in situ active tuning of the lspr of gold nanorods over 90 nm," *Opt. Lett.*, vol. 46, no. 18, pp. 4562–4565, 2021.

[114] E. Dulkeith *et al.*, "Plasmon emission in photoexcited gold nanoparticles," *Phys. Rev. B*, vol. 70, p. 205 424, 20 2004.

[115] R. Malabi, S. Manoto, S. Ombinda-Lemboumba, M. Maaza, and P. Mthunzi-Kufa, "Detection of biological analytes using surface plasmon resonance as a biosensing technique for possible development of a point of care diagnostic tool," in *Plasmonics in Biology and Medicine XVI*, vol. 10894, SPIE, 2019, pp. 87 –92.

[116] I. H. Malitson, F. V. Murphy, and W. S. Rodney, "Refractive index of synthetic sapphire," *J. Opt. Soc. Am.*, vol. 48, no. 1, pp. 72–73, 1958.

[117] T. Siefke *et al.*, "Materials pushing the application limits of wire grid polarizers further into the deep ultraviolet spectral range," *Advanced Optical Materials*, vol. 4, no. 11, pp. 1780–1786, 2016.

[118] S. H. Jones, M. D. King, and A. D. Ward, "Determining the unique refractive index properties of solid polystyrene aerosol using broadband mie scattering from optically trapped beads," *Phys. Chem. Chem. Phys.*, vol. 15, pp. 20 735–20 741, 47 2013.

[119] T. Shima *et al.*, "Detection of influenza viruses attached to an optical disk," *Journal of Biomaterials and Nanobiotechnology*, vol. 4, no. 2, pp. 145–150, 2013.

[120] G. W. Burr and A. Farjadpour, "Balancing accuracy against computation time: 3-d fdtd for nanophotonics device optimization," vol. 5733, Photonic Crystal Materials and Devices III, SPIE, 2005, pp. 336–347.

[121] G. Sun, "Development and evaluation of novel finite-difference time-domain methods for solving maxwell's equations," Unpublished, Ph.D. dissertation, Concordia University, 2004. [Online]. Available: https://spectrum.library.concordia.ca/id/eprint/8293/.

[122] A. Pors and S. I. Bozhevolnyi, "Plasmonic metasurfaces for efficient phase control in reflection," *Opt. Express*, vol. 21, no. 22, pp. 27 438–27 451, 2013.

[123] C. Hsu *et al.*, "Thickness-dependent refractive index of 1l, 2l, and 3l mos2, mose2, ws2, and wse2," *Advanced Optical Materials*, vol. 7, no. 13, p. 1 900 239, 2019.

[124] H. Chen, X. Kou, Z. Yang, W. Ni, and J. Wang, "Shape- and size-dependent refractive index sensitivity of gold nanoparticles," *Langmuir*, vol. 24, no. 10, pp. 5233–5237, 2008.

[125] H. Jiang, T. Li, E. Ertorer, J. Yang, J. Sabarinathan, and S. Mittler, "A biosensor based on periodic arrays of gold nanodisks under normal transmission," *Sensors and Actuators A: Physical*, vol. 189, pp. 474–480, 2013, ISSN: 0924-4247.

[126] G. Duffett, R. Wirth, M. Rayer, E. R. Martins, and T. F. Krauss, "Metal-insulator-metal nanoresonators – strongly confined modes for high surface sensitivity," *Nanophotonics*, vol. 9, no. 6, pp. 1547–1552, 2020.

[127] M. Butt, S. Khonina, N. Kazanskiy, and R. Piramidowicz, "Hybrid metasurface perfect absorbers for temperature and biosensing applications," *Optical Materials*, vol. 123, p. 111 906, 2022, ISSN: 0925-3467.

[128] C. Y. Chang *et al.*, "Flexible localized surface plasmon resonance sensor with metal–insulator–metal nanodisks on pdms substrate," *Scientific Reports*, vol. 8, no. 11812, pp. 2045–2322, 2018.

[129] M. M. Wiecha *et al.*, "Direct near-field observation of surface plasmon polaritons on silver nanowires," *ACS Omega*, vol. 4, no. 26, pp. 21 962–21 966, 2019.

[130] *Horiba spectrometer*, https://www.horiba.com/int/products/detail/action/show/Product/1000m-series-1587/.

[131] A. Dmitriev *et al.*, "Enhanced nanoplasmonic optical sensors with reduced substrate effect," *Nano letters*, vol. 8, no. 11, pp. 3893–3898, 2008.

[132] N. A. Hatab *et al.*, "Free-standing optical gold bowtie nanoantenna with variable gap size for enhanced raman spectroscopy," *Nano letters*, vol. 10, no. 12, pp. 4952–4955, 2010.

[133] L. P. Hackett, W. Li, A. Ameen, L. L. Goddard, and G. L. Liu, "Plasmonic metal–insulator–metal capped polymer nanopillars for sers analysis of protein–protein interactions," *The Journal of Physical Chemistry C*, vol. 122, no. 11, pp. 6255–6266, 2018.

[134] I. M. Pryce, Y. A. Kelaita, K. Aydin, and H. A. Atwater, "Compliant metamaterials for resonantly enhanced infrared absorption spectroscopy and refractive index sensing," *ACS nano*, vol. 5, no. 10, pp. 8167–8174, 2011.

[135] N. Verellen *et al.*, "Plasmon line shaping using nanocrosses for high sensitivity localized surface plasmon resonance sensing," *Nano letters*, vol. 11, no. 2, pp. 391–397, 2011.

[136] J. B. Lassiter *et al.*, "Fano resonances in plasmonic nanoclusters: Geometrical and chemical tunability," *Nano letters*, vol. 10, no. 8, pp. 3184–3189, 2010.

[137] L. J. Sherry, S.-H. Chang, G. C. Schatz, R. P. Van Duyne, B. J. Wiley, and Y. Xia, "Localized surface plasmon resonance spectroscopy of single silver nanocubes," *Nano letters*, vol. 5, no. 10, pp. 2034–2038, 2005.

[138] Y. Shen *et al.*, "Plasmonic gold mushroom arrays with refractive index sensing figures of merit approaching the theoretical limit," *Nature communications*, vol. 4, no. 1, p. 2381, 2013.

[139] J.-T. Shen, P. B. Catrysse, and S. Fan, "Mechanism for designing metallic metamaterials with a high index of refraction," *Physical review letters*, vol. 94, no. 19, p. 197 401, 2005.

[140] S. Szunerits and R. Boukherroub, "Sensing using localised surface plasmon resonance sensors," *Chemical Communications*, vol. 48, no. 72, pp. 8999–9010, 2012.

[141] J.-S. Chen, P.-F. Chen, H. T.-H. Lin, and N.-T. Huang, "A localized surface plasmon resonance (lspr) sensor integrated automated microfluidic system for multiplex inflammatory biomarker detection," *Analyst*, vol. 145, no. 23, pp. 7654–7661, 2020.

[142] G. Qiu, Z. Gai, Y. Tao, J. Schmitt, G. A. Kullak-Ublick, and J. Wang, "Dual-functional plasmonic photothermal biosensors for highly accurate severe acute respiratory syndrome coronavirus 2 detection," *ACS nano*, vol. 14, no. 5, pp. 5268–5277, 2020.

[143] A. Ahmadivand, B. Gerislioglu, Z. Ramezani, A. Kaushik, P. Manickam, and S. A. Ghoreishi, "Functionalized terahertz plasmonic metasensors: Femtomolar-level detection of sars-cov-2 spike proteins," *Biosensors and Bioelectronics*, vol. 177, p. 112 971, 2021.

[144] *Thorlabs https://www.thorlabs.com/*.

[145] V. Amendola, R. Pilot, M. Frasconi, O. M. Maragò, and M. A. Iatì, "Surface plasmon resonance in gold nanoparticles: A review," *Journal of Physics: Condensed Matter*, vol. 29, no. 20, p. 203 002, 2017.

[146] Y. M. Bar-On, A. Flamholz, R. Phillips, and R. Milo, "Sars-cov-2 (covid-19) by the numbers," *elife*, vol. 9, e57309, 2020.

[147] T. Shima *et al.*, "Detection of influenza viruses attached to an optical disk," 2013.

[148] V. T. Hoang *et al.*, "Optical properties of buffers and cell culture media for optofluidic and sensing applications," *Applied Sciences*, vol. 9, no. 6, p. 1145, 2019.

[149] J. Fan, S. Parr, S. Kang, and M. Gupta, "Point-of-care (poc) sars-cov-2 antigen detection using functionalized aerosol jet-printed organic electrochemical transistors (oects)," *Nanoscale*, vol. 15, no. 11, pp. 5476–5485, 2023.

[150] O. Yavas, M. Svedendahl, and R. Quidant, "Unravelling the role of electric and magnetic dipoles in biosensing with si nanoresonators," *ACS nano*, vol. 13, no. 4, pp. 4582–4588, 2019.

[151] M. A. Gorlach *et al.*, "Far-field probing of leaky topological states in all-dielectric metasurfaces," *Nature communications*, vol. 9, no. 1, p. 909, 2018.

[152] M. Wang *et al.*, "Topological one-way large-area waveguide states in magnetic photonic crystals," *Physical Review Letters*, vol. 126, no. 6, p. 067 401, 2021.

[153] C.-C. Lu *et al.*, "On-chip topological nanophotonic devices," *Chip*, vol. 1, no. 4, p. 100 025, 2022.

[154] Y. Kivshar, "All-dielectric meta-optics and non-linear nanophotonics," *National Science Review*, vol. 5, no. 2, pp. 144–158, 2018.

[155] J. E. Fröch *et al.*, "Real time full-color imaging in a meta-optical fiber endoscope," *eLight*, vol. 3, no. 1, pp. 1–8, 2023.

[156] S. Pinilla *et al.*, "Miniature color camera via flat hybrid meta-optics," *Science Advances*, vol. 9, no. 21, eadg7297, 2023.

[157] A. S. Solntsev, G. S. Agarwal, and Y. S. Kivshar, "Metasurfaces for quantum photonics," *Nature Photonics*, vol. 15, no. 5, pp. 327–336, 2021.

[158] P. Georgi *et al.*, "Metasurface interferometry toward quantum sensors," *Light: Science & Applications*, vol. 8, no. 1, p. 70, 2019.

[159] J. Liu, M. Shi, Z. Chen, S. Wang, Z. Wang, and S. Zhu, "Quantum photonics based on metasurfaces," *Opto-Electronic Advances*, vol. 4, no. 9, pp. 200 092–1, 2021.

[160] T. Santiago-Cruz *et al.*, "Resonant metasurfaces for generating complex quantum states," *Science*, vol. 377, no. 6609, pp. 991–995, 2022.

[161] S. Kruk and Y. Kivshar, "Functional meta-optics and nanophotonics governed by mie resonances," *Acs Photonics*, vol. 4, no. 11, pp. 2638–2649, 2017.

[162] K. F. Mak, C. Lee, J. Hone, J. Shan, and T. F. Heinz, "Atomically thin mos 2: A new direct-gap semiconductor," *Physical review letters*, vol. 105, no. 13, p. 136 805, 2010.

[163] J. A. Wilson and A. Yoffe, "The transition metal dichalcogenides discussion and interpretation of the observed optical, electrical and structural properties," *Advances in Physics*, vol. 18, no. 73, pp. 193–335, 1969.

[164] F Hu *et al.*, "Imaging exciton–polariton transport in mose2 waveguides," *Nature Photonics*, vol. 11, no. 6, pp. 356–360, 2017.

[165] M.-E. Kleemann *et al.*, "Strong-coupling of wse2 in ultra-compact plasmonic nanocavities at room temperature," *Nature communications*, vol. 8, no. 1, p. 1296, 2017.

[166] H.-Y. Chang *et al.*, "High-performance, highly bendable mos2 transistors with high-k dielectrics for flexible low-power systems," *ACS nano*, vol. 7, no. 6, pp. 5446–5452, 2013.

[167] B. Munkhbat, P. Wróbel, T. J. Antosiewicz, and T. O. Shegai, "Optical constants of several multilayer transition metal dichalcogenides measured by spectroscopic ellipsometry in the 300–1700 nm range: High index, anisotropy, and hyperbolicity," *ACS photonics*, vol. 9, no. 7, pp. 2398–2407, 2022.

[168] D. Hu *et al.*, "Probing optical anisotropy of nanometer-thin van der waals microcrystals by near-field imaging," *Nature communications*, vol. 8, no. 1, p. 1471, 2017.

[169] P. G. Zotev *et al.*, "Transition metal dichalcogenide dimer nanoantennas for tailored light–matter interactions," *ACS nano*, vol. 16, no. 4, pp. 6493–6505, 2022.

[170] C.-C. Huang, "Anisotropic slot waveguides with bulk transition metal dichalcogenides for crosstalk reduction and high-efficiency mode conversion," *Optics Express*, vol. 30, no. 17, pp. 30 219–30 232, 2022.

[171] F. Shen *et al.*, "Transition metal dichalcogenide metaphotonic and self-coupled polaritonic platform grown by chemical vapor deposition," *Nature Communications*, vol. 13, no. 1, p. 5597, 2022.

[172] V. E. Babicheva, S. Gamage, L. Zhen, S. B. Cronin, V. S. Yakovlev, and Y. Abate, "Near-field surface waves in few-layer mos2," *Acs Photonics*, vol. 5, no. 6, pp. 2106–2112, 2018.

[173] P. Kumar *et al.*, "Light–matter coupling in large-area van der waals superlattices," *Nature nanotechnology*, vol. 17, no. 2, pp. 182–189, 2022.

[174] X. Zhang *et al.*, "Azimuthally polarized and unidirectional excitonic emission from deep subwavelength transition metal dichalcogenide annular heterostructures," *ACS Photonics*, vol. 8, no. 10, pp. 2861–2867, 2021.

[175] P. Shah, T. N. Narayanan, C.-Z. Li, and S. Alwarappan, "Probing the biocompatibility of mos2 nanosheets by cytotoxicity assay and electrical impedance spectroscopy," *Nanotechnology*, vol. 26, no. 31, p. 315 102, 2015.

[176] J. H. Appel *et al.*, "Low cytotoxicity and genotoxicity of two-dimensional mos2 and ws2," *ACS Biomaterials Science & Engineering*, vol. 2, no. 3, pp. 361–367, 2016.

[177] J. Lee *et al.*, "Two-dimensional layered mos2 biosensors enable highly sensitive detection of biomolecules," *Scientific reports*, vol. 4, no. 1, p. 7352, 2014.

[178] S. Barua, H. S. Dutta, S. Gogoi, R. Devi, and R. Khan, "Nanostructured mos2-based advanced biosensors: A review," *ACS Applied Nano Materials*, vol. 1, no. 1, pp. 2–25, 2017.

[179] H. Park *et al.*, "Ultrasensitive and selective field-effect transistor-based biosensor created by rings of mos2 nanopores," *ACS nano*, vol. 16, no. 2, pp. 1826–1835, 2021.

[180] G. Mie, "Beiträge zur optik trüber medien, speziell kolloidaler metallösungen," *Annalen der Physik*, vol. 330, no. 3, pp. 377–445, 1908.

[181] H. Horvath, "Gustav mie and the scattering and absorption of light by particles: Historic developments and basics," *Journal of Quantitative Spectroscopy and Radiative Transfer*, vol. 110, no. 11, pp. 787–799, 2009.

[182] Y. Kivshar, "The rise of mie-tronics," *Nano Letters*, vol. 22, no. 9, pp. 3513–3515, 2022.

[183] A. I. Kuznetsov, A. E. Miroshnichenko, M. L. Brongersma, Y. S. Kivshar, and B. Luk'yanchuk, "Optically resonant dielectric nanostructures," *Science*, vol. 354, no. 6314, aag2472, 2016.

[184] S. H. Jones, M. D. King, and A. D. Ward, "Determining the unique refractive index properties of solid polystyrene aerosol using broadband mie scattering from optically trapped beads," *Physical Chemistry Chemical Physics*, vol. 15, no. 47, pp. 20 735–20 741, 2013.

[185] Y. Jahani *et al.*, "Imaging-based spectrometer-less optofluidic biosensors based on dielectric metasurfaces for detecting extracellular vesicles," *Nature Communications*, vol. 12, no. 1, p. 3246, 2021.

[186] A. Tittl *et al.*, "Imaging-based molecular barcoding with pixelated dielectric metasurfaces," *Science*, vol. 360, no. 6393, pp. 1105–1109, 2018.

[187] Y. Yu *et al.*, "Exciton-dominated dielectric function of atomically thin mos2 films," *Scientific reports*, vol. 5, no. 1, pp. 1–7, 2015.

[188] S. B. Anantharaman, K. Jo, and D. Jariwala, "Exciton–photonics: From fundamental science to applications," *ACS nano*, vol. 15, no. 8, pp. 12 628–12 654, 2021.

[189] G. Ermolaev *et al.*, "Giant optical anisotropy in transition metal dichalcogenides for next-generation photonics," *Nature communications*, vol. 12, no. 1, p. 854, 2021.

[190] R. Verre, D. G. Baranov, B. Munkhbat, J. Cuadra, M. Käll, and T. Shegai, "Transition metal dichalcogenide nanodisks as high-index dielectric mie nanoresonators," *Nature nanotechnology*, vol. 14, no. 7, pp. 679–683, 2019.

[191] V. E. Babicheva and J. V. Moloney, "Lattice resonances in transdimensional ws2 nanoantenna arrays," *Applied Sciences*, vol. 9, no. 10, p. 2005, 2019.

[192] A. V. Prokhorov, A. V. Shesterikov, M. Y. Gubin, V. S. Volkov, and A. B. Evlyukhin, "Quasitrapped modes in metasurfaces of anisotropic mos 2 nanoparticles for absorption and polarization control in the telecom wavelength range," *Physical Review B*, vol. 106, no. 3, p. 035 412, 2022.

[193] B. Munkhbat, B. Küçüköz, D. G. Baranov, T. J. Antosiewicz, and T. O. Shegai, "Nanostructured transition metal dichalcogenide multilayers for advanced nanophotonics," *Laser & Photonics Reviews*, vol. 17, no. 1, p. 2 200 057, 2023.

[194] C. Hsu *et al.*, "Thickness-dependent refractive index of 1l, 2l, and 3l mos2, mose2, ws2, and wse2," *Advanced optical materials*, vol. 7, no. 13, p. 1 900 239, 2019.

[195] P. Sen and M. Gupta, "Single nucleotide detection using bilayer mos 2 nanopores with high efficiency," *RSC advances*, vol. 11, no. 11, pp. 6114–6123, 2021.

[196] P. Sen, H. Hoi, and M. Gupta, "Low noise hybrid nanopore with engineered ompg and bilayer mos2," *ACS Applied Bio Materials*, vol. 4, no. 7, pp. 5416–5424, 2021.

[197] S. Catalán-Gómez *et al.*, "Breast cancer biomarker detection through the photoluminescence of epitaxial monolayer mos2 flakes," *Scientific Reports*, vol. 10, no. 1, p. 16 039, 2020.

[198] D. Gudi, P. Sen, A. A. Forero Pico, D. Nandi, and M. Gupta, "Optimization of growth parameters to obtain epitaxial large area growth of molybdenum disulfide using pulsed laser deposition," *AIP Advances*, vol. 12, no. 6, 2022.

[199] L. Jiao *et al.*, "Fabrication and characterization of two-dimensional layered mos2 thin films by pulsed laser deposition," *Advances in Condensed Matter Physics*, vol. 2018, 2018.

[200] A. Barvat *et al.*, "Electronic structure of the pld grown mixed phase mos2/gan interface and its thermal annealing effect," *Current Applied Physics*, vol. 18, no. 2, pp. 170–177, 2018.

[201] A. Barvat *et al.*, "Mixed phase compositions of mos2 ultra thin film grown by pulsed laser deposition," *Materials Today: Proceedings*, vol. 5, no. 1, pp. 2241–2245, 2018.

[202] H. F. McMurdie *et al.*, "Standard x-ray diffraction powder patterns from the jcpds research associateship," *Powder Diffraction*, vol. 1, no. 2, pp. 64–77, 1986.

[203] Y. Zhang *et al.*, "All-dielectric refractive index sensor based on fano resonance with high sensitivity in the mid-infrared region," *Results in Physics*, vol. 24, p. 104 129, 2021.

[204] J. Wei, Z. Zhao, F. Luo, K. Lan, R. Chen, and G. Qin, "Sensitive and quantitative detection of sars-cov-2 antibodies from vaccinated serum by mos2-field effect transistor," *2D Materials*, vol. 9, no. 1, p. 015 030, 2021.

[205] K. Yee, "Numerical solution of initial boundary value problems involving maxwell's equations in isotropic media," *IEEE Transactions on antennas and propagation*, vol. 14, no. 3, pp. 302–307, 1966.

[206] Y. Ji *et al.*, "Dft-calculated ir spectrum amide i, ii, and iii band contributions of n-methylacetamide fine components," *ACS omega*, vol. 5, no. 15, pp. 8572–8578, 2020.

Appendix A: Finite Difference Time Domain (FDTD) Simulations

The finite-difference time-domain (FDTD) method is widely considered as one of the simplest yet powerful full-wave techniques for solving electromagnetics problems. Its implementation is uncomplicated, and it can handle a broad range of problems with remarkable accuracy. However, like all numerical methods, it has its limitations, and the accuracy depends on the implementation. Although FDTD can solve complicated problems, it is frequently computationally demanding. Solutions may require a substantial amount of memory and computation time, which can increase with the complexity of the problem. The Finite-Difference Time-Domain (FDTD) method is a numerical technique that employs finite differences to approximate both the spatial and temporal derivatives that appear in Maxwells equations. Kane S. Yee's groundbreaking paper [205], published in 1966, introduced a discrete solution to Maxwell's equations that relied on central difference approximations of the curl-equations' spatial and temporal derivatives. One of the advantages of the FDTD method is its ability to model various types of materials and medium. The FDTD method is adept at handling media that are non-uniform and prone to loss. Complex media such as frequency-dependent dispersive, anisotropic, bi-anisotropic, chiral, or non-linear can also be dealt by the FDTD method. In the last few decades, researchers have devoted considerable resources to developing precise and efficient algorithms to simulate these types of media within the framework of the FDTD method. The Yee algorithm is discussed below.

A.1 The Yee Algorithm

The formulation is based on discretizing the volume domain with a regular, structured, staggered, rectangular grid. The novel scheme he derived to achieve this, now referred to as the Yee-algorithm, is detailed in this section.

FDTD solves Maxwell's curl equations in non-magnetic materials:

$$\frac{\partial \mathbf{D}}{\partial t} = \nabla \times \mathbf{H} \tag{A.1}$$

$$\mathbf{D}(\omega) = \epsilon_0 \epsilon_r(\omega) \mathbf{E}(\omega) \tag{A.2}$$

$$\frac{\partial \mathbf{H}}{\partial t} = -\frac{1}{\mu_0} \nabla \times \mathbf{E} \tag{A.3}$$

where $\mathbf{H}$: magnetic field, $\mathbf{E}$: electric field, and $\mathbf{D}$: displacement field. $\epsilon_r(\omega)$ denotes the complex relative dielectric constant related to the refractive index (n) of the medium as follows:

$$\epsilon_r(\omega) = n^2 \tag{A.4}$$

In 3D FDTD simulations, Maxwell's equations in three dimensions describe six elec-

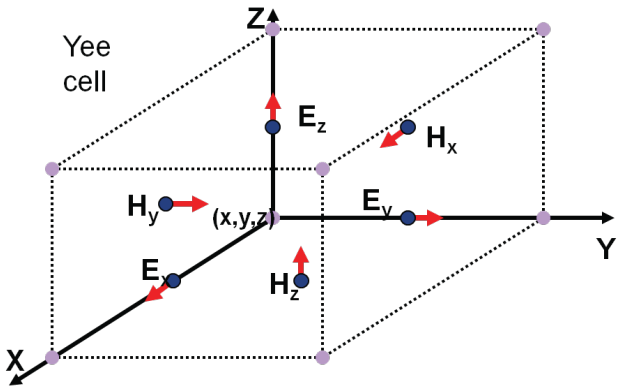

Figure A.1: schematic of the Yee cell [108]

tromagnetic field components, namely E_x, E_y, E_z, H_x, H_x, and H_z. FDTD method solves the Maxwell's equations on a discrete spatial and temporal grid known as "Yee cell" as shown in Fig. A.1, where each field component is solved in the Yee-cell as shown.

Incorporating dispersive materials that possess tabulated refractive index (n,k) data as a function of wavelength can be achieved using multi-coefficient material models. These models are designed to automatically generate a material model that is based on the tabulated data ensuring maximum efficiency and accuracy.

Appendix B: Supplementary Information for Chapter 3

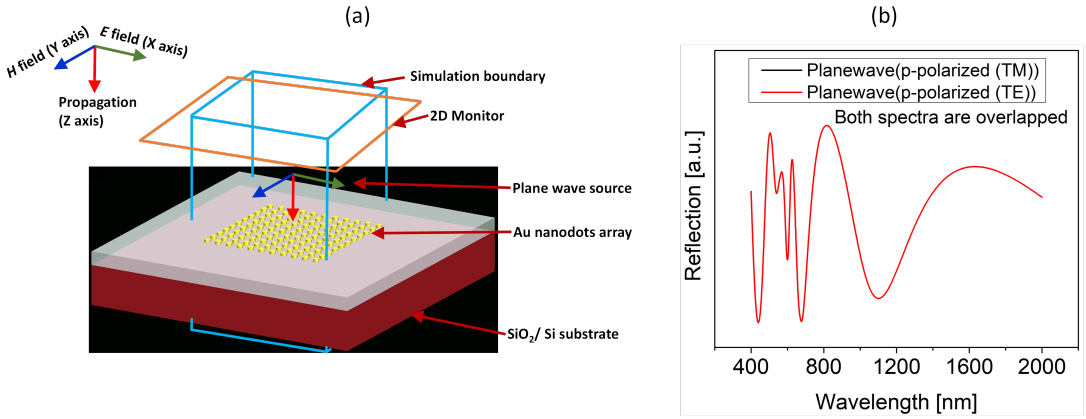

Figure B.1: (a) Schematic illustration shows the simulation set up. Here, the plane wave source is TM polarized as shown. (b) Simulated reflection spectra recorded by the 2D monitor with both TE and TM polarization of plane wave source. There is no difference between two distinct polarizations because of the geometrically symmetric Au nanodots array on both X and Y directions.

To confirm the fact that DSP molecule has good selectivity with the gold surface compared to the SiO_2/Si substrate surface, we have conducted a separate test with a piece of SiO_2/Si half covered with 50 nm thick Au with 5 nm Ti adhesion layer. We have placed a piece of SiO_2/Si with a kapton tape covered a part during the Au deposition with the e-beam evaporation while preparing the Au nanodots array to keep the deposition condition same. DSP surface activation procedure (as discussed in methods section) followed and after that 50 μL of 1 mg/mL BSA (Bovine serum albumin) diluted in PBS drop casted on the whole substrate surface covering gold thin film and SiO_2/Si substrate surface area. Fourier-transform infrared spectroscopy (FTIR) measurement (see Fig. B.4 (a) and (b)) was performed both on the Au thin

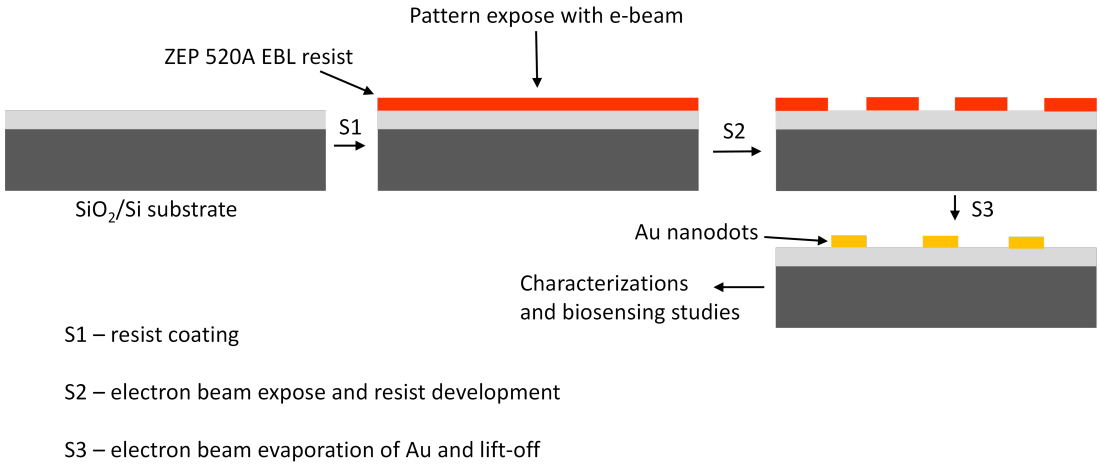

Figure B.2: Schematic illustrates the fabrication process flow, and the details description is in the Experimental Methods Section.

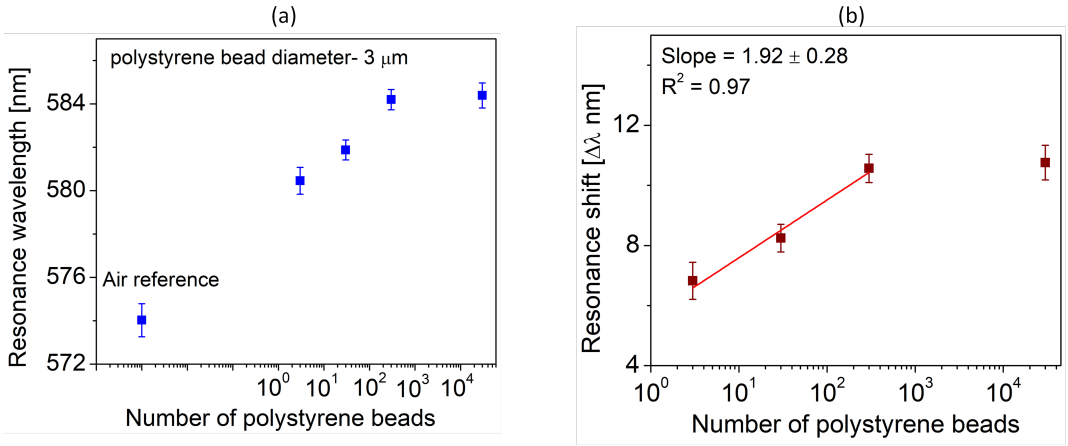

Figure B.3: 3 μm polystyrene beads testing results: (a) Resonance wavelength position with the number of polystyrene beads and (b) Resonance shift plot with the increasing number of polystyrene beads. The linear fit shows the slope 1.92 $\pm$ 0.28 nm/decade with the goodness of fit $R^2 = 0.97$.

film and bare SiO_2/Si substrate areas and the peaks observed at 1663.6 cm^{-1} (amide I peak [206]) and 1546.17 cm^{-1} (amide II peak [206]) from the Au surface area only. However, these two peaks specific two only amide I and amide II are not visible while FTIR measurement was performed on the SiO_2 surface. This indicates that DSP molecule has a very good selectivity to Au compared to the SiO_2 surface. The photographs of all the sample chips used for this test is displayed in Fig. B.4 (c).

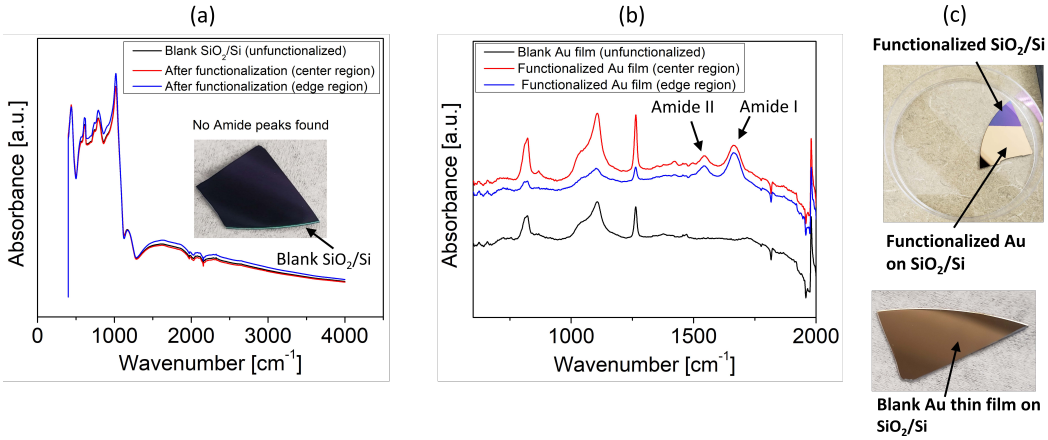

Figure B.4: Selectivity test of self-assembled monolayer of DSP on Au film surface with respect to the SiO_2/Si substrate surface. (a) FTIR spectra measured on blank (unfunctionalized) SiO_2/Si substrate surface as-well-as on SiO_2 surface of half-covered Au film chip after functionalization. There are not Amide peaks found from SiO_2 area, which indicates there was no attachments of DSP on SiO_2 surface area. (b) FTIR spectra collected form blank (unfunctionalized) Au sample as-well-as Au film area of half-covered chip after DSP functionalization and BSA attachments. Spectra clearly display that two characteristic Amide I and Amide II peaks observed on the functionalized Au thin film chip, but it is not visible from the blank Au (unfunctionalized) chip. (c) Photograph shows all the 3 different chips.

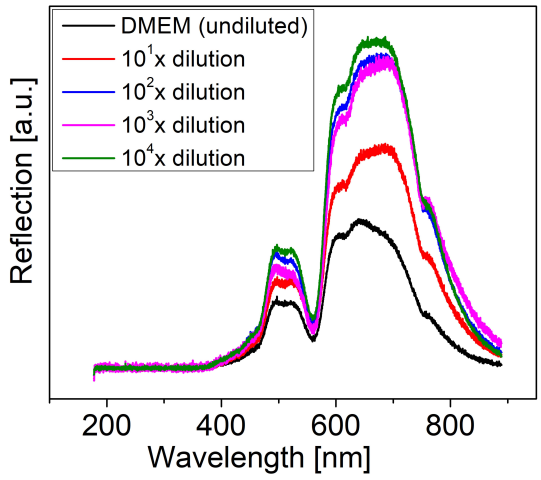

Figure B.5: Reflection spectra collected form an unfunctionalized Au nanodots array (D = 100 nm, P = 200 nm) device after drop-casting 50 μL fresh DMEM solution from the original stock (undiluted) and after diluting with PBS of different folds ($10^1\times$ to $10^4\times$ dilution). There is no peak shift observed wither of the resonance positions.

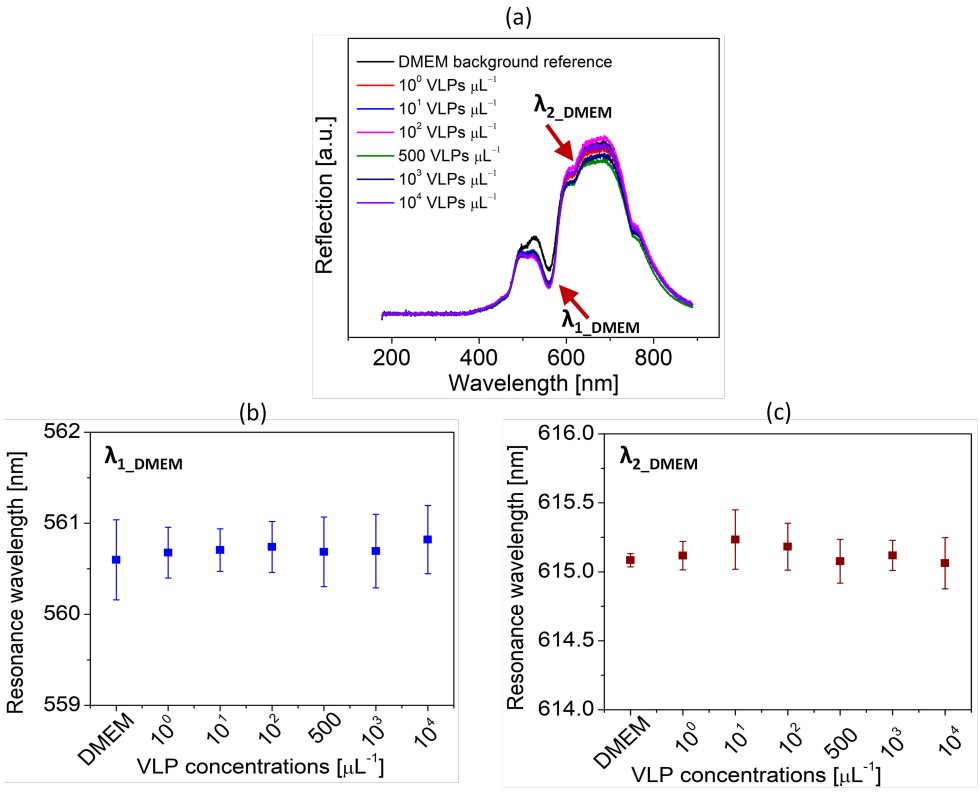

Figure B.6: VLP specificity test: Unfunctionalized 8 Au nanodots array devices (D = 100 nm and P = 200 nm) were tested (a) Spectra collected from a device shows the DMEM background (reference) and after addition of different VLP concentrations. There is no shift observed on both the resonance positions. No significance resonance shift found on mean resonance positions (error bar shows standard deviation from 8 devices) of (b) λ_{1_DMEM} (c) λ_{2_DMEM} after varying VLP concentrations: $10^0 \mu L^{-1}$ $10^4 \mu L^{-1}$ with respect to the DMEM reference. This highlights that VLPs are very specific to the anti-SARS-CoV-2 antibody and without antibody functionalization no VLPs are attached on the Au nanodots array devices.

Appendix C: Additional Data

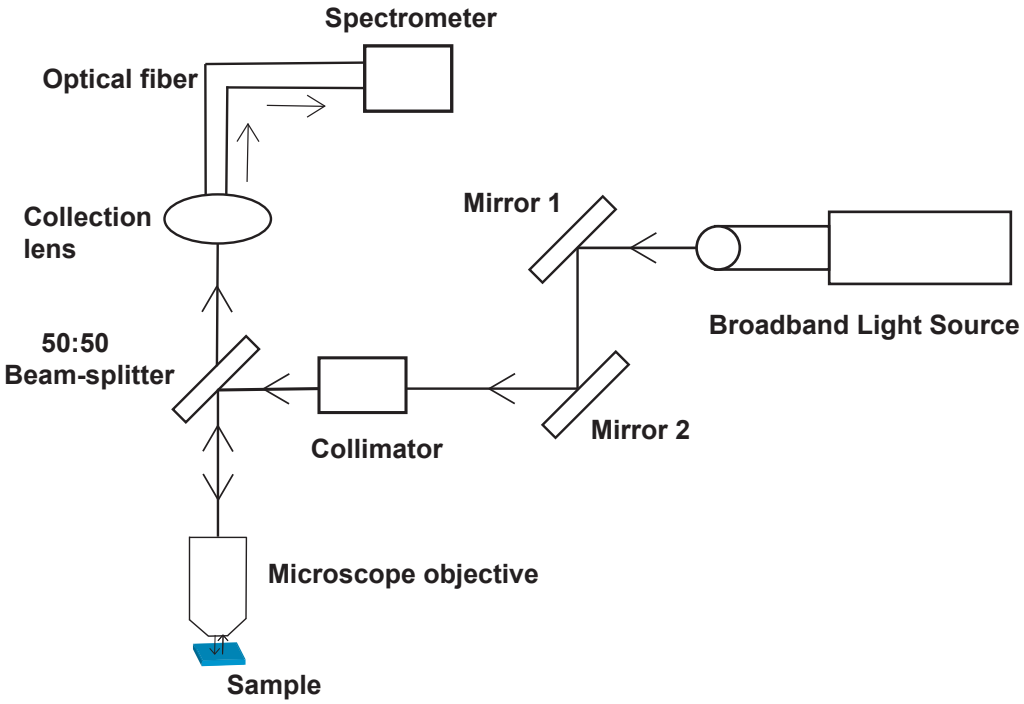

Figure C.1: Schematic illustration of the optics measurement setup.

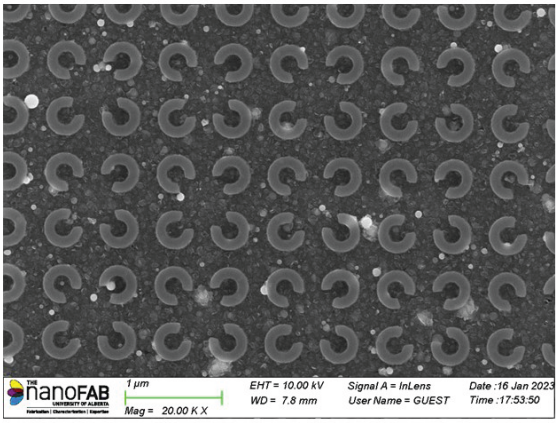

Figure C.2: EBL patterning on 150 nm thick MoS_2 split-nanorings (before etching was performed).

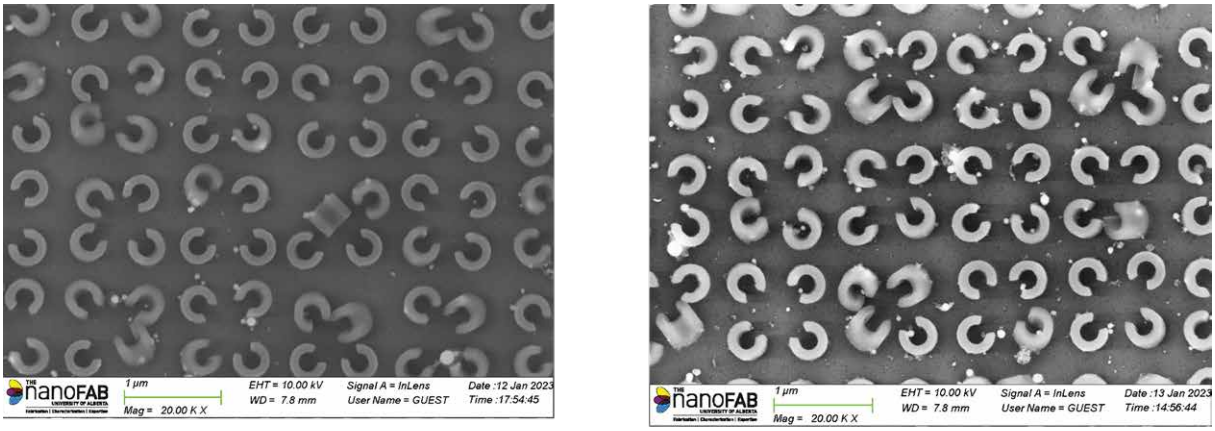

Figure C.3: MoS_2 etching with standard RIE technique uisng NGP system.

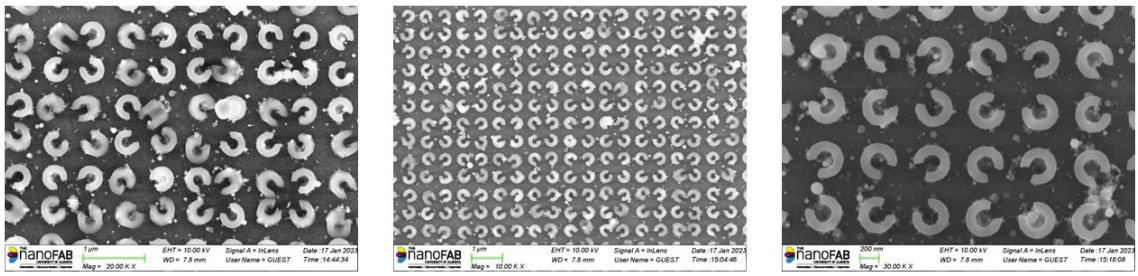

Chip 1:

No O_2 plasma step

SF_6 : 20W, 60 sec, 80 mTorr, 15 sccm

Chip 2:

No O_2 plasma step

SF_6 : 20W, 75 sec, 80 mTorr, 15 sccm

Chip 3:

No O_2 plasma step

SF_6 : 10W, 95 sec, 80 mTorr, 15 sccm

Figure C.4: Defects arose during the 150 nm thick MoS_2 split-nanorings etching with RIE technique (NGP system used).

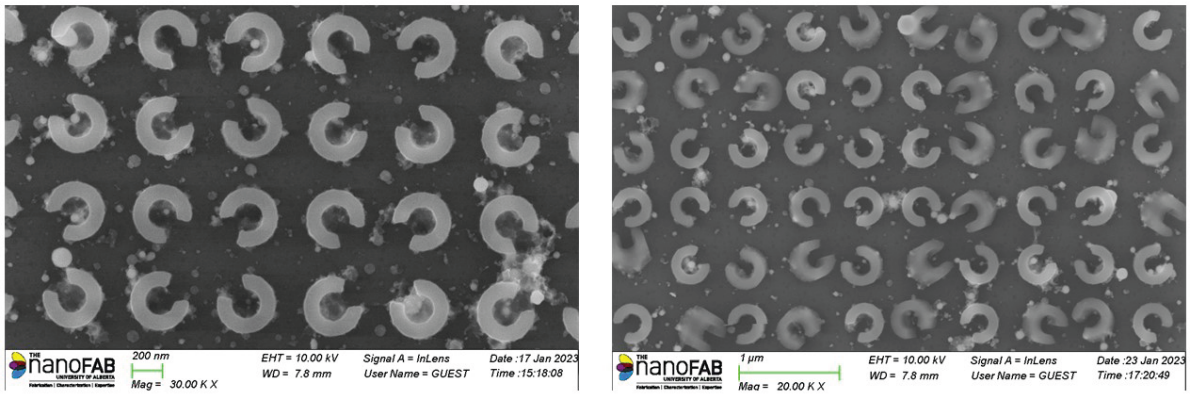

Chip 3:

No O_2 plasma step

SF_6 : 10W, 95 sec, 80 mTorr, 15 sccm

NGP system used

Chip 3:

No O_2 plasma step

SF_6 : 10W, 95+90 = 185 sec, 80 mTorr, 15 sccm

Figure C.5: Defects and issues faced during the 150 nm thick MoS_2 split-nanorings etching with standard RIE technique using NGP system.

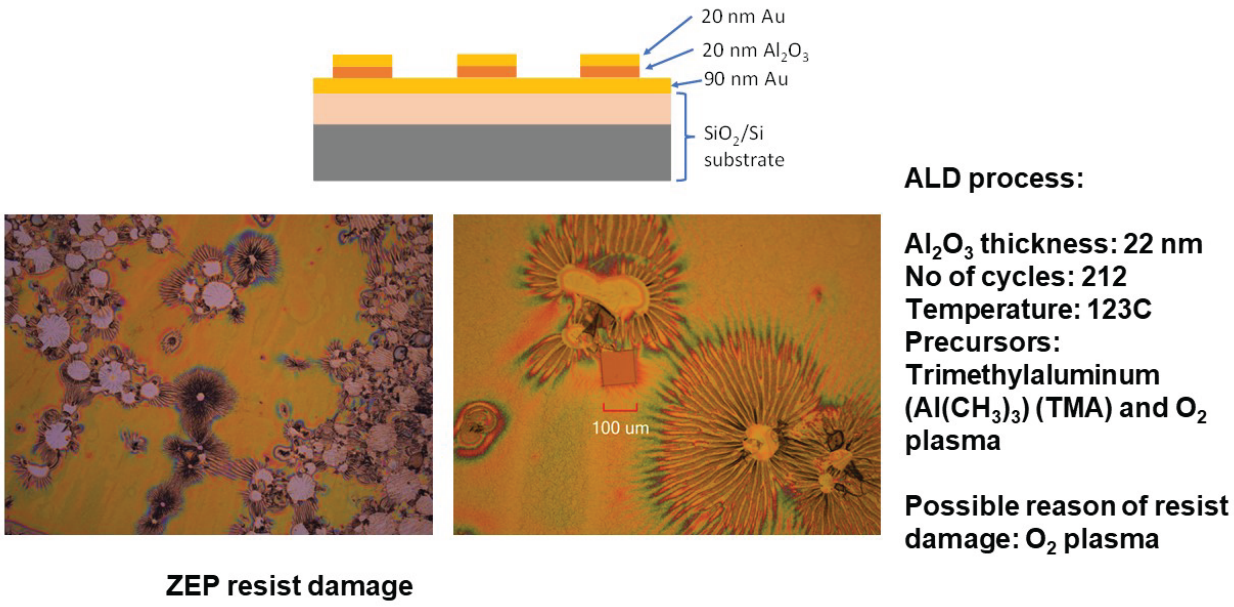

Figure C.6: Defects and issues arose during the fabrication process of MIM nanostructure fabrication. ZEP resist damaged during the Al_2O_3 deposition by atomic layer deposition (ALD).

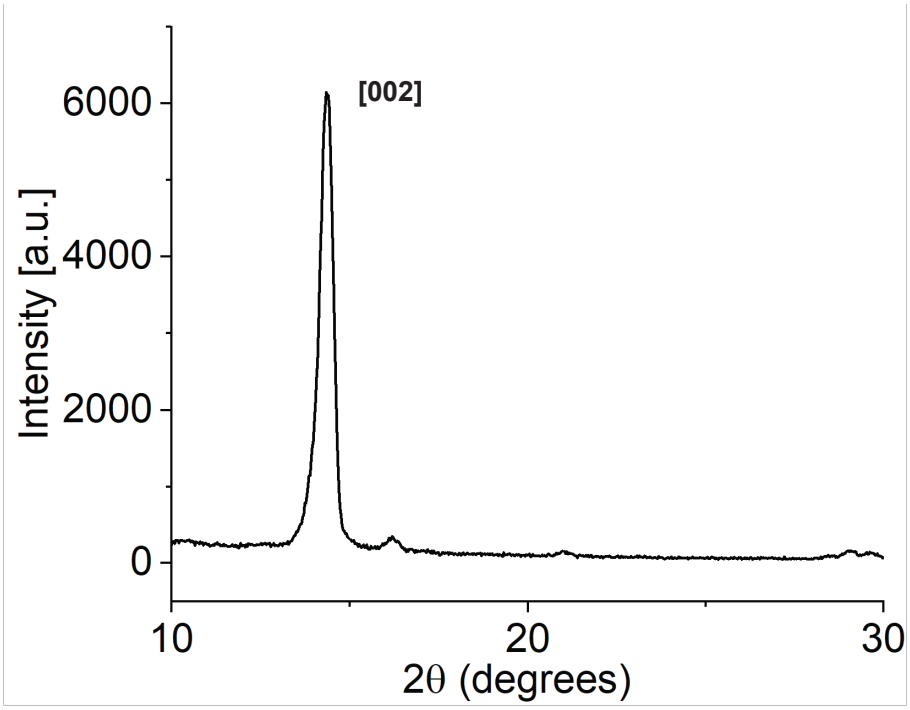

Figure C.7: XRD measurement was performed on the MoS_2 target for pulsed laser deposition system. The peak position at $\backsim$14.4° represents the [002] peak and demonstrates the highly crystalline structure.